2013

PHYSICOCHEMICAL MODIFICATIONS AND APPLICATIONS OF CARBON NANO-ONIONS FOR ELECTROCHEMICAL ENERGY STORAGE

Rituraj Borgohain
University of Kentucky, rborgoha@uwyo.edu

STUDENT AGREEMENT:

I represent that my thesis or dissertation and abstract are my original work. Proper attribution has been given to all outside sources. I understand that I am solely responsible for obtaining any needed copyright permissions. I have obtained and attached hereto needed written permission statements(s) from the owner(s) of each third-party copyrighted matter to be included in my work, allowing electronic distribution (if such use is not permitted by the fair use doctrine).

I hereby grant to The University of Kentucky and its agents the non-exclusive license to archive and make accessible my work in whole or in part in all forms of media, now or hereafter known. I agree that the document mentioned above may be made available immediately for worldwide access unless a preapproved embargo applies.

I retain all other ownership rights to the copyright of my work. I also retain the right to use in future works (such as articles or books) all or part of my work. I understand that I am free to register the copyright to my work.

REVIEW, APPROVAL AND ACCEPTANCE

The document mentioned above has been reviewed and accepted by the student's advisor, on behalf of the advisory committee, and by the Director of Graduate Studies (DGS), on behalf of the program; we verify that this is the final, approved version of the student's dissertation including all changes required by the advisory committee. The undersigned agree to abide by the statements above.

Rituraj Borgohain, Student

Dr. John P. Selegue, Major Professor

Dr. Dong-Sheng Yang, Director of Graduate Studies

PHYSICOCHEMICAL MODIFICATIONS AND APPLICATIONS OF CARBON NANO-ONIONS FOR ELECTROCHEMICAL ENERGY STORAGE

DISSERTATION

A dissertation submitted in partial fulfillment of the

requirement for the degree of Doctor of Philosophy in the

College of Arts and Science

at the University of Kentucky

By

Rituraj Borgohain

Lexington, Kentucky

Director: Dr. John P. Selegue, Professor of Chemistry
Lexington, Kentucky

2013

ABSTRACT OF DISSERTATION

PHYSICOCHEMICAL MODIFICATIONS AND APPLICATIONS OF CARBON NANO-ONIONS FOR ELECTROCHEMICAL ENERGY STORAGE

Carbon nano-onions (CNOs), concentrically multilayered fullerenes, are prepared by several different methods. We are studying the properties of two specific CNOs: A-CNOs and N-CNOs. A-CNOs are synthesized by underwater arc discharge, and N-CNOs are synthesized by high-temperature graphitization of commercial nanodiamond. In this study the synthesis of A-CNOs are optimized by designing an arc discharge aparatus to control the arc plasma. Moreover other synthesis parameters such as arc power, duty cycles, temperature, graphitic and metal impurities are controlled for optimum production of A-CNOs. Also, a very efficient purification method is developed to screen out A-CNOs from carboneseous and metal impurities. In general, A-CNOs are larger than N-CNOs (*ca.* 30 nm vs. 7 nm diameter). The high surface area, appropriate mesoporosity, high thermal stability and high electrical conductivity of CNOs make them a promising material for various applications. These hydrophobic materials are functionalized with organic groups on their outer layers to study their surface chemistry and to decorate with metal oxide nanoparticles. Both CNOs and CNO nanocomposites are investigated for application in electrochemical capacitors (ECs). The influences of pH, concentration and additives on the performance of the composites are studied. Electrochemical measurements demonstrate high specific capacitance and high cycling stability with high energy and power density of the composite materials in aqueous electrolyte.

Key words: Carbon Nano-onions, Arc discharge, Purification, Functionalization, Supercapacitor.

Rituraj Borgohain

09-28-2013

PHYSICOCHEMICAL MODIFICATIONS AND APPLICATIONS OF CARBON NANO-ONIONS FOR ELECTROCHEMICAL ENERGY STORAGE

By

Rituraj Borgohain

Dr. John P. Selegue

Director of dissertation

Dr. Dong-Sheng Yang

Director of graduate studies

09/28/2013

Date

Dedicated to my beloved parents, Late Debendra Nath Borgohain and Mrs. Renu Poma Borgohain

ACKNOWLEDGEMENTS

First of all my deepest gratitude goes to my parents. My father (Late D. N. Borgohain), whose constant inspiration, sacrifices, attitude towards life, and love keep motivating me to think broad and accept challenges humbly. My mother (Mrs. Renu Poma Borgohain), with a strong heart for compassion and belief that every person should contribute to his existence for something good for the rest of the society, helps me to stand up in the time of frustration and misery. I am also very grateful to my sister (Bristirekha Borgohain) for her love, inspiration and help in my difficult times. I sincerely thank my uncle (Mr. Robin Gogoi) for all his unconditional love and efforts to mentally and physically support my parents and me.

My greatest respect and acknowledgment goes to my advisor, Prof. John Paul Selegue for his continuous support, belief in my credibility and guidance to mature my scientific reasoning. He is the best teacher and guide I have so far in my academic career. His gentle attitude, family values, practical guidance, patience, and restless enthusiasm towards new ideas taught me many valuable lessons both on and off the research laboratory. My thanks go to my committee members, Dr. Mark Meier, Dr. David Atwood and Dr. Rodney Andrews. Their suggestions and considerations helped me to develop insightful thoughts in my projects and to access facilities to implement those thoughts experimentally.

My special thanks go to Prof. Y.-T. Cheng, at Department of Chemical and Materials Engineering for a very successful collaboration. The always charming and enthusiastic Prof. Y.-T. helped me in many ways including full access to his lab and financial assistance to my research. He also encouraged me to establish Materials

Research Society—University of Kentucky chapter by accepting the position of chapter advisor. I am also thankful to his student Dr. Juchuan Li for his collaboration. I thank Prof. Doo Young Kim for his collaboration and frequent valuable discussions on research projects.

I would like to thank Department of Chemistry, Department of Chemical and Materials Engineering, Center for Advanced Materials (CAM) and Center for Applied Energy Research (CAER) at UK for allowing me to use the facilities and financial supports during my doctoral research.

I would like to give my warmth love and respect to my friends and lab mates. Special thanks go to my best friend Buli Borah (my wife) and Subhash Patil, who inspired and motivated me to pursue Ph.D. studies abroad. I am indebted to their efforts to guide me and to help me to choose research as my carrier and a way of continuous learning process for self-development. Many thanks to my very close friends Aman, Anita, Mahendra and Sandeep for their help, fruitful discussions and making PhD study less frustrating. I am thankful to my lab mates, Bidhya, Deepshikha, Eric, Ilya, Surya and Dr. Uttam for the electric environment in the lab. Finally, I thank Almighty for His blessings.

TABLE OF CONTENTS

LIST OF FIGURES

LIST OF TABLES

LIST OF SCHEMES

Chapter I: Introduction to Carbon Nano-Onions

1.1 Introduction

Control of materials properties on the atomic and molecular scale has been a dominant research topic during the last few decades. Generally, these involve structures of 100 nm or smaller in at least one dimension. Carbon in sp^2-hybridized network can form a variety of structures with unique properties. Based on their dimensions, they are categorized as 3D (graphite), 2D (graphene), 1D (nanotubes) or 0D (fullerene). Although applications of nanomaterials have gained much attention only in recent years, the concept of low-dimensional materials evolved a long time back. In the 1960s, physicist Richard Feynman took the initiative to emphasize that control of the magnitude of various physical phenomena like van der Waals forces and surface tension could be more important to control the bulk properties of nanomaterials.[1]

Study of nanomaterials was boosted in the early 1980s with the invention of the scanning tunneling microscope (STM). This development for characterizing nanoparticles led to the discovery of another carbon allotrope known as "fullerene". In 1985, Richard Smalley, Harold Kroto and Robert Curl at the Rice University accidently discovered the smallest form of carbon nanoparticle (CNP), C_{60}, while vaporizing graphite to produce carbon polymer.[2] C_{60} or buckminsterfullerene was named after Richard Buckminster Fuller due to its resemblance to Fuller's geodesic dome structure. The IUPAC name of Buckminsterfullerene is C_{60}-I_h fullerene. C_{60} adopts a 60-vertex truncated icosahedral shape with 12 pentagonal and 20 hexagonal faces (**Fig. 1.1**). After $C_{60,}$ other stable fullerene homologue such as C_{70}, C_{74}, C_{76}, C_{78}, C_{80}, C_{82} have also been prepared.[3] Schmalz *et al*. proposed that for stable structure of fullerene, all the pentagons

must be isolated from each other by hexagons.[4] It was found that fullerenes that obey isolated pentagon rule (IPR) are more spherical and distribute the surface strain more evenly throughout the structure. However, exception to the IPR rule is found in many fullerenes, e.g. C_{62}, C_{64}, C_{66}, C_{68} etc.[5]

Various mechanisms have been proposed to explain the formation of fullerene. Although fullerenes are less stable than graphite, it is not only the thermodynamics that governed the product formation. Again, C_{60} is found as a major product as compared to thermodynamically more stable C_{70}.

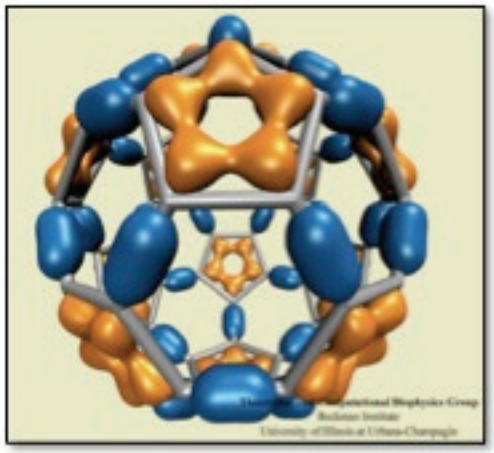

Figure 1.1. Model of fullerene (C_{60})

Electron delocalization and distribution of surface strain plays a major role during the formation of these fullerenes near the hot plasma zone. Chemical nature and structure of the initially formed species in the plasma governs the structure of the primary clusters. As the clusters begin to assemble to form a curvature, highly energetic dangling bonds are removed *via* annealing to form a completely closed structure. [6]

C_{60} is the most widely studied fullerene so far. It is insoluble in polar solvents. Solubility of C_{60} increases with increase in carbon chain in alkanes and aromatic solvents.[7, 8] Chemical reactivity of C_{60} mainly governed by the double bond character of ring and the surface strain. C_{60} is the most reactive while graphite with planar hexagonal array is the least reactive allotrope of carbon. With no hydrogen or functional groups on its surface, C_{60} undergoes nucleophilic addition reactions with Grignard reagent,

organolithium reagents, Bingel reaction,[9] Friedel-crafts alkylation,[10] and cycloaddition reactions. However, electrophilic addition reactions with halogens, such as $C_{60}F_{60}$ have also been reported.[11]

While working on fullerenes, Iijima discovered a new allotrope of carbon with needle-like structure where many tubes are nested inside one another. These are named as multi-walled carbon nanotubes (MWNTs). Again, two years later, Iijima and Ichihashi reported the discovery of single-walled nanotubes (SWNTs) in 1993.[12] Concurrently, Bethune *et al.* independently claimed the synthesis of SWNTs in the same year.[13] These discoveries of SWNTs were quite accidental in both cases, since SWNTs were formed in failed attempts to produce MWNTs filled with transition metals.

Carbon nanotubes are made up of graphene sheets. These sheets are planar network of interconnected hexagonal rings of carbon atoms. When graphene sheets are rolled into a cylinder and their edges joined, they form carbon nanotubes. They can be thought as elongated series of hexagons with fullerene-like hemispherical end caps. Since only the tangents of the graphitic planes come into contact with each other, their properties are more like those of a molecule.[14] A nanotube may consist of one tube of graphite, a one-atom thick single-wall nanotubes (SWNTs) or a number of concentric tubes called multi-wall nanotubes (MWNTs). Depending upon the rolling of graphene sheets in different ways, different types of CNTs can be formed. The three basic types of CNTs are zigzag, armchair and chiral (**Fig. 1.2**). It is possible to recognize zigzag,

armchair, and chiral CNTs by following the pattern across the diameter of the tubes and analysing their cross-sectional structure.[14] However MWNTs usually have more complex array of forms, because each concentric single wall nanotube can have different structures; hence there are a variety of sequential arrangements possible. When the concentric layers are identical but differ in diameter, the structure is simpler than that of mixed variants consisting of two or more types of concentric CNTs

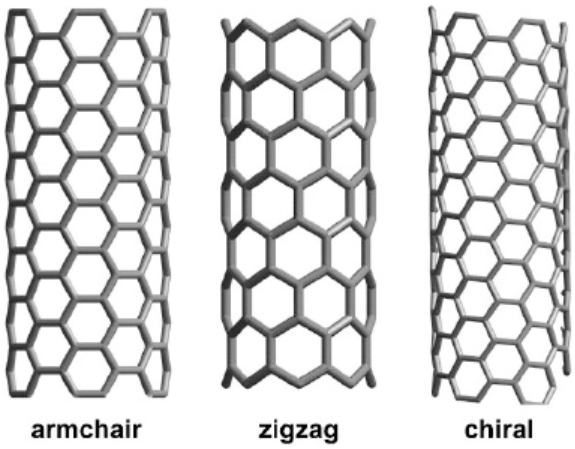

Figure 1.2. Types of **SWCNTs**

arranged in different order, which can have either regular layering or random layering. Carbon nanotubes can be synthesized either in the laboratory or on an industrial scale. However, further development of the existing techniques and new methods are required for continuous growth of CNTs with desirable properties. Some of the existing methods include arc discharge,[15] pulsed laser ablation,[16] and chemical vapor deposition (CVD). CVD is the most extensively used industrial method so far. In CVD, site selective synthesis at controllable locations and with desired orientations of CNT arrays on catalytic surface can be performed. For better alignment of CNTs plasma enhanced

chemical vapor deposition can also be used. In this technique CNTs are forced to align in the direction of applied electric field.[17]

In 1992 Ugarte reported curling and closure of graphitic networks under electron beam irradiation. He found that with increase in electron beam energy in the microscope, carbon soot reorganized to form spherical, concentric fullerene networks. These materials had fullerenes nested inside one another, commonly known as carbon nano-onions (CNOs). Carbon nano-onions formed under his experimental condition had average diameter of 20–30 nm.[18] These are the least studied carbon nanoparticles to date.

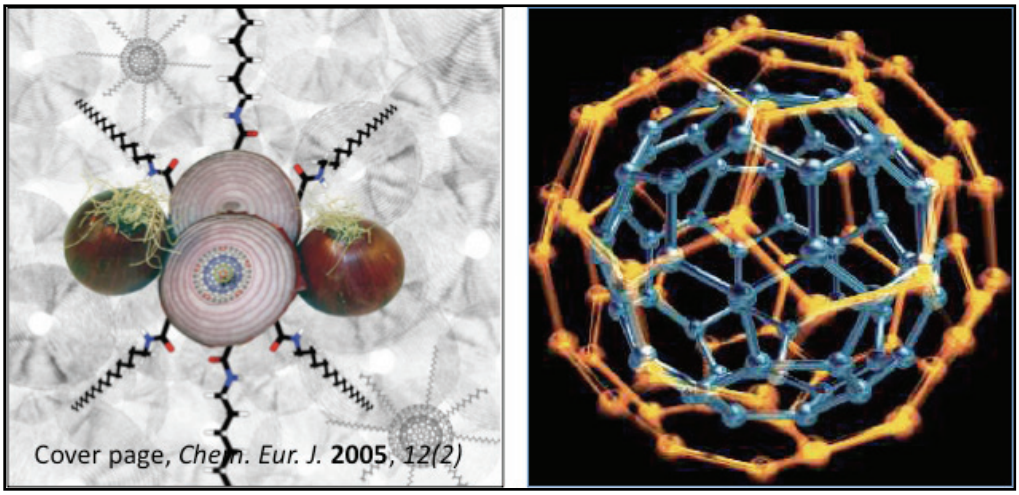

Figure 1.3 Models of carbon nano-onion

Different methods such as electron irradiation, [18, 19] ion implantation,[20] counter flow diffusion flames,[21] CVD using transition metal catalyst,[22] plasma enhanced CVD,[23] annealing nanodiamonds,[24, 25] plasma spraying of nanodiamonds,[26] underwater arc discharge,[27] have been used to produce CNOs. Most of these methods can produce only a minute quantity of CNOs and can't be used for bulk production. Further development of these methods to produce CNOs in bulk quantity is still under investigations. However,

high temperature annealing of nanodiamonds and under water arc discharge produces CNOs in bulk quantities as compared to other available methods.

1.1.1 Annealing nanodiamond

In 1994, Kuznetsov *et al*. discovered an easy method to synthesis carbon nano-onions.[24] A simple thermal annealing of very high surface energy diamond nanoparticles, obtained by detonation technique, induces their progressive transformation towards carbon nano-onions.[28] Carbon nanodiamonds, also known as ultra-dispersed diamonds, are originated from detonation of explosive mixture, such as mixture of trinitrotoluene (TNT) and cyclotrimethylenetrinitramine. Nanodiamonds have spherical and quasi-spherical particles with average diameter of 5 nm. When these diamond particles were annealed at 1000−1800 °C in a high vacuum chamber, structural imperfection due to the dangling bonds were removed and the particles were transformed into closed onion-like structures by minimizing their surface energy. N-CNOs (nanodiamond-annealed CNOs) produced under these conditions have average diameter of 5-7 nm. Furthermore, the discovery of a progressive transformation of diamond nano-particles into carbon nano-onions is of great interest to astrophysicists since it could explain the possibility of carbon nano-onions in interstellar dust.[29]

1.1.2 Underwater arc discharge

In 2001, Sano *et al.* reported a bench-top method for large-scale synthesis of A-CNOs (arc prepared CNOs). In their method CNOs were synthesized by producing arc with two pure graphite electrodes submerged in deionized water. A moveable 5 mm electrode acts as an anode and a stationary 12 mm electrode acts as a cathode.. A discharge voltage of 16-17 V and current of 30 A were used to produce the arc. Under

HRTEM, spherical carbon nano-onions as well as polyhedral and nested onion-like particles are found. The average diameter of these onions was 25–30 nm, having 7–15 concentric walls with a hollow core diameter of 5-7 nm. In this method, they reported a production rate of 3 $mg.min^{-1}$. Although Sano proposed that most of the pure onions float on the surface, it was found that majority of the CNOs fall to the bottom of the water container.[30]

H. Lange *et al.* studied some details of the carbon arc discharge process in water to determine the temperature distribution of the arc and the intermediate species formed. They used both pure and doped (Gd, Y) electrodes to study the selectivity of this process for nanomaterial generation. Plasma spectroscopy studies revealed the presence of C_2 radical along with atomic H and O in the plasma. The average plasma temperature for the electric arc produced under water by 40 A and 21 V was ca. 4000–6500 K.[31] Although a large amount of C_2 was found, no fullerenes were detected. This may be due to the presence of hydrogen, oxygen and water vapor which significantly hindered C_{60} formation.[32] Sano *et al.* proposed a mechanism of A-CNO formation under arc-discharge conditions (**Fig. 1.4)**.[27]

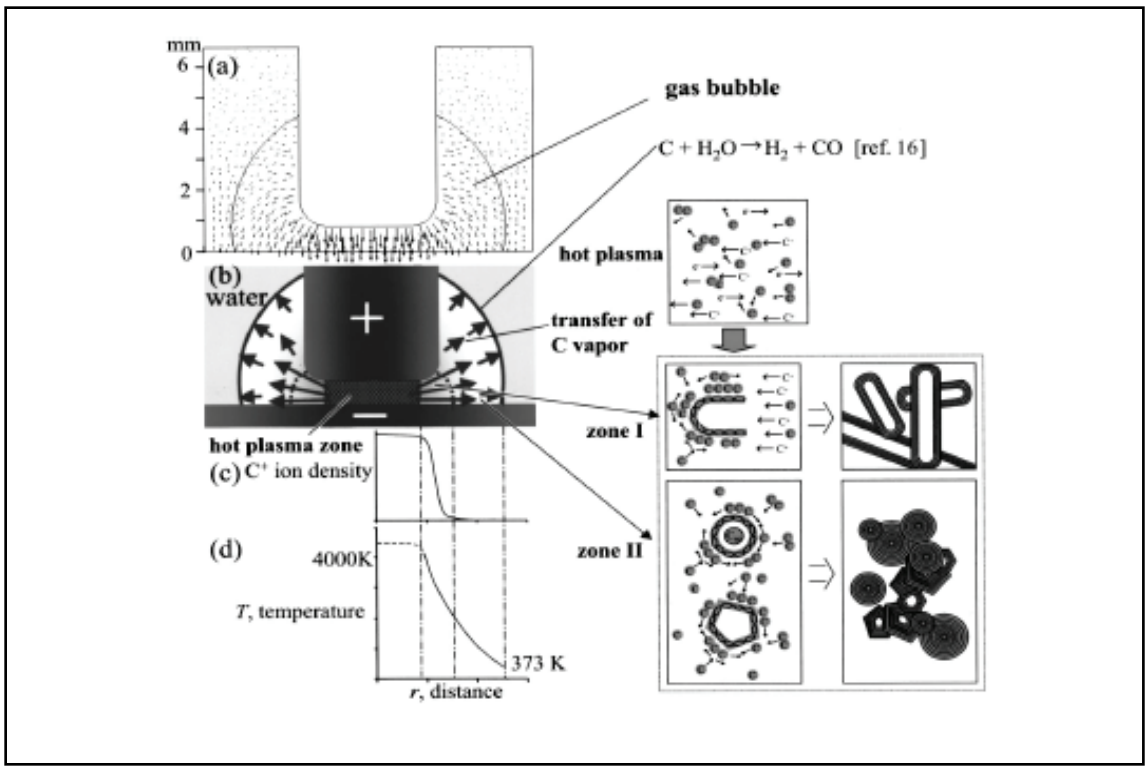

Figure 1.4. (a) Gas bubble formation in water at the interface of anode and cathode due to applied electric field (b) thermal expansion during the formation of the plasma (c) qualitative ion density distribution (d) theoretical temperature gradient (zone I) elongated particles formation zone (zone II) CNOs formation zone .[27]

Many potential applications of CNOs have been proposed, including but not limited to gas storage,[27] photovoltaic cells,[33] optically transparent electrodes,[34] catalysis,[35] electrochemical capacitor,[36] and biomedical applications.[37] Due to higher surface area of CNOs as compared to SWNTs and MWNTs, CNOs have also been proposed as potential candidates for the development of miniaturized fuel cells. Recently, NASA researchers have proposed that CNOs might serve as an excellent additive for aerospace applications.[23] Better insight into the tribological properties of CNOs showed

that these particles can provide adequate and even superior lubrication properties than the commonly used graphitic materials and other conventional lubricants.[38]

In our current study we set out to work on two different kinds of CNOs. N-CNOs will be synthesized by annealing commercially available nanodiamonds and A-CNOs will be synthesized by a controlled arc discharge method. Basic properties including physical characteristics, surface reactivity, chemical functionalization etc. will be studied in detail for both types of CNOs. Moreover, the applications of both types of CNOs and their composites will be studied for electrochemical energy storage applications.

Chapter II: Instrumentation and Optimization of A-CNO Synthesis

2.1 Introduction

Sano *et al*. introduced the process of CNO production using arc discharge between two graphite electrodes submerged under deionized water. They reported initial production of A-CNOs at the rate of 3 $mg \cdot min^{-1}$ using an "unsophisticated" apparatus.[30] Although it was not adequate for industrial process, the yield was much higher than most of the other methods available at that time. There are many advantages of this process, such as simplicity in handling bench-top apparatus, availability of low-cost, pure raw materials and reasonable scale of production. There are various possible modifications to be made for mass production of pure nano-materials using this technique. These include control over the arc power, maintaining optimum gap between the electrodes, temperature of the surrounding water, physical parameters such as purity of the starting materials and the proper alignment (horizontal and vertical) of the electrodes.

Selegue and Chen at the University of Kentucky worked on CNOs produced by arc discharge, using high-purity graphite electrodes submerged in deionized water while purging helium through it. The production rate of nano-materials in their system was *ca.* 200 $mg.day^{-1}$. Initial characterization studies detected CNOs with average diameter of 25–30 nm. Later John Craddock continued their work and he made some progress in the development of arc-discharge apparatus. He addressed issues like proper alignment of the moving anode over stationary cathode, but the nylon driver rod melted at its junction with the anode. These problems were solved first by putting an acrylic guide/plate with a 5/16'' diameter hole directly above the cathode so that the anode fit snugly through the guide and remained well centered above the cathode. The acrylic guide was positioned

~1.5‘’ above the cathode to avoid overheating. Secondly, the overheating of nylon rod at the junction was dealt with by plugging a self-aligning tube-to-pipe adapter (McMaster-Carr part #5220K35) in the apparatus. These modifications led to a bright white plasma that could be mechanically maintained for an average of 45 s.[39] Also he reported that the time required to consume the anode (6’’ long, diameter ¼’’) was considerably reduced from ~12 h to ~4 h and the yields at an average of ~ 0.900 g were observed.

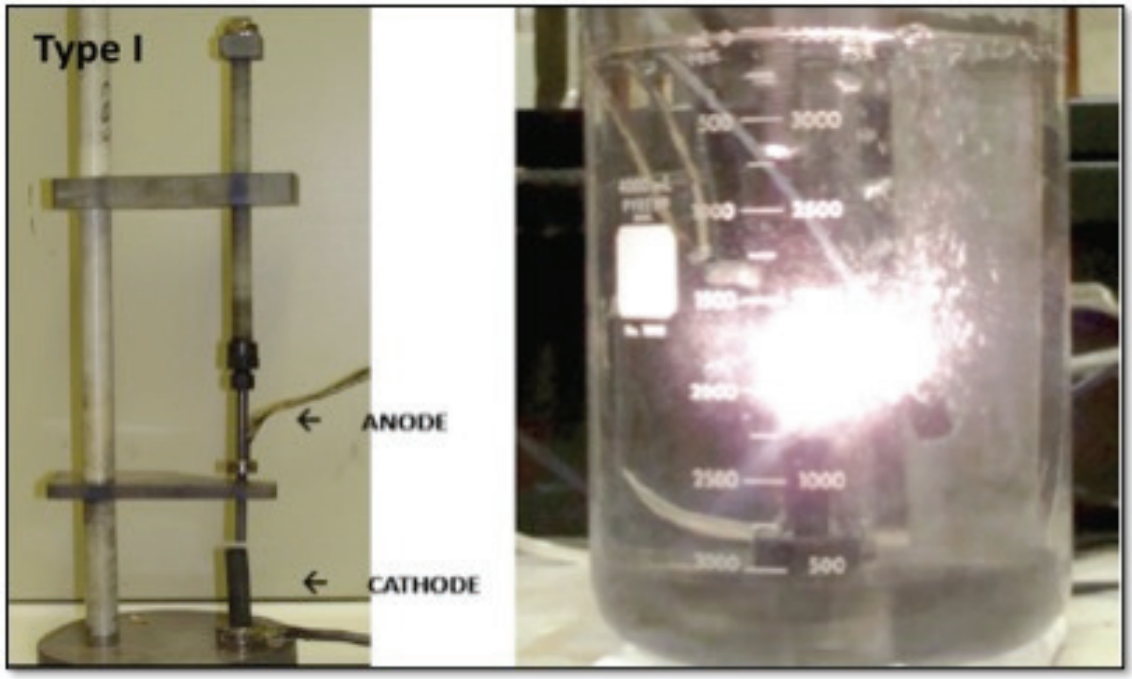

Figure 2.1. Type I Manual arc-discharge apparatus for A-CNO synthesis

The arc-discharge apparatus developed so far had some technical problems. These include mechanical rotation of the nylon-driver to keep the anode consistently over the cathode, heterogeneous product due to inconsistent plasma, high metal contamination and overheated surrounding water.

2.2 Experimental Procedures

Materials All the chemicals were of analytical grade and used without further purification. High-purity (99.9%) graphite rods (6'' in length and ¼'' and ½'' in diameter) were purchased from McMaster-Carr.

Thermogravimetric analysis (TGA) TGA of the samples was conducted on a Thermal Analysis Hi-Res TGA 2950 instrument. In a typical run 3–5 mg of the sample was loaded in a platinum pan. For all the analyses Hi-Res dynamic (ramp 50 °C min^{-1}, res 4.0 °C to 1000 °C) was used under constant airflow (60 $mL.min^{-1}$)

Electron microscopy Size and morphology of the samples were imaged using transmission electron microscopy on a JEOL 2010F.

X-ray diffraction Diffraction patterns of the samples were collected on a Bruker D8 Discover diffractometer using Cu-Kα radiation (40 kV, 40 mA). Samples were scanned over a 2 θ range 10°−60° in a step-scan with 0.05°/step.

Instrumentation

In present modifications to our graphite arc process, the manual arc apparatus (**Type I**) was replaced by an automated apparatus (**Type II**). In the **Type II** apparatus, an DC motor was attached to the nylon driver passing through a rectangular tube. The motor was controlled *via* an electrical circuit to push the anode up and down at a constant rate towards the stationary cathode. The power supply to the motor can be adjusted to the desired speed to maintain optimum gap between the electrodes. High-purity graphite rods (McMaster-Carr, 99.9% C) were used as anode and cathode.

An arc voltage difference of ±5 V is maintained using appropriate resistance, so that beyond it the motor moves in opposite direction to maintain a narrow-voltage arc during A-CNOs synthesis. These modifications improve the ease to operate the apparatus for long period of time, enabling a higher and consistent synthetic output rate as compared to **Type I** manual apparatus.

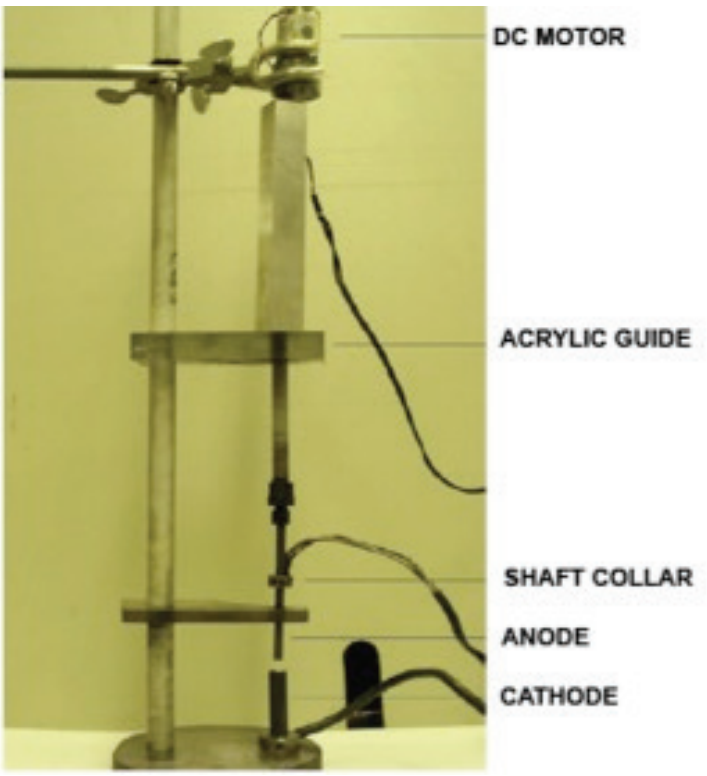

Figure 2.2. Type II automated arc-discharge apparatus for A-CNO synthesis

We have designed another automated apparatus to keep the electrical contact between the shaft collar and the anode away from the water used during A-CNO synthesis. In this **Type III** apparatus some important modifications were made to prevent the electrical contacts from the surrounding water. The anode was enclosed in a 2'' diameter glass hollow cylindrical sheath. Instead of a single shaft collar, four electrical terminals running through the carrier guide were used to pass current through the anode.

These terminals were fixed in a contact assembly made of PVC. A narrow gap was maintained between the ¼'' anode and the inner surface of the contact assembly. Two O-rings of different diameters were used to plug the contact assembly inside the hollow cylinder and to prevent surrounding water from touching the anode contacts in it. At the bottom of the contact assembly, a ceramic O-ring was attached to prevent overheating of

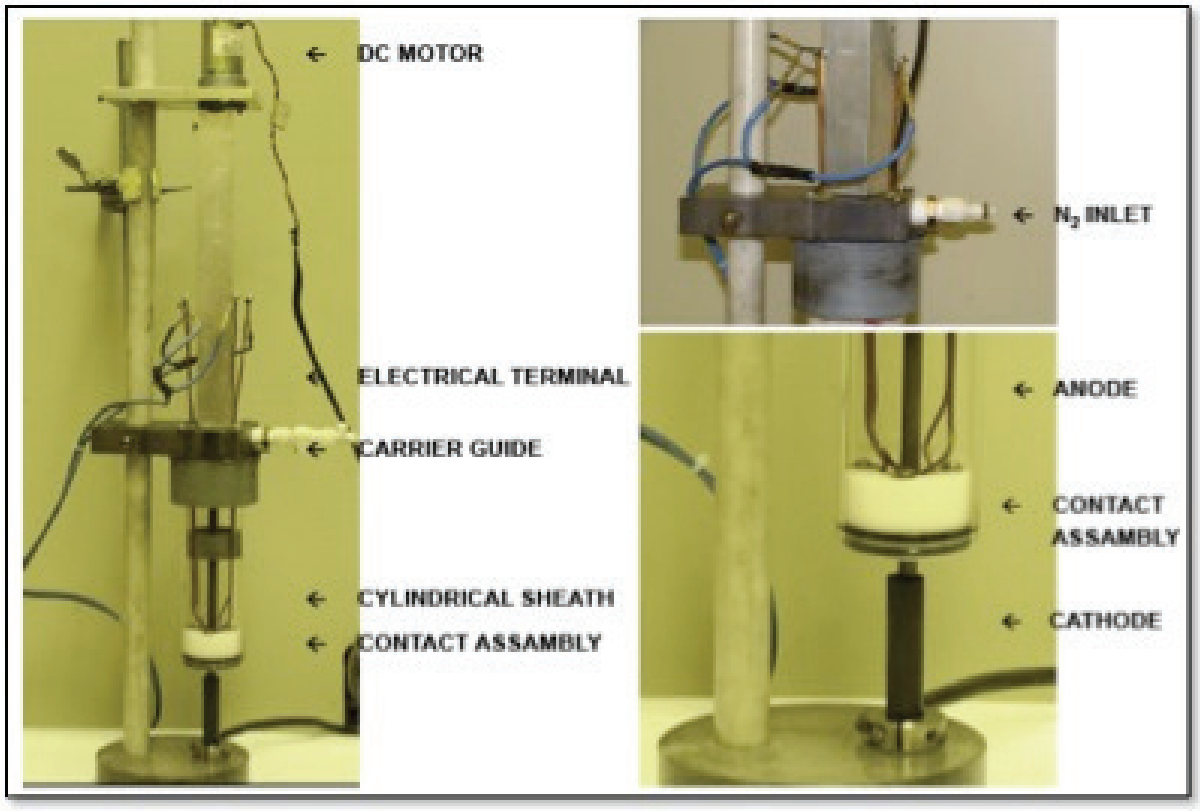

Figure 2.3. Type III automated arc-discharge apparatus for A-CNO synthesis.

the contact assembly from the high temperature produced during arc discharge. A gas inlet was installed in the carrier guide to maintain positive gas pressure inside the cylindrical sheath. The electric circuit was also programmed to maintain 20-30% duty cycles to control the arc as well as to prevent the surrounding water from overheating.

2.3 Synthesis and comparison of A-CNOs at different powers

A-CNOs were prepared at a range of arc powers using the newly developed discharge apparatus. The experiment was designed to compare the quality of A-CNOs formed under different arc powers. Four sets of experiments were carried out at 465 W (30 A, 15.5 V), 825 W (50 A, 16.5 V), 1327 W (75 A, 17.7 V) and 2016 W (105 A, 19.2 V). In a typical experiment, 3 L of distilled water was taken in a 4 L Pyrex beaker surrounded by a jacket through which cold water was continuously flowed. The apparatus (**Figure 2.3**) was lowered to the bottom of the beaker and N_2 was passed through the nozzle. The N_2 pressure was maintained in such a way that water did not rise to contact the anode and the terminal connections inside the hollow tube. Required power was supplied from a Dual MIG 151T/2 welding machine and desired duty cycle was programmed using the control box. For all these batches, 30% duty cycle was maintained throughout. With increase in arc power, the increase of intensity of the plasma was observed and the anode consumption was also found to be much faster.

2.4 Results and discussion

TGA analysis was done for the A-CNOs prepared at different arc powers. A comparison of combustion temperatures of A-CNOs prepared at 825 W, 1327 W, 2016 W using **Type II** arc apparatus and the raw anode graphite particles are shown in **Fig. 2.4**. A-CNOs prepared at higher arc power have higher onset combustion temperature. TGA data are compiled in T**able 2.1**.

Table 2.1. TGA data of A-CNOs prepared using **Type II** arc apparatus, and graphite anode.

Sample	Arc power (W)	Sample Name	Combustion Temperature (°C)	Residue (%)
A-CNO	825	A-CNO@825W	594.4	9.05
A-CNO	1327	A-CNO@1327W	669.0	3.61
A-CNO	2016	A-CNO@2016W	730.9	3.38
Anode	---	Raw anode	753.1	0.807

The gradual increase of onset combustion temperature for A-CNOs with increase in arc power may be due to several reasons, including:

- Loss of surface defects
- Metal contamination
- Contamination with graphite particles dislodged from the electrodes during high-power arc
- Formation of other nanocarbons, such as CNTs and CNT-like structures.

The derivative TGA plots of A-CNO samples are much broader than raw anode particles. This indicates that A-CNO samples are heterogeneous mixtures and/or there are broad distributions of particle size and/or range of defects in its surface.

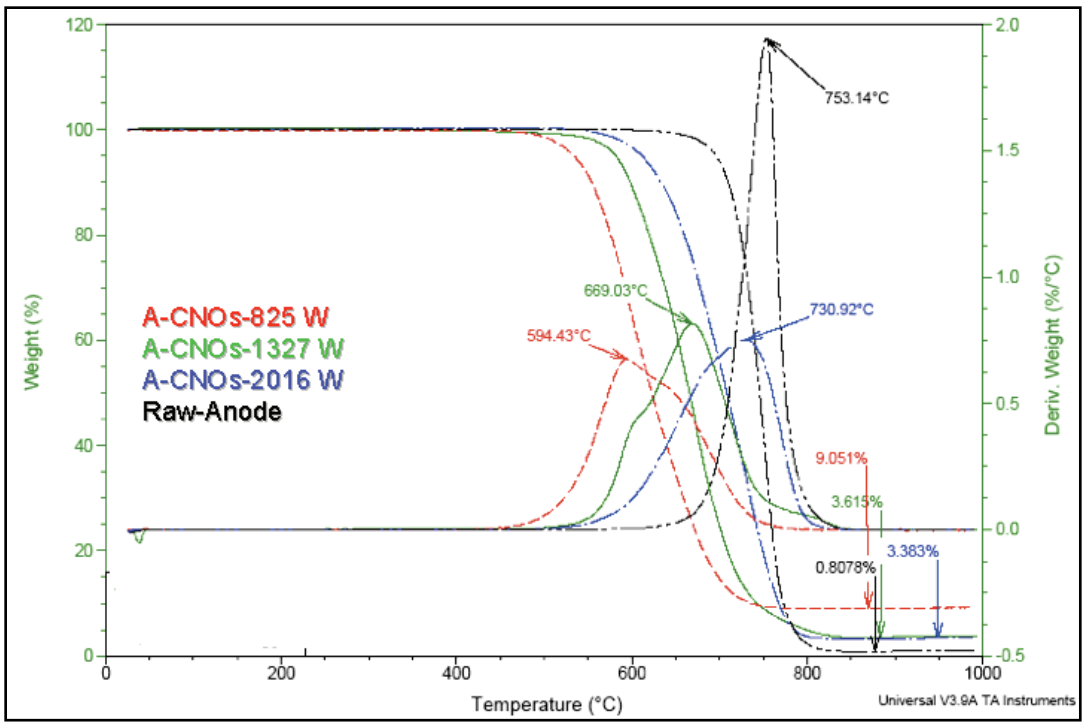

Figure 2.4. TGA (air) overlay of A-CNOs prepared at different arc power (825 W, 1327 W, 2016 W) using Type II arc apparatus and anode particles.

Moreover, the combustion residues for A-CNOs are significantly higher than for pure anode particles. This is due to metal contamination, mostly from the loose connection of the anode and shaft collar. The shaft collar had to fit loosely enough so that the anode could be driven toward the cathode continuously without much struggle. Thus the continuous sparks produced from the stainless steel contaminate the sample with metal impurities. TGA data are consistent with the increase in residue with decrease in arc power. Since at low arc power much longer time is required to consume the anode resulting more metal contamination from continuous sparks at the shaft collar and anode connection. To minimize the polydispersity of A-CNO samples and the metal impurities we redesigned the arc apparatus. The modified Type III apparatus is shown in Fig. 2.3.

Using **Type III** automated apparatus A-CNOs were again prepared at different arc power and TGA analysis (**Fig. 2.5**) were done under air. TGA data obtained for these sets of A-CNOs are compiled in T**able 2.2**.

Table 2.2. TGA data for A-CNO samples using Type III arc apparatus and for graphite anode.

Sample	Arc power (W)	Sample Name	Combustion Temperature (°C)	Residue (%)
A-CNO	465	A-CNO@465 W	623	2.8
A-CNO	825	A-CNO@825 W	662	2.2
A-CNO	1327	A-CNO@1327 W	663	2.4
A-CNO	2017	A-CNO@2016 W	680	2.7
Anode	---	ANODE	775	0.8

TGA analyses are consistent with gradual increase in onset combustion temperature from 825 W to 2016 W as observed for samples prepared using **Type II** apparatus. However, for all the A-CNO samples prepared using **Type III** apparatus at different arc power, considerably lower residues are observed. Also the percentages of the residues from different batches are quite consistent. The derivative peaks due to mass loss of A-CNOs are much sharper, indicating better homogeneity in the sample.

To further study the size and morphology of the A-CNOs at different arc power HRTEM analysis was carried out. HRTEM images obtained from different parts of the samples at 825 W, 1327 W and 465 W are shown in **Fig. 2.6**, **Fig. 2.7** and **Fig. 2.8** respectively.

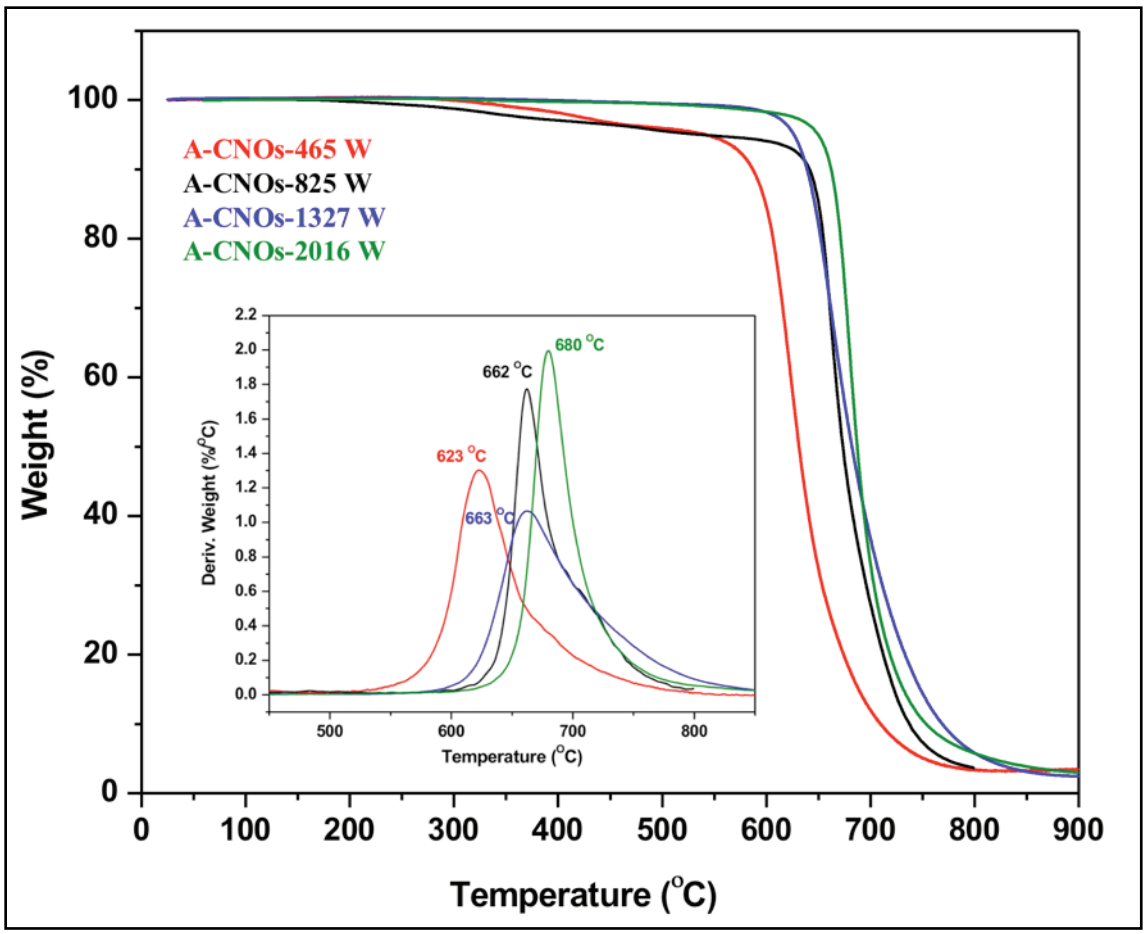

Figure 2.5. TGA (air) overlay of A-CNOs prepared at different arc power **(465 W, 825 W, 1327 W, 2016 W)** and **anode** using **Type III** arc apparatus.

A-CNOs were formed predominantly at the arc voltage of 825 W and 1327 W, while at 465 W polygonal particles were predominant. Samples prepared at 2016 W contained a heterogeneous mixture of amorphous and graphitic carbon as major components and a few CNOs along with CNTs. A-CNOs synthesized in our experimental conditions are 20–40 nm in diameter and MWNTs are also commonly observed in these samples. Moreover, A-CNOs are not always spherical and consist of many polyhedral, layered structures.

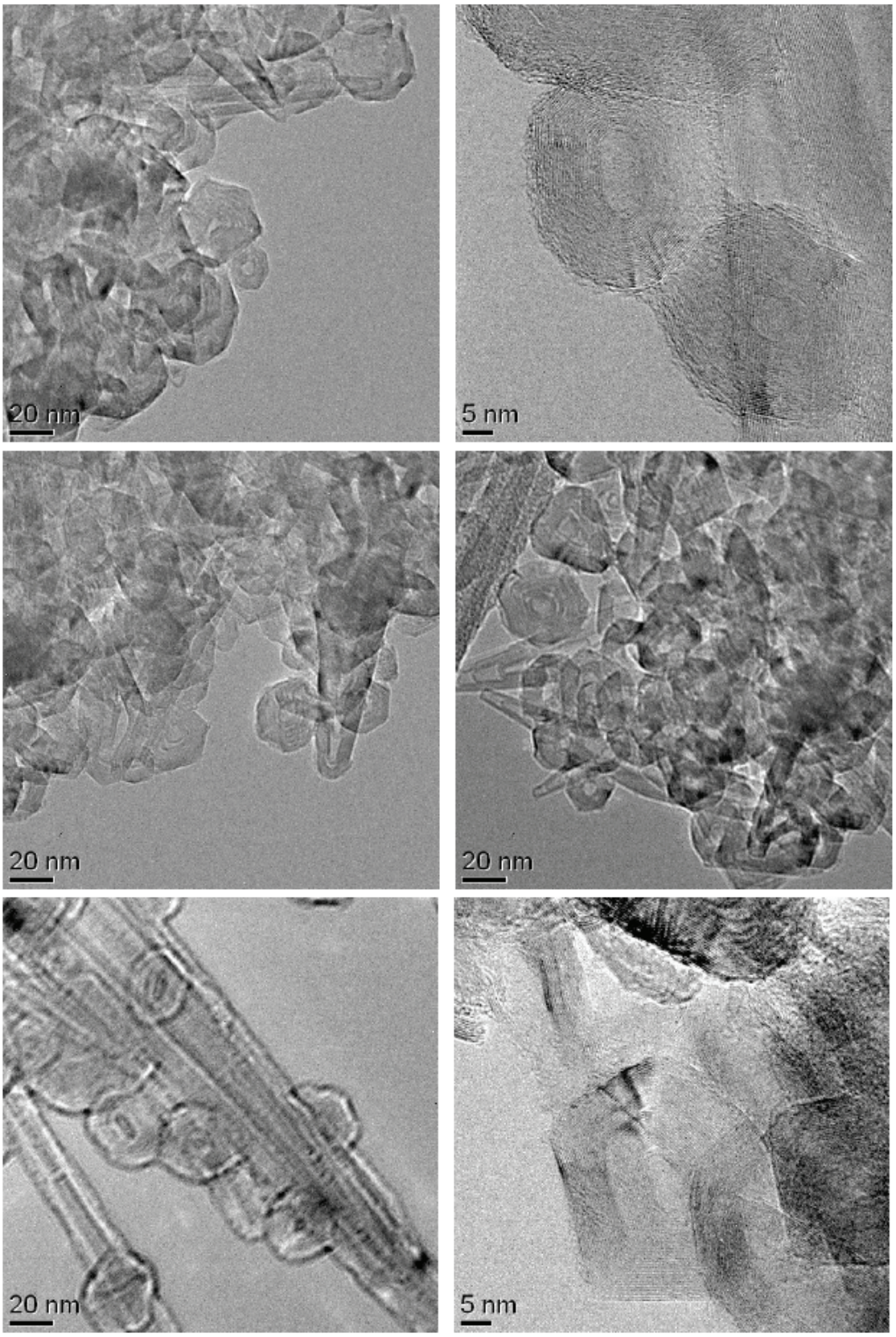

Figure 2.6. HRTEM images of A-CNOs at 825 W arc power.

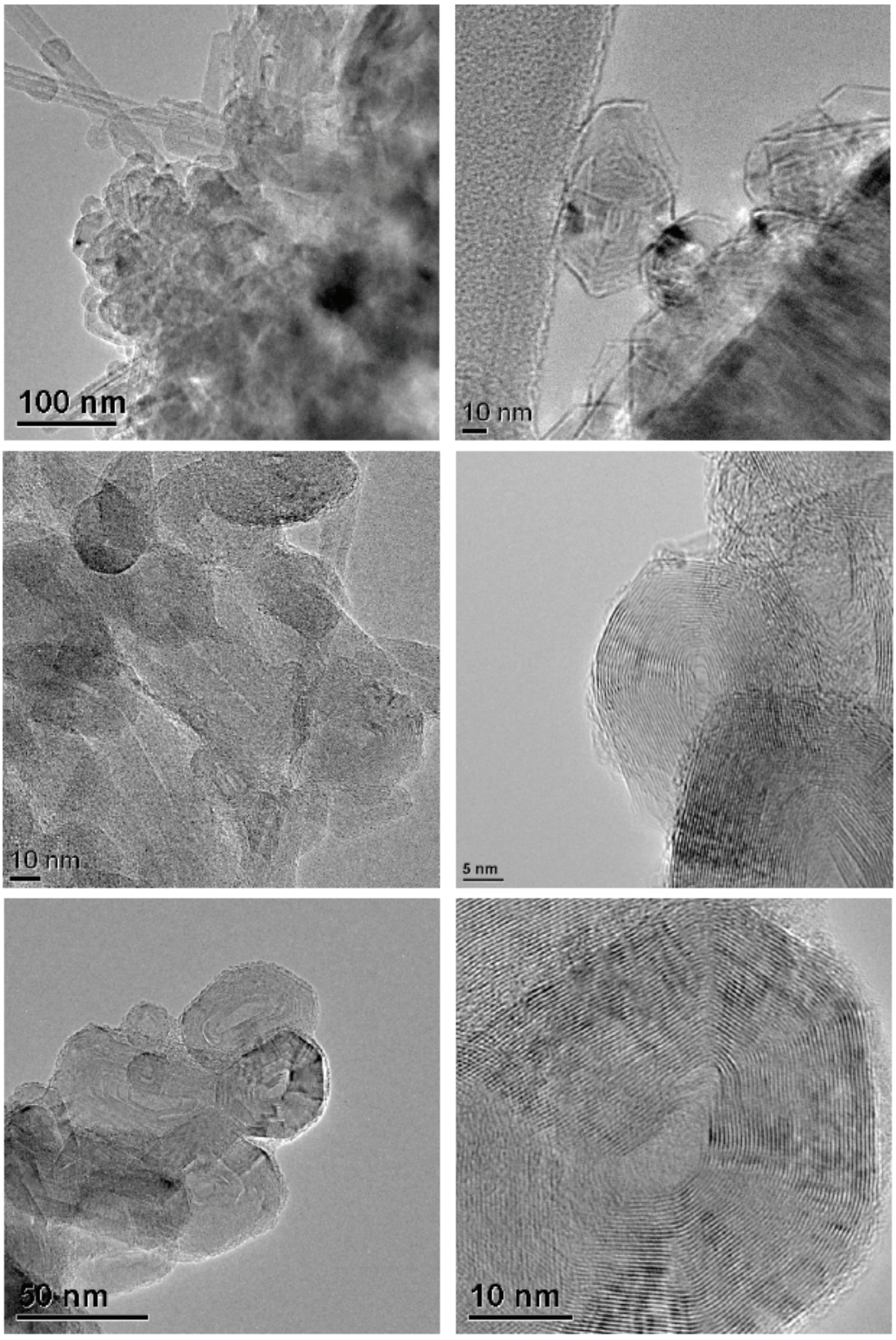

Figure 2.7. HRTEM images of A-CNOs at 1327 W arc power.

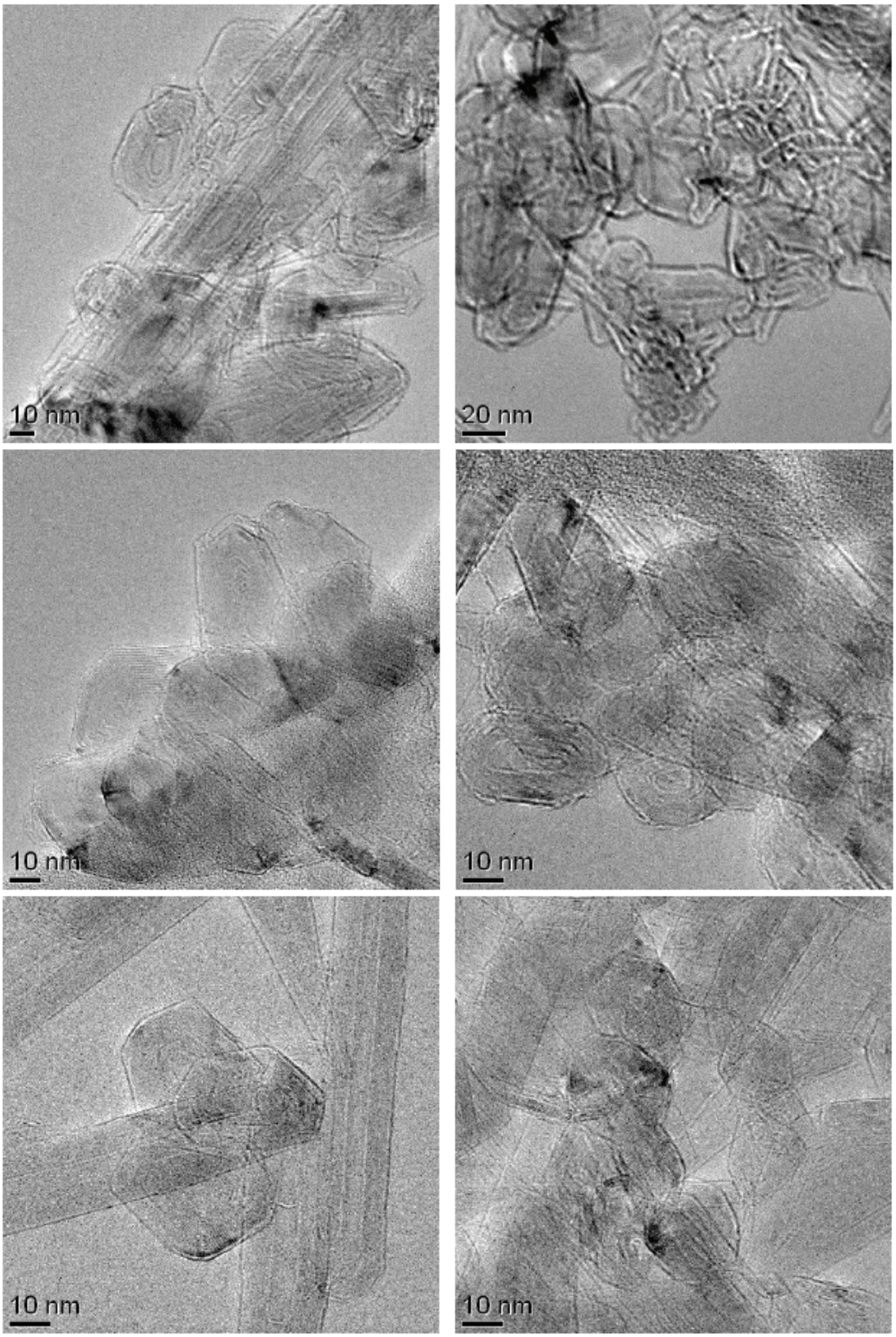

Figure 2.8. HRTEM images of A-CNOs prepared at 465 W arc power.

Powder XRD studies (**Fig. 2.9**) were done on A-CNOs synthesized at different arc power to find any change in the interlayer spacing of concentric layers. As an internal reference 10 wt. % CaF_2 was spiked into the samples to calibrate the (002) peak position. A typical graphite (002) diffraction peak was observed for all the samples at 2 θ = 26°. Using Bragg's equation, interlayer spacing (d_{002}) was calculated; with increasing arc power, the average interlayer d_{002} spacing in A-CNOs decreases from the usual value for CNOs (3.4 Å) to pure hexagonal graphite (3.354 Å) (**Table 2.3**). The *d*-spacings are similar for samples prepared at 465 W, 825 W and 1327 W, but A-CNOs prepared at 2016 W showed substantial deviation. The (002) peak of samples prepared at 465 W, 825 W and 1327 W was relatively broad and centered at 2 θ = 26.0 °, while the (002) diffraction of 2016 W sample was sharp and centered at 2 θ = 26.5 °, corresponding to an interlayer spacing (d_{002}) of 3.40 Å for 465 W, 825 W and 1327 W samples, but 3.35 Å for the 2016 W sample. The deviations of *d*-spacings indicate more graphitic nature of the samples prepared at higher arc power.

The domain crystallite sizes of A-CNOs can be determined from L_a (longitudinal crystallite size along a-axis) and L_c (thickness of crystallite along c-axis). According to Scherrer's equation:

$$L_a\,(L_c) = k\,\lambda\ /\mathrm{B}\cos\theta$$

where k = Scherrer constant = 0.94 for (002) and 1.84 for (100); X-ray wavelength = λ = 0.15406 nm for Cu K_α radiation; B = full width at half maximum = FWHM in radians; θ = diffraction angle in radians. L_c corresponds to the (002) peak at 2θ = 26.5° and L_a corresponds to the (100) peak at 2θ = 44°.[40]

Table 2.3. d_{002} spacing and crystallite parameters of A-CNOs prepared at different arc power.

Sample	A-CNO	A-CNO	A-CNO	A-CNO	Anode
Arc power	465 W	825 W	1327 W	2016 W	---
d_{002} (Å)	3.43	3.43	3.42	3.38	3.36
L_c (nm)	9.8	11.1	10.6	30.8	–
L_a (nm)	6.6–19.4	13.6–17.9	12.3–16.6	13.3–22.1	–

Due to the very broad peak at 2 θ = 44°, L_a values determined from the (100) plane are only a rough estimate. For better results, L_a must be determined from Raman spectra using Knight's formula.[41]

$$\boldsymbol{L_a(\mathrm{nm}) = 4.35\left(\frac{I_D}{I_G}\right)^{-1}}$$

The interlayer spacing d_{002} in A-CNOs decreases and the crystallite height L_c increases with increasing arc power. This correlates with high-temperature shrinking of graphitic layers of carbon fibers reported by other groups.[42] Wider variations of L_a were observed for the 465 W and 2016 W samples compared to the 825 W and 1327 W samples. This indicates that better control of the arc plasma at 825 W and 1327 W produces A-CNOs with narrower dispersity.

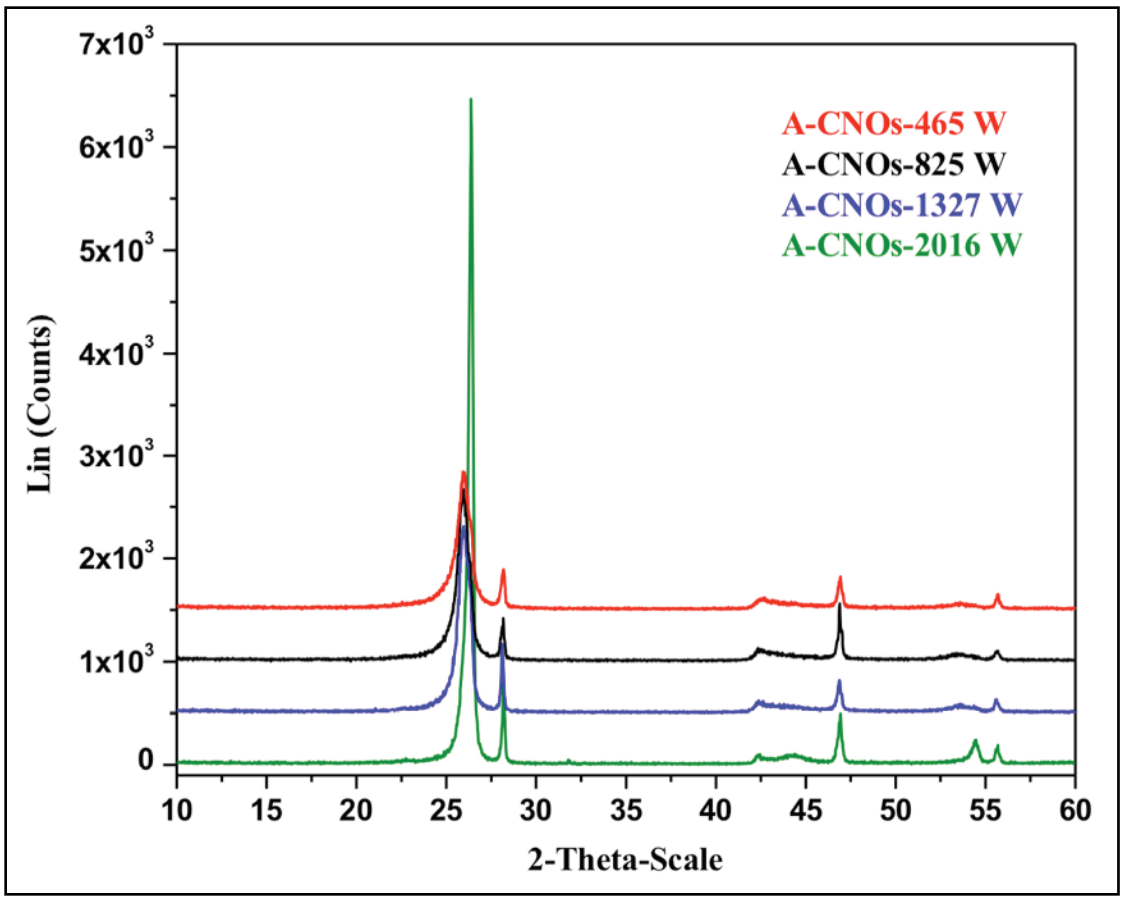

Figure 2.9. XRD of A-CNOs synthesized at different arc power A) 465 W; B) 825 W; C) 1327 W; D) 2016 W. CaF_2 calibration peaks are at 2□= 28°, 47° and 56°.

Raman spectroscopic analysis was also conducted to investigate the effect of arc power on the growth of A-CNO. Raman spectroscopy is a sensitive and powerful technique to monitor the level of defects and the microstructure of carbon materials. The Raman peak intensity ratio (I_D/I_G) of the disorder band (D at ~1350 cm^{-1}) and the graphitic band (G at ~1580 cm^{-1}) correlates with the density of exposed edge planes in carbon materials. Figure 2.10 shows Raman spectra measured at multiple spots of A-CNOs prepared at 4 different arc powers (465, 825, 1327 and 2016 W). The spectra were normalized by the G peak intensity. This result shows that arc power dramatically

influences the growth of A-CNOs. At 465 W (Fig. 3.1.4a), the Raman spectra showed widely varying peak width, peak height and I_D/I_G. I_D/I_G determined at different spots ranged from ~ 0.2 to 0.8, indicating that the produced carbon samples are heterogeneous. High I_D/I_G (~ 0.8) corresponds to highly disordered, amorphous carbon.[43]

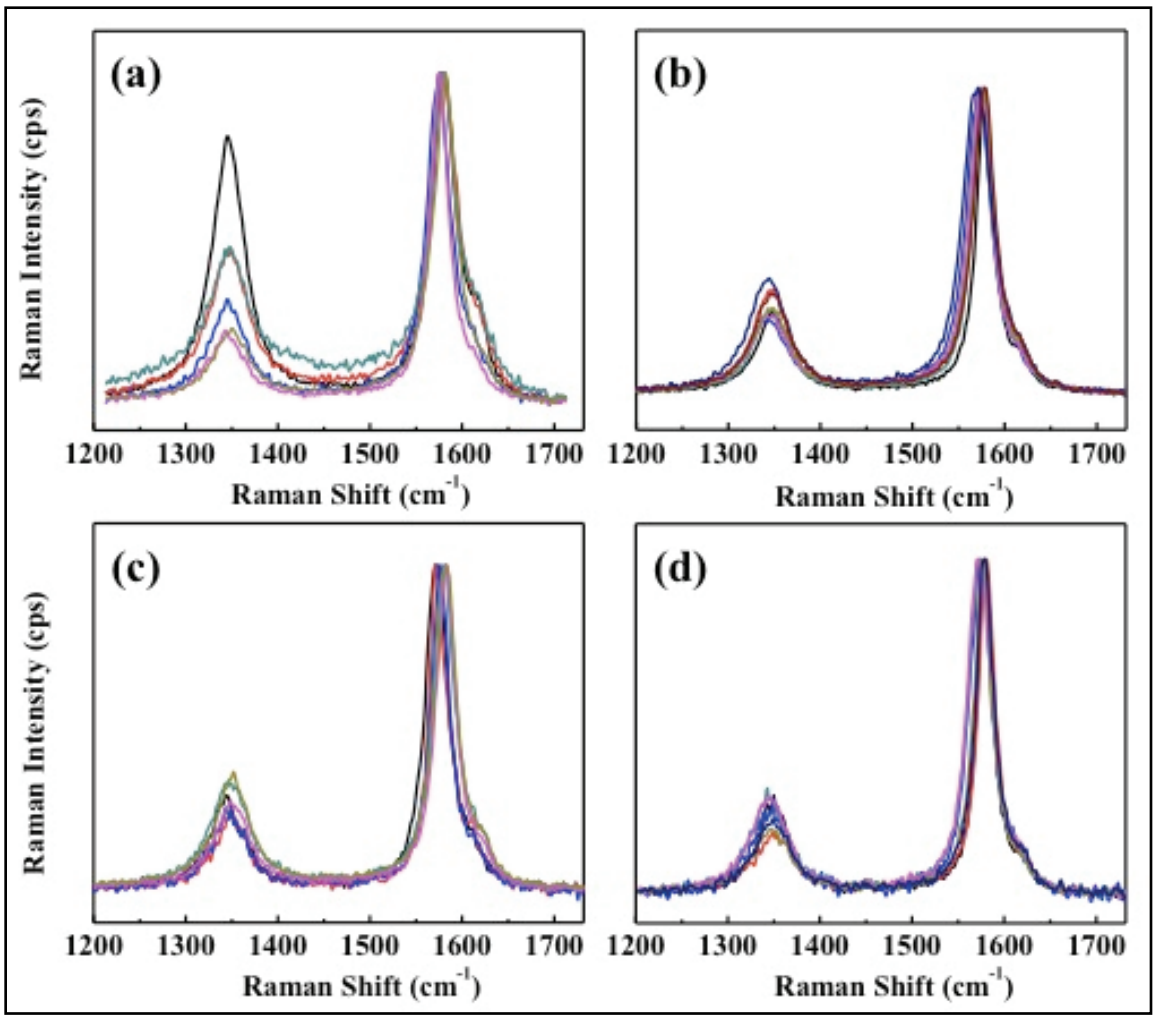

Figure 2.10. Raman comparison of A-CNOs prepared at four different arc powers

At the higher arc powers (825–2016 W), the Raman spectra showed much less variation as the A-CNO-producing arc becomes more controlled. The average value of I_D/I_G was 0.20, 0.20 and 0.15 at 825 W, 1327 W and 2016 W, respectively. The smallest

I_D/I_G value at 2016 W implies that A-CNOs may convert into microstructurally more ordered (less defective) graphite at high power. This is consistent with the trend observed by TGA, XRD and HRTEM.

The TGA, Raman, XRD and HRTEM results consistently indicate that synthesis of A-CNOs at 465 W is poorly controlled, resulting in amorphous carbon impurities, but synthesis at 2016 W results in more graphitic impurities. Thus, arc power in the range of 825 W to 1327 W is optimal for producing pure A-CNOs in high yields. These A-CNOs are well crystallized with an average diameter of 20–40 nm, consisting of about 25–35 graphitic layers with a spacing of ~3.4 Å between two neighboring lattice fringes. A-CNOs prepared under our experimental conditions have both spherical and polyhedral shapes. The irregular hollow cores of these A-CNOs are as large as 10-12 nm. Because synthesis at 825 W leads to a narrower size distribution and fewer graphite impurities, 825 W is preferred over 1327 W.

2.5 Summary

A-CNOs were successfully synthesized using the underwater arc-discharge method. A manual arc-discharge apparatus was replaced by an automated apparatus. Various modifications to the automated apparatus and the synthesis conditions were made to optimize A-CNO production. The modified **Type III** apparatus allows control over the duty cycles, voltage tuning, and the anode movement. Elimination of metal impurities and control over the plasma produces better homogeneity and less contamination in the samples. The desired arc power, required for maximize production, was optimized by studying the thermal stability and the morphology of the A-CNOs

produced at different arc power. Arc power in the range of 825 W was found to be more consistent in producing homogeneous A-CNO samples.

Chapter III: Purification of A-CNOs

3.1 Introduction

Arc-produced CNOs inevitably contain large amount of carbonaceous impurities such as polycyclic aromatic hydrocarbons, amorphous carbon, CNTs, and graphitic carbon along with small quantities of metal impurities. In the arc-discharge preparative method, carbonaceous impurities originate from unvaporized graphitic particles that have fallen from the graphitic rods and from the uncontrolled formation of other nanostructures. It is very important to get rid of these impurities to facilitate fundamental research and targeted application of CNOs. Many research groups have reported efficient methods to purify carbon nanomaterials. Since research in CNOs is not very mature as compared to CNTs, different approaches have been made based on the techniques developed so far for CNTs. Considerable progress has been made in purification methods based on both chemical and physical properties of nanoparticles and the possible impurities. These methods have their own advantages and limitations. Minute quantity of fullerenes can be easily removed based on their solubility in organic solvents. Polycyclic aromatic hydrocarbons and amorphous carbon could be easily eliminated by mild oxidation because of their high density of defects.[44] A problem arises from the large portion of graphitic particles and metal contamination. CNTs are usually found as an impurity in the case of CNOs prepared by the arc-discharge method. Another problem arises from the wide range of size and morphology in carbonaceous and metal impurities generated based on preparation techniques. These factors make it difficult to develop highly efficient, common purification methods. Purification methods developed so far for CNTs can be categorized as physical, chemical, and a combination of both.

Chemical methods purify CNTs based on the idea of selective oxidation. The high oxidative activity of amorphous carbon is due to the presence of more prismatic faces per unit volume and structural defects, while the high reactivity of the CNTs and CNOs can be attributed to their large curvature and pentagonal carbon rings.[45] The etching rate of amorphous carbon is faster than that of nanoparticles,[46] Thus selective oxidation is an efficient method to remove amorphous carbon. Chemical oxidation can be done in the gas phase (O_2, Cl_2, H_2O, mixture of Ar and O_2, mixture of O_2, SF_6 and $C_2H_2F_4$, etc.), the liquid phase (refluxing acidic solution) or to some extent *via* electrochemical oxidation.[44]

Ebbesen *et al.* first reported gas-phase purification of MWNTs by oxidizing in air at 750 °C for 30 min, but they reported a recovery of only 1–2 wt.%[47] resulting from uneven exposure of the nanoparticles to air and poor selectivity for CNTs over other carbonaceous impurities. The yield of this method was improved to ~35 wt.% by Park *et al.* by limiting the sample quantity and rotating the furnace tube while annealing at high temperature.[48] This method is very convenient although it cannot remove metallic impurities. Thus arc-prepared samples with minimal metal impurities are best suited for this purification method. However, other limitations due to agglomeration of nanoparticles that prevents even exposure to oxidizing atmosphere and low selectivity due to narrow combustion stability of carbon nanoparticles (CNPs) with graphitic particles have to be overcome before using gas-phase oxidation for bulk purification.

In liquid-phase oxidation, various oxidizing agents such as HNO_3, H_2O_2, Br_2 or $KMnO_4$, often in combination added strong acids, are commonly used to remove amorphous carbon and metal impurities from CNTs.[49, 50] Nitric acid is commonly used in

liquid-phase oxidation due to its mild oxidation and selective removal of amorphous carbon. Under acidic condition, metal impurities can be removed by dissolution. However, acid treatments often damage surface structure and introduce functional groups (-OH, -C=O, -COOH etc.).[51] Thus, careful choice of acid, concentration, time and temperature are the key factors to maximize yield and to minimize surface damage.

Other types of purifications based upon the physical properties such as differences in size, aspect ratio, solubility, thermal stability and electronic or magnetic properties of constituents in the sample have led to the extensive study on methods such as chromatography,[52] centrifugation, electrophoresis,[53] field-flow fractionation (FFF)[54] and high-temperature annealing (graphitization)[55]. Most of these methods require high dispersion of materials, which is often difficult to achieve. Use of surfactants to disperse CNTs *via* ultrasonication and then separation of purified nanotubes has been reported. In another approach, polyoxometalate (POM) compounds are used for their preferential adsorption on graphitic surfaces through electrostatic interactions, thereby keeping nanoparticles in dispersion while separating amorphous and metal impurities.[56] The main advantage of these methods is the retention of structural morphology, while limitations include poor selectivity resulting in retention of carbonaceous impurities, requirement of high dispersability and limited scale of sample processability. Thus, owing to diversity of as-produced CNPs in terms of size, morphology and types of non-carbonaceous impurities, proper combinations of physical and chemical methods are required to obtain desired purity.

3.2 Experimental Procedures

3.2.1. Air-cleaning at high temperature

A-CNOs were prepared under the arc power of 825 W as discussed in the previous chapter. These A-CNOs were placed in a ceramic dish and annealed at 450 °C in a General Signal Lindberg/Blue tube furnace under constant airflow. Annealing was done for 4 h and then the sample was cooled to room temperature. No specific controlled temperature program was used to anneal as-produced A-CNO samples.

3.2.2. Graphitization

As-produced A-CNOs were vacuum-dried overnight at 45 °C and then graphitized at 2400 °C under He for 1 h.

3.2.3. HNO_3 acid treatment

As-produced A-CNOs (0.300 g) were vacuum-dried overnight at 45 °C and then stirred in refluxing HNO_3 (3 M, 50 mL) for 12 h. Acid-treated CNOs were separated by centrifugation and washed several times with distilled water. The resulting material was vacuum-dried overnight at 45 °C, followed by annealing at 450 °C for 4 h under constant airflow.

3.2.4. Mixed (H_2SO_4/HNO_3) acid treatment along with extraction

In a typical experiment, as-produced A-CNOs (0.300 g) were washed with CS_2 in a Soxhlet extractor for 6 h. The resulting material was vacuum-dried and subsequently stirred in a refluxing mixture of H_2SO_4 (3 M, 30 mL) and HNO_3 (3 M, 20 mL) for 6 h. The CNOs were separated by centrifugation and washed several times with distilled water. The resulting material was vacuum-dried overnight at 45 °C, followed by annealing at 450 °C for 4 h under constant airflow.

3.2.5. Polyoxometalate-based purification

In a typical procedure, as-produced A-CNOs (0.500 g) were added to an aqueous solution of phosphotungstic acid (2.15 g in 500 mL H_2O, 15 mM) and horn-sonicated (100 W, 20 KHz, 50% duty cycle) for 4 h, 6 h. During sonication, an ice bath was used to prevent surface damage of the A-CNOs and to control the temperature of the dispersion. After sonication a gray suspension was obtained, which was centrifuged for 10–15 min to remove undispersed materials. The supernatant solution was filtered off to remove free POM from the dispersed materials. These materials were washed with HF (10 % v/v, 20 mL) for 36 h at room temperature to ensure complete removal of the adsorbed POM. The acidic solution was decanted and the solid material was further washed with water (3 X 100 mL) and vacuum dried overnight at 45 ºC. The material was again annealed at 450 °C for 4 h.

3.3 Results and Discussion

A-CNOs contain many carbonaceous impurities. As-prepared A-CNO samples have combustion onset temperature that vary between ~640 ºC – ~665 ºC from batch to batch. Amorphous carbon, graphitic electrode particles, carbon nanotubes and other structures were observed by using HRTEM. Metal contaminants of A-CNO samples were observed as residue after TGA analyses in air.

Air-cleaning (450 °C under constant airflow for 2–4 h) of A-CNOs results in a mass loss of 7–10 wt.%. The treatment is experimentally simple and polycyclic aromatic hydrocarbons and amorphous carbon having low combustion temperature are removed, but amorphous carbon with high combustion stability, graphitic particles, CNTs

and metal impurities remain. Our modified Type III apparatus lowers the metal contamination level. TGA analysis (Fig. 3.1) shows a slight increase in combustion onset temperature, but the broad mass loss above ~650 °C indicates the presence of carbonaceous impurities with combustion stability close to that of A-CNOs.

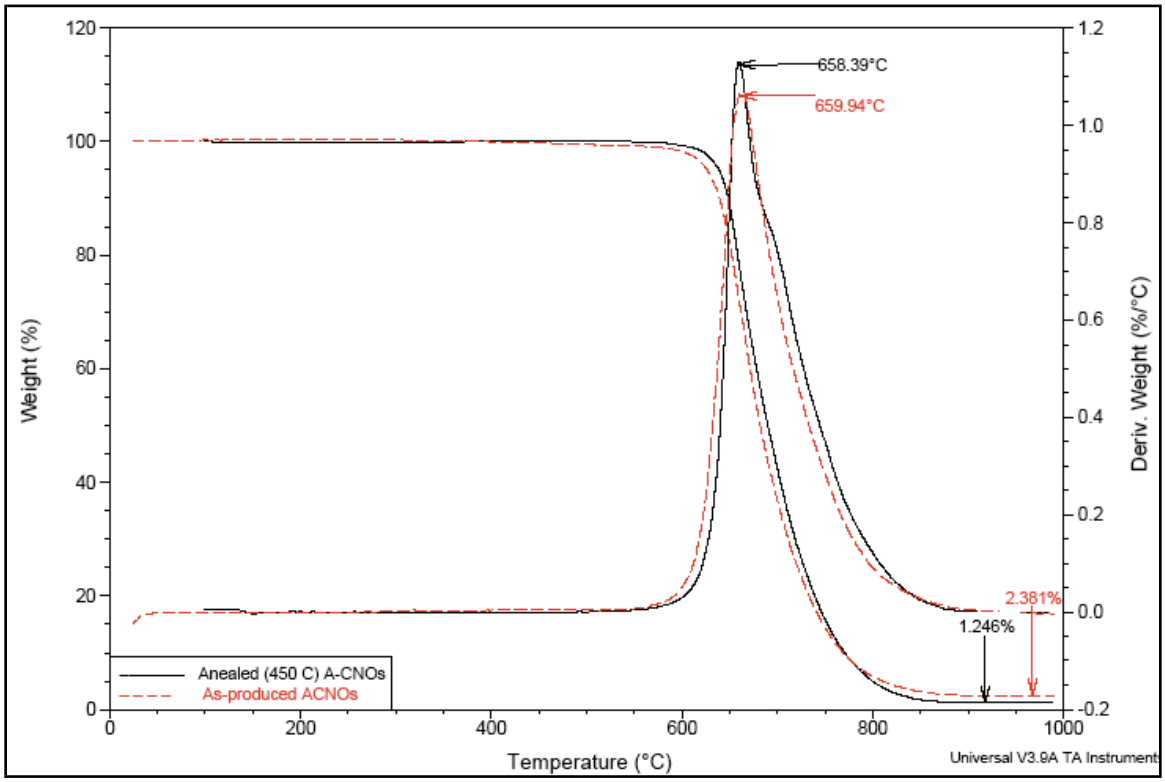

Figure 3.1. TGA compilation of **air-cleaned (450 °C) A-CNOs** and **raw A-CNOs**

Control experiments were done by physically mixing anode particles with A-CNOs in three different ratios (1:2, 1:1, 2:1) to compare their TGA behavior with A-CNOs and pure anode particles (Fig. 3.2). With increase in anode (graphite) particle contamination in A-CNO samples the onset combustion temperature of the mixture gradually increases.

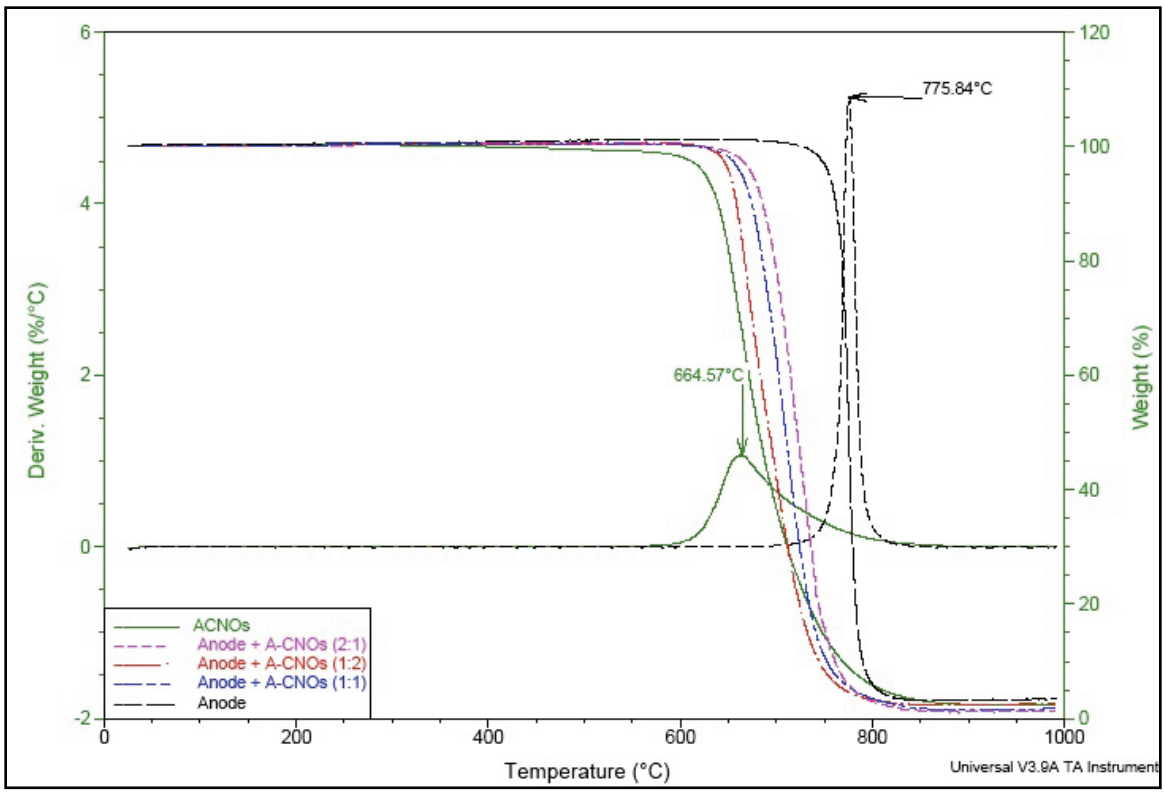

Figure 3.2. TGA overlay of **A-CNOs, anode + A-CNOs (in 2:1, 1:1, 1:2 ratios)** and **anode** particles

In another approach, graphitization of as-produced A-CNOs at 2400 °C under inert atmosphere significantly increased the combustion stability of the A-CNOs. In a typical experiment, the combustion onset temperature increased by ~100 °C (**Fig. 3.3**). This quick, convenient method removes carbonaceous and metallic impurities. A TGA plot of a graphitized sample shows a sharp derivative peak, indicating homogeneity of the sample. The downside of this method is that high-temperature graphitization completely removes the surface defects of A-CNOs, a critical requirement for chemical functionalization. HRTEM (**Fig. 3.4**) measurements on graphitized A-CNOs show smoother CNO surfaces and fewer impurities. Consistent with observations on CNTs, the remaining carbonaceous impurities become more difficult to remove after graphitization.[1]

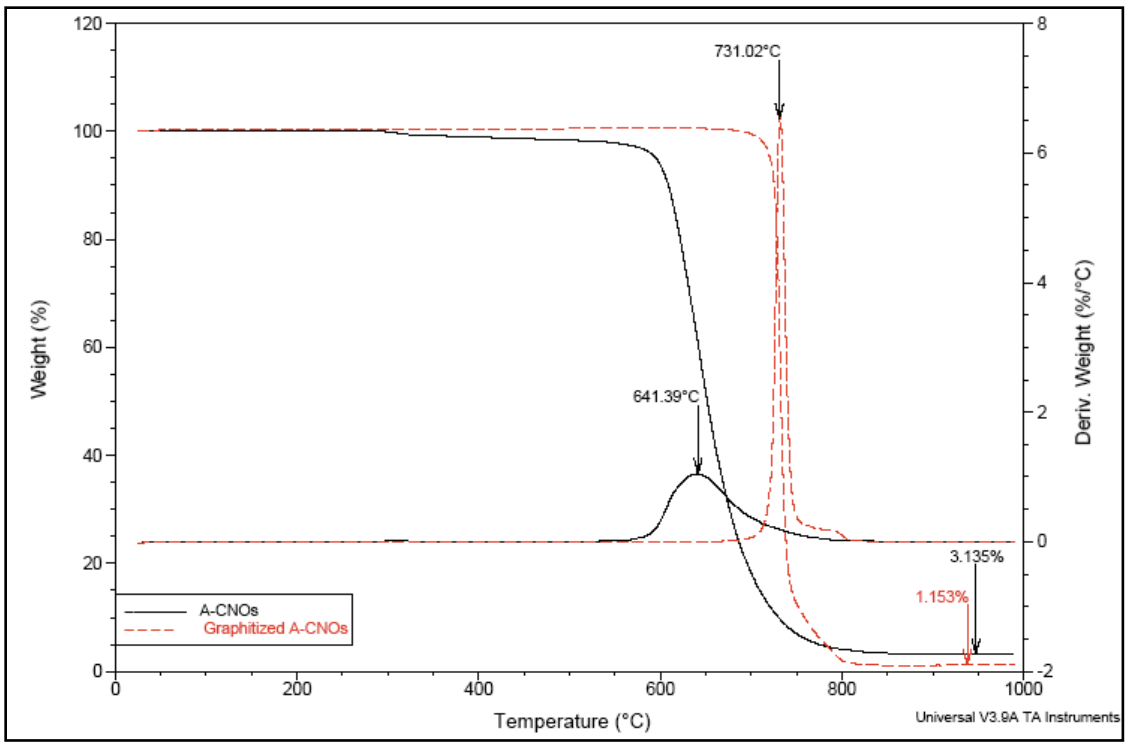

Figure 3.3. TGA overlay of **as-produced A-CNOs before and after graphitization**

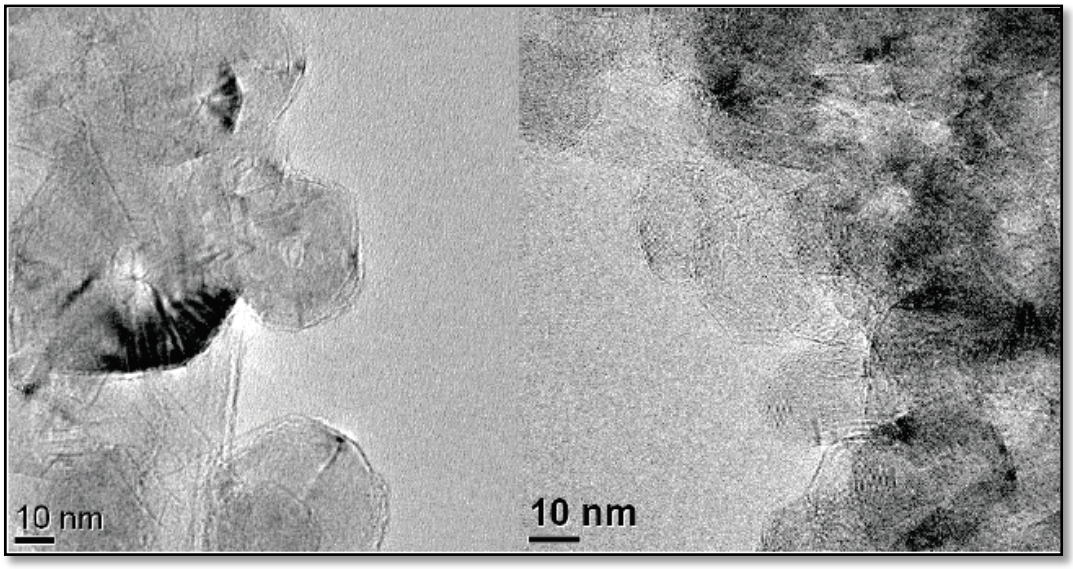

Figure 3.4. HRTEM images of A-CNOs after graphitization.

To remove these graphitic materials, as-produced A-CNOs were oxidized with 3-M nitric acid followed by annealing at 450 °C. This treatment oxidatively removed amorphous and some of the graphitic particles. Acid or hydroxyl groups attached to A-

CNO surface after acid cleaning were removed by thermal treatment. TGA analyses of A-CNOs after HNO_3 washing show increased combustion stability and derivative peak sharpness as compared to as-produced A-CNOs (Fig. 3.5). During this two-step method, chemical oxidation preferentially removes most of the defective carbons and subsequent annealing at 450 °C removes the attached reactive oxide groups on the surface, resulting in enhanced thermal stability.

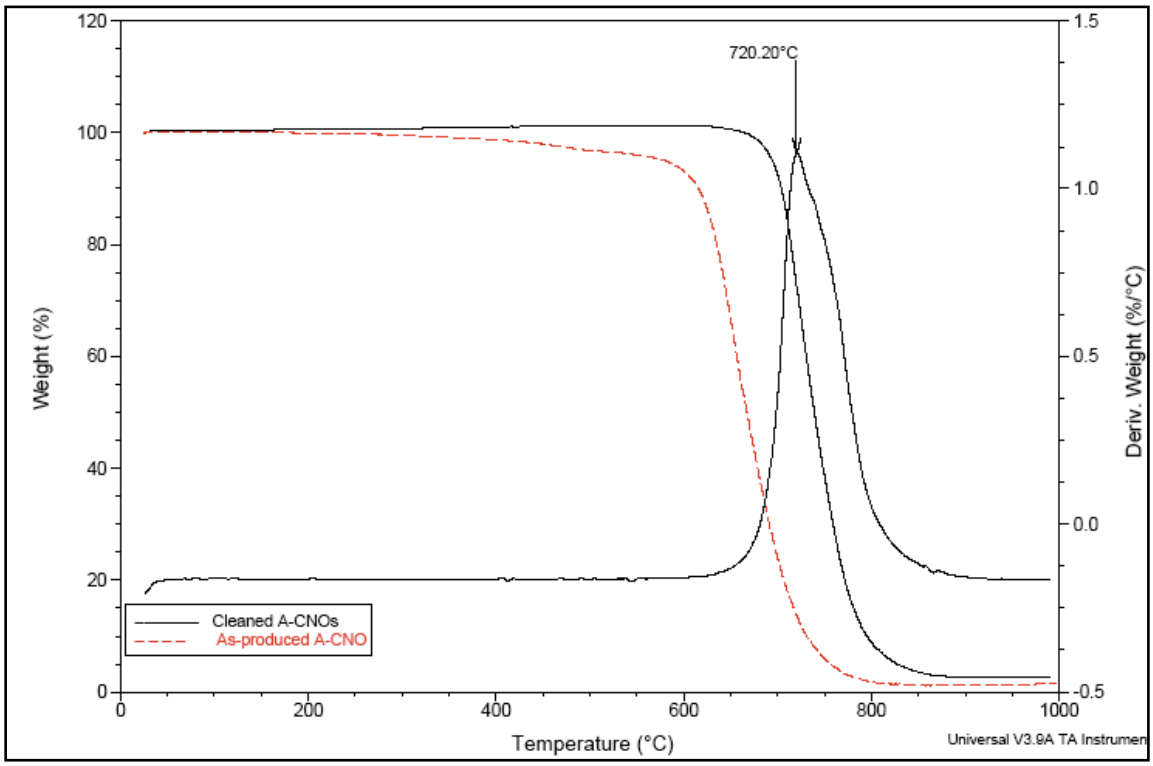

Figure 3.5. TGA overlay of A-CNO-825 W **before** and **after** HNO_3 acid cleaning

Lee *et al*. reported the effectiveness of mixed-acid treatment for SWNTs purification.[57] They found that 3:1 H_2SO_4/HNO_3 is more effective than HNO_3 (6 M) alone. We took a similar approach to A-CNOs. Washing as-produced A-CNOs with CS_2 in a Soxhlet extractor to remove soluble hydrocarbons and fullerenes, followed by

treatment with 3:2 H_2SO_4 (3 M) and HNO_3 (3 M) under reflux gave pure A-CNOs. **Fig. 3.**6 shows a flowchart of this method.

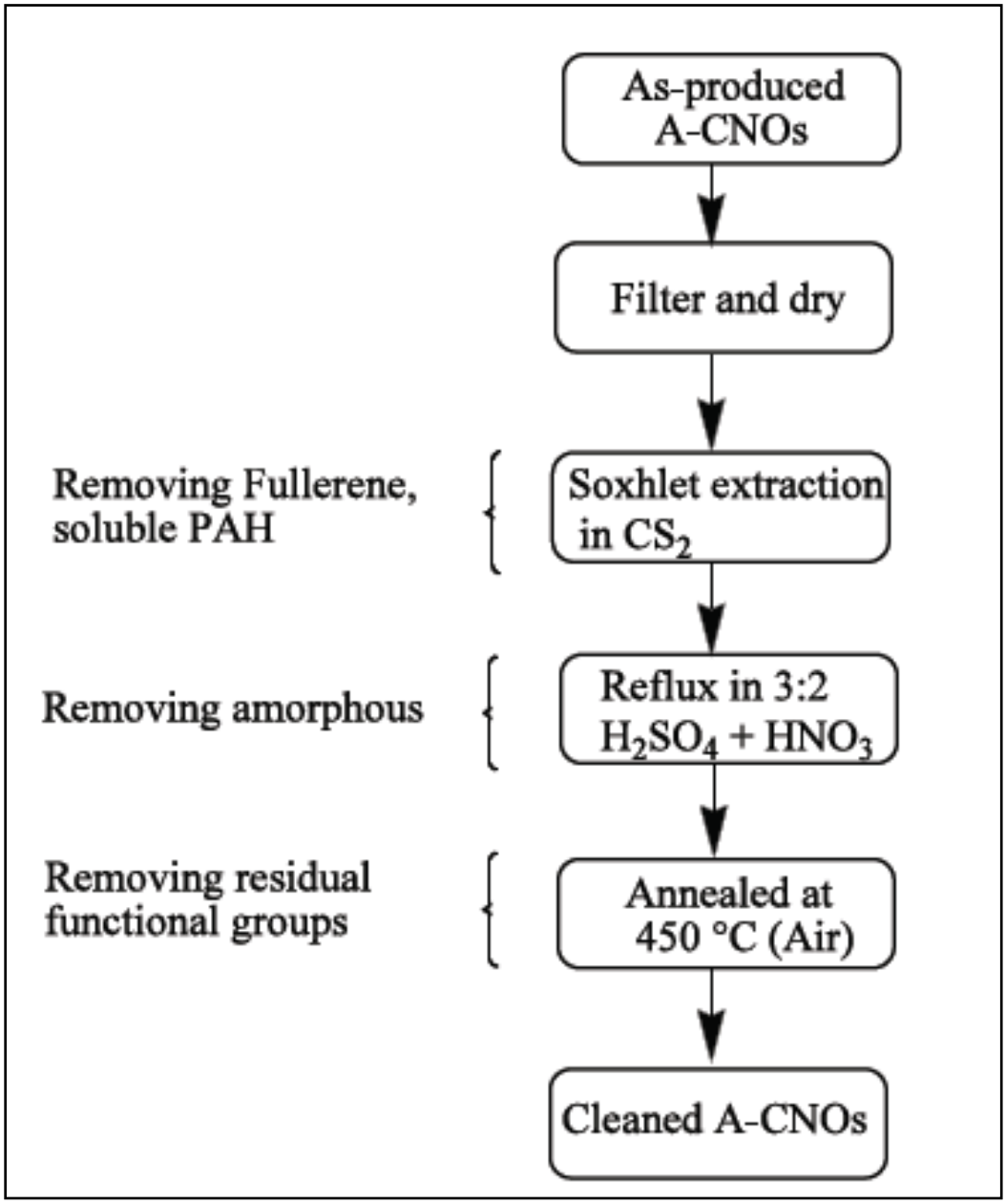

Figure 3.6. Flowchart of mixed-acid purification method

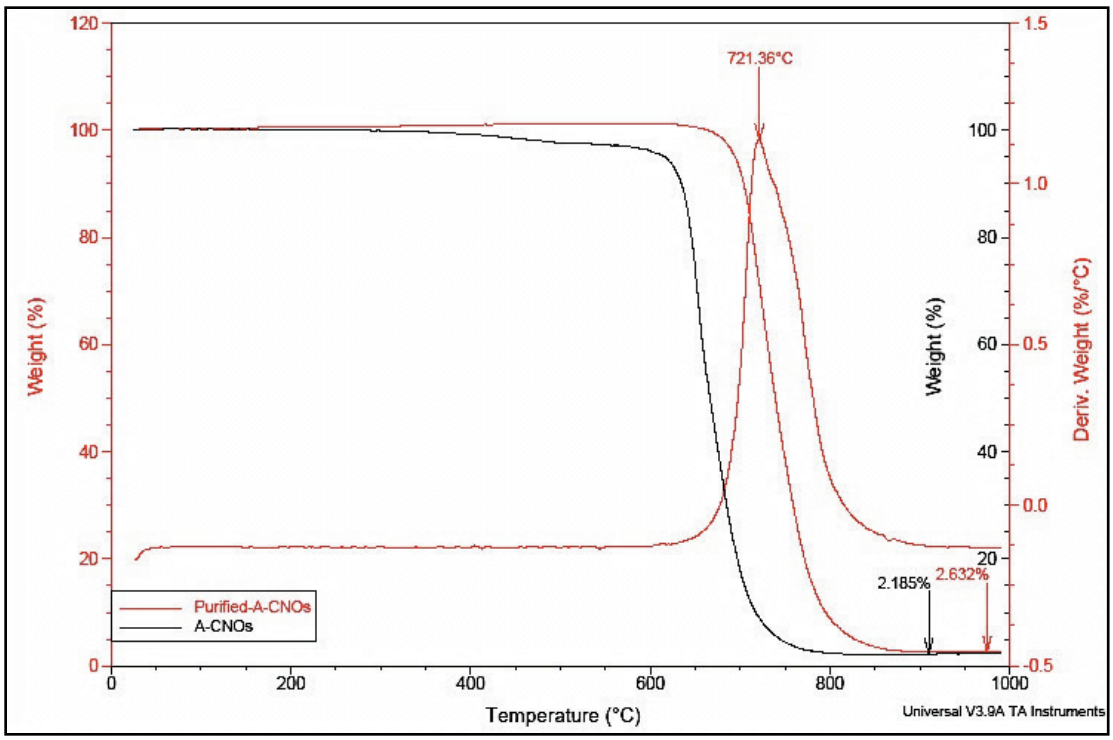

Figure 3.7. TGA overlay of **as-produced** and **mixed acid-purified** A-CNOs

Figure 3.7 shows the onset combustion temperature differences of the as-produced and purified CNOs using mixed acid treatment. The relatively broad derivative TGA plot of the purified sample indicates the presence of multiple phases in it.

Fei et al. reported the separation of CNTs from amorphous carbon impurities through adsorption of polyoxometalate (POM) on CNT surfaces, followed by further functionalization of POM-CNT composite with tin nanoparticles.[56] However, subsequent removal of adsorbed phosphotungstic acid (PWA) from CNTs was not discussed. Based on the preferential electrostatic interactions of heteropolyacids with different types of carbon surfaces, we have developed an efficient method to purify A-CNOs. **Fig. 3.10** shows a stepwise depiction of the PWA-based purification method. Each step of the purification was assayed by using TGA, Raman and HRTEM analyses to identify and quantify the isolated materials.

We made several modifications such as sonication method (bath vs. horn), sonication duration, PWA solution concentration, removing low dispersed materials via centrifugation, completely removing adsorbed PWA molecules after CNOs seperation, annealing under air to remove possible surface functional groups after purification, to Fei's CNT purification using POMs.[58] The method is optimized to selectively screen out A-CNOs from amorphous carbons, graphite debris, CNTs, and CNT like structures. Purification using phosphotungstic acid (PWA) showed different combustion behavior for dispersed and undispersed (settled) materials. In the TGA under dry air, dispersed materials showed two major mass losses at ~480 °C–515 ºC (broad) and at ~656 °C. We attribute the 480 °C–515 ºC mass loss to desorption of water of crystallization from the adsorbed PWA molecules followed by the loss of three acidic protons combined with PWA lattice oxygen as 1.5 H_2O.[59, 60] The 656 °C mass loss is due to combustion of A-CNOs. The undispersed materials showed a single-step, sharp mass loss at ~696 °C. The dispersed materials had residue of 7.5 % while undispersed materials had residue of 3.4 % (**Fig. 3.9**). The presence of PWA molecules on the surface of A-CNOs was also confirmed in EDAX measurements. These results indicate that different types of materials were clearly separated through this treatment based on preferential adsorption of PWA on different types of carbon surfaces. PWA adsorbs strongly to active carbon surfaces through proton donation,[61, 62] requiring strongly acidic conditions for removal of adsorbed PWA from CNOs.[61, 62] Another explanation of possible interaction of electron cloud of adjacent W=O with the graphitic network of carbon particles was forwarded by Fei *et al.* as shown in **Fig. 3.8.**[56]

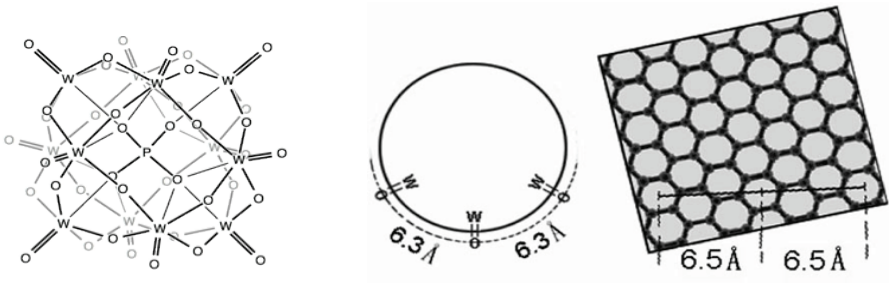

Figure 3.8. Possible interaction of $H_3PW_{12}O_{40}$ on carbon surfaces.[56]

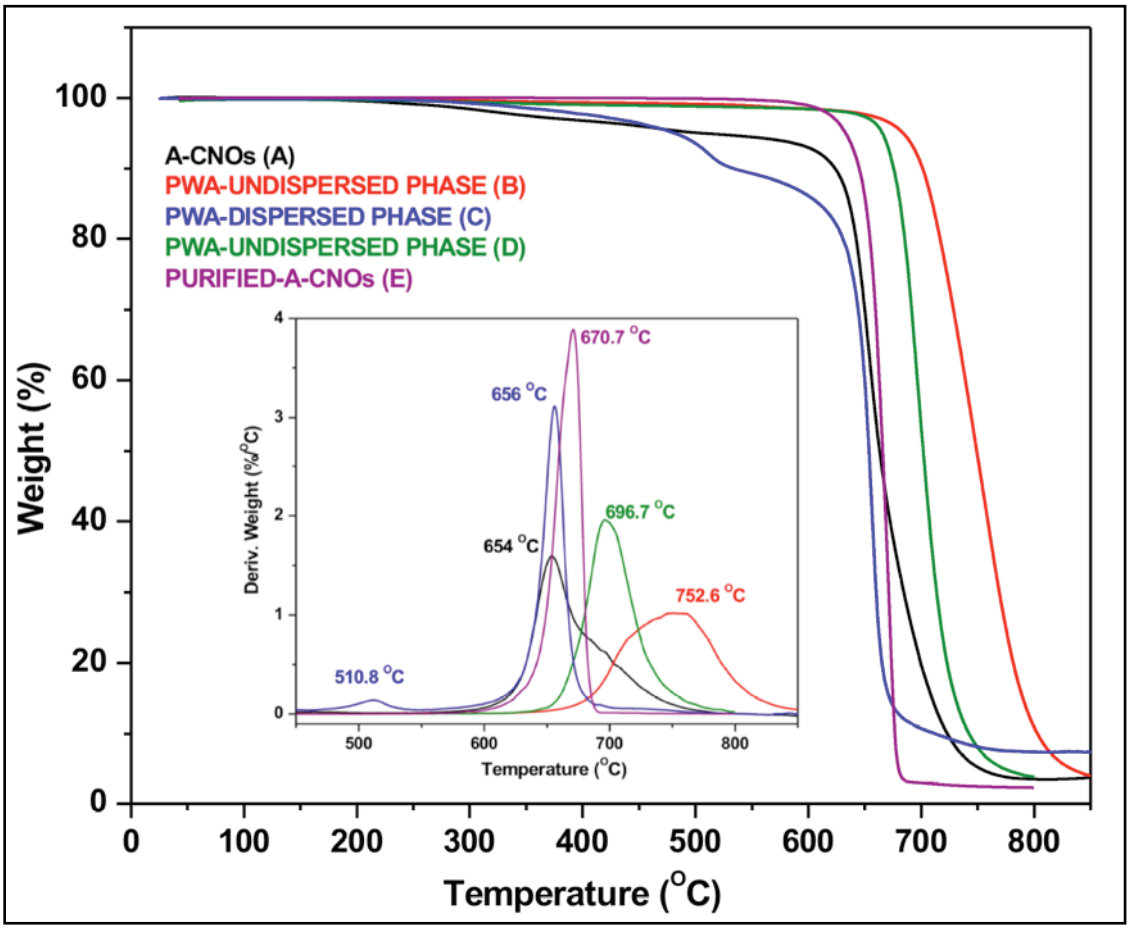

Figure 3.9. TGA compilation of **A-CNO@825 W**, **PWA-dispersed** and **undispersed A-CNOs**

Treatment with 6 M HNO_3, 6 M HCl and H_2SO_4/HNO_3 (3:2) even under reflux only partially removes adsorbed PWA from A-CNOs. However, room temperature stirring of A-CNOs with bound PWAs in 10–15 % v/v HF for 36 h effectively removes

PWAs. Simple filtration through a membrane filter and washing with water separates PWA-free A-CNOs. By using 1.5 mM phosphotungstic acid, 26–30 wt.% pure A-CNOs were recovered.

Fig. 3.10 shows a stepwise depiction of the modified PWA-based purification method.

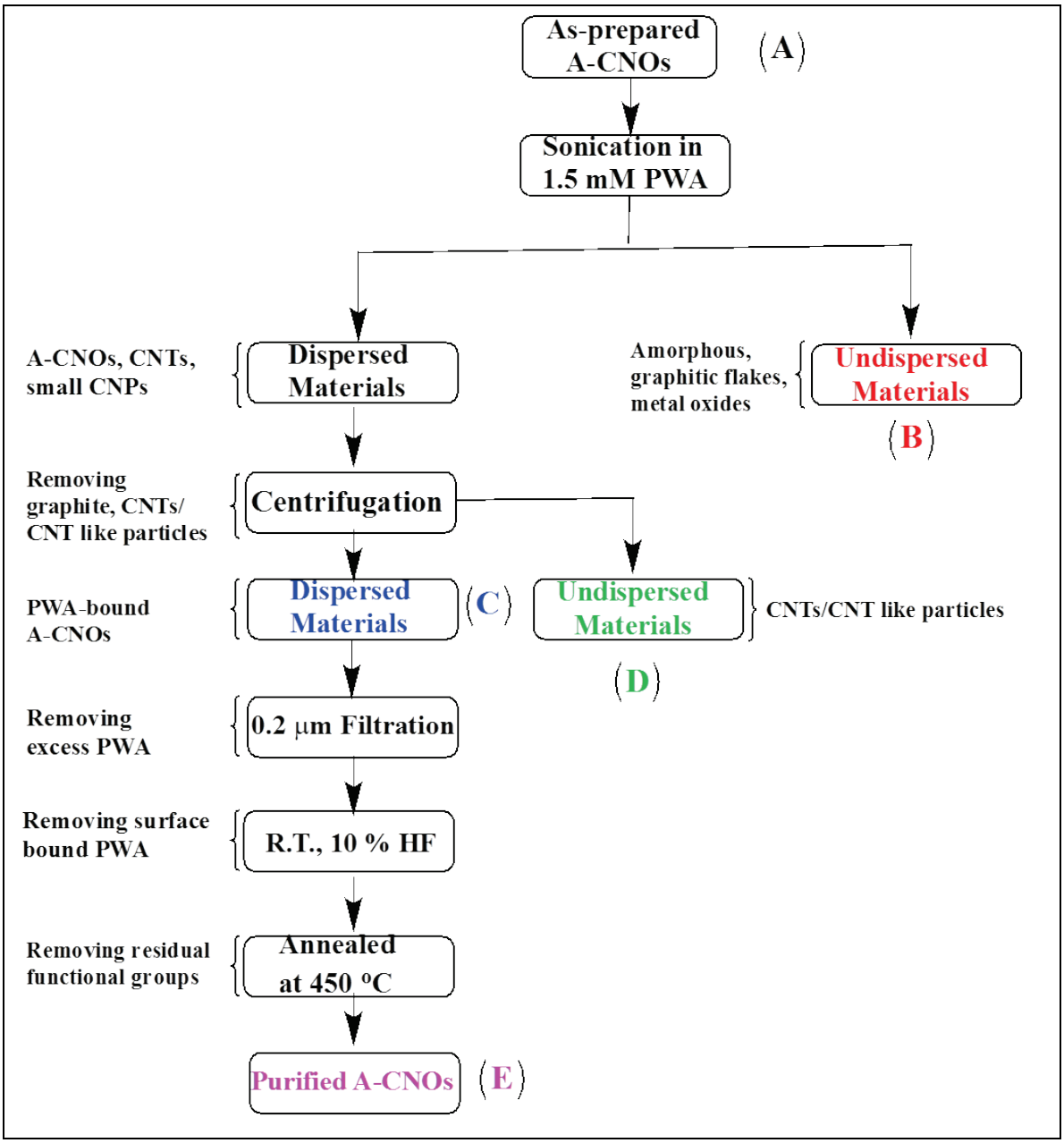

Figure 3.10. Flow chart of PWA purification method for A-CNOs.

The successful purification of A-CNOs by the PWA-based approach was also confirmed by Raman spectroscopic analysis. Dispersed and undispersed phases were collected separately and their Raman spectra were measured for the comparison (**Fig. 3.11**).

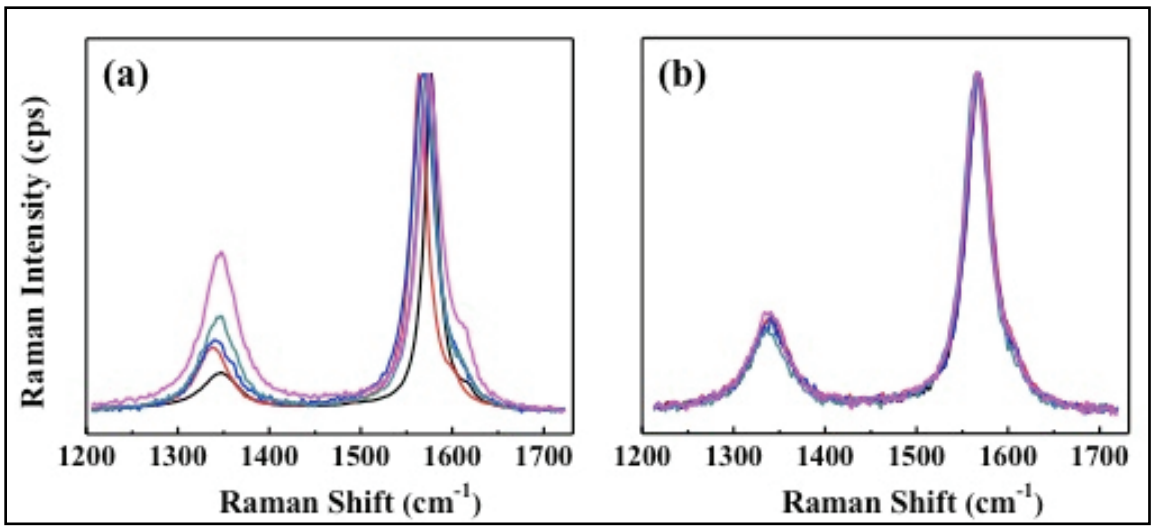

Figure 3.11. Raman spectra of **(a) PWA-Undispersed** and **(b) PWA-Dispersed** materials

They showed noticeably different Raman spectra. The undispersed phase (**Fig. 3.11a**) showed widely varied spectra and dissimilar I_D/I_G (0.1 – 0.5) from spot to spot. This indicates that the undispersed phase contains various carbonaceous phases. In contrast, multi-spot Raman spectra from the dispersed phase are nearly identical (**Fig. 3.11b**). The I_D/I_G of the dispersed phase was close to ~0.25, indicating that A-CNOs were successfully separated from other carbonaceous phases through this purification process.

In addition, the position of G peak is another strong evidence to support the successful purification. Previously, Gupta et al. reported the G peak position center sensitively varies according to the morphology, especially the curvature and strain, of

carbon materials.[63] They reported that the G peak center of CNO has significantly downshifted (~1575 cm^{-1}) as compared with highly ordered pyrolytic graphite (HOPG) (~1581 cm^{-1}) and multiwall carbon nanotube (MWNT) (~1584 cm^{-1}). According to our Raman data for dispersed and undispersed phases presented in **Fig. 3.11**, the G peak of dispersed phase is centered at around 1574 cm^{-1} while those of undispersed phase broadly cover from 1570 – 1585 cm^{-1}. Broad range of G peak centers of undispersed phase reflect the presence of carbonaceous particles including graphite and CNTs. Based upon the Raman spectroscopic characteristics, PWA-based approach seems to effectively purify A-CNO by the removal of carbonaceous impurities such as carbon nanotube and graphite. The selectivity of purification comes from the preferential adsorption of PWA on the curved CNO surface, compared to other carbonaceous impurities.

HRTEM images, **Fig. 3.12 a–c**, of purified A-CNOs sample from dispersed phase shows mostly onions with very clean surfaces. As shown in **Fig. 3.12 d–f**, materials recovered from the undispersed phase contain mostly amorphous and graphitic carbon particles along with CNTs/CNT like particles and a few A-CNOs.

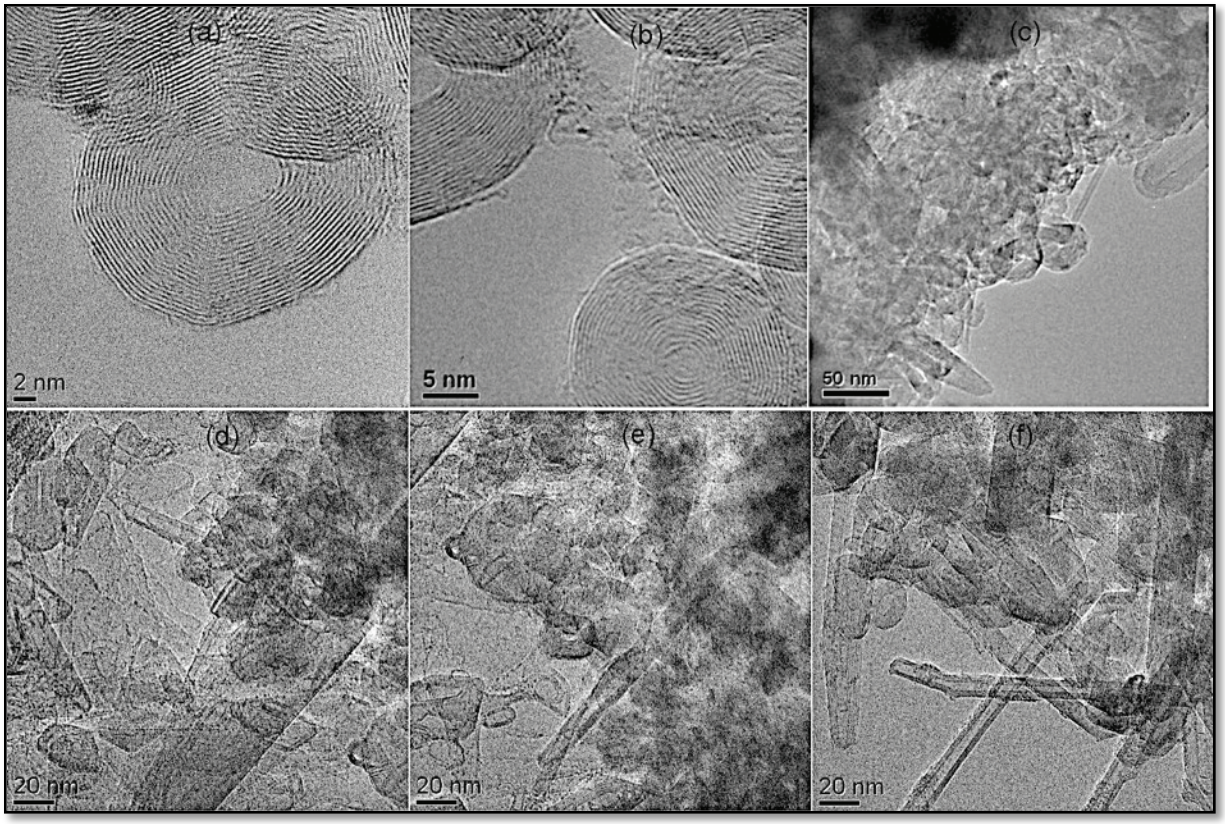

Figure 3.12. HRTEM images of **PWA-dispersed phase (a, b, c)** vs. **PWA-undispersed phase(c, d, f)**

These observations indicate that PWA preferentially adsorbs by electrostatic interaction with highly curved and stained surface of CNOs as compared to CNTs/CNT like structures and other graphitic particles formed during arc discharge. Therefore, these PWA-bound A-CNOs can be separated from the dispersed phase by centrifugation. However, a yield of ~30 wt.% pure A-CNOs and presence of some A-CNOs in the PWA-undispersed part of the materials indicates the possibility of further optimization in the method. Optimization in terms of PWA vs. A-CNOs concentration and duration of sonication can be done for the recovery of the A-CNOs left behind in the undispersed phase.

To compare the combustion stability of purified A-CNOs with a model amorphous carbon (ENSACO 350G) source and anode particles (McMaster-Carr), TGA study was done under air. For amorphous carbon sample and anode particles, TGA onset temperature were observed at ~655 °C and ~775 °C respectively. The combustion temperature for POM purified and graphitized A-CNO samples fell between these limits, as shown in **Fig. 3.13.**

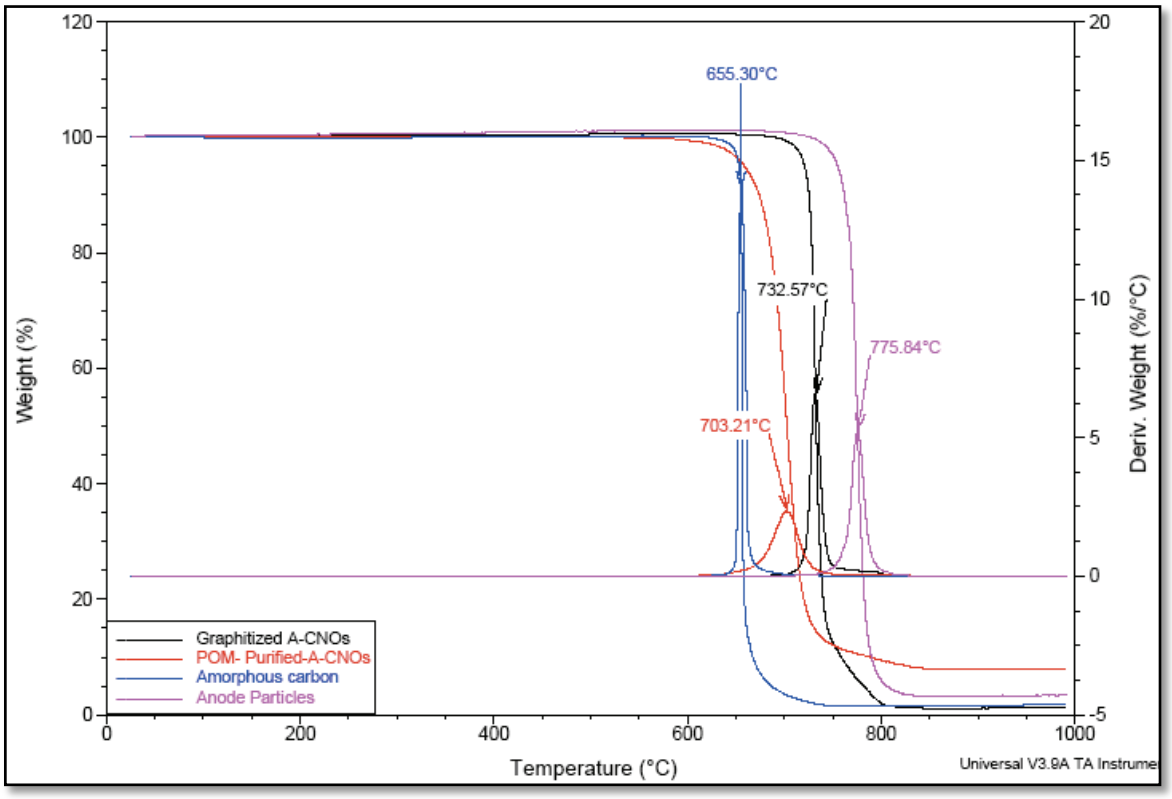

Figure 3.13. TGA overlay of **amorphous**, **graphite (anode particles)**, **purified-A-CNOs**, **graphitized A-CNOs**

TGA comparison reveal that A-CNOs prepared under our experimental conditions have combustion stability in the range of 650–750 °C. Thus, combustion temperature

below 650 °C indicates higher contamination from amorphous carbon materials, while temperature above ~750 °C indicates more graphitic particles in the A-CNO samples.

3.4 Summary

Purification approaches based on physical and chemical properties of A-CNOs have been developed. Physical methods are usually non-destructive and non-oxidative and thus retain surface morphology of the nanoparticles. However, physical methods are not efficient for selective removal of carbonaceous impurities. Although chemical methods introduce surface defects and usually involve multistep treatments, they are more efficient. Mixed-acid treatment along with extraction is also partially effective for the purpose. Combinations of both chemical and physical methods are important to purify A-CNOs. The POM-based purification method is very efficient in removing carbonaceous impurities such as CNTs/CNT like particles, graphite, and amorphous carbons as compared to other methods.

Chapter IV: Functionalization of CNOs

4.1 Introduction

Why is functionalization important?

Functionalization of carbon nanoparticles and their solubilization in aqueous and non-aqueous medium has many applications in various aspects of these nanomaterials. Most importantly, it will allow the study of physicochemical properties of these materials using well-developed solution-based characterization techniques. Knowledge of these materials in solution offers unique opportunities to judge their compatibility in biomedical applications and high-performance nanocomposite materials.

Embedding carbon nanomaterials in polymeric matrices is a popular research area for development of various composite materials. However, use of pristine nanomaterials for fabrication of polymeric carbon nanocomposites results in poor quality of the materials. This is due to the aggregation of nanoparticles and inhomogeneous dispersion in the polymer matrices. This is a particularly serious issue for materials design for optical applications. Studies on polymer-functionalized SWNTs and MWNTs showed that preparation of nanotube-embedded polyvinyl alcohol (PVA) thin films using solution-casting methods result in high optical quality. The absorption spectra of these thin films are similar to that of functionalized SWNTs in solution.[64]

Biocompatibility is a major issue for many proposed bio-applications of carbon nanomaterials. Sadler *et al.* reported immobilization of oligonucleotides, enzymes and proteins on MWNTs. Also Mioskowski *et al.* took the advantage of shape and rigidity of CNTs to induce helical crystallization of proteins.[64] Water-soluble CNTs can be used in

exchange reactions with natural proteins under optimized conditions to reduce damage to the targeted proteins.[65] However, optimization of conditions such as solvation and other physicochemical requirements to handle nanoparticle-protein bio-conjugates is a big challenge. Thus, solubilization of carbon nanoparticles (CNPs) *via* chemical modification offers excellent opportunities not only in the characterization and understanding of their properties but also their utilization in various nanomaterial applications.

The reactivity of CNOs lies between fullerene (C_{60}) and graphite. While C_{60} exhibits chemical reactivity with many functional groups, planar graphite is extremely inert to chemical functionalization. High reactivity of fullerenes is attributable to their high surface curvature. Thus CNOs with fewer number of concentric layers and greater surface curvature are more desirable for higher reactivity.[33] Unlike CNTs and fullerene, chemistry of CNOs has not been developed so far. Although CNOs and SWNTs have different morphology, based on possible surface groups, their preferences for particular reactions are expected to be similar. Thus reactions done successfully on SWNTs are also promising for CNOs. However, open ends and higher defect sites are additional advantages to CNTs as compared to CNOs.

Derivatizations of SWNTs are typically done either by direct sidewall addition or by functionalization at the defect sites. There is strong experimental evidence for nanotube-bound carboxylic groups on acid-treated CNTs and successful solubilization of SWNTs by further addition of polar and nonpolar groups targeting these bound carboxylic acids.[66] Moreover, other non-covalent modifications to solubilize CNTs include polymer wrapping,[67, 68] cationic or anionic surfactant based wrapping,[69, 70] alkali metal reduction,[71] and π-stacking interaction.[72]

Tour *et al.* reported soluble SWNTs through oxidation alone by using a mixture of oleum and nitric acid. Oleum disperses the SWNTs by removing agglomeration, while nitric acid treatment further oxidizes the acid-intercalated SWNTs dispersion.[66] Since they have reported the presence of –COOH, −OH, −C=O etc. on the surface of the oleum-treated SWNTs, further functionalization targeting these groups can also be done. Based on nanotube-bound carboxylic acid groups, further reactions *via* direct acid–base zwitterion interaction, amidation *via in situ*-generated acyl chloride and carbodiimide-activated coupling could be done.[73] Thus we have proposed oleum oxidation of CNOs followed by further functionalization using various reactions to obtain desired solubility.

Pekker *et al.* reported hydrogenation of CNTs *via* Birch reduction in liquid ammonia.[74, 75] From thermogravimetric and electron microscopic data, they proposed the formation of strongly bound hydrogen derivatives on CNTs sidewall. This harsh reduction condition could also be fruitful for CNOs to functionalize with different electrophiles. Other approaches for chemical modifications of CNTs and C_{60} include 1,3-dipolar cycloaddition of *in situ*-generated azomethine ylide[76] and nitrile oxide.[77] In case of azomethine ylide reaction, long alkyl chains could be introduced *via* aldehyde or amino acid to improve solubility of these materials. Similar types of solution chemistry can also be proposed by attaching long side chains to nitrile oxide precursors.

Characterization of functionalized carbon nanoparticles consistently remains an analytical challenge. Even after more than decades of research, there is no direct technique for adequate characterization of chemically modified materials. A wide variety of techniques including thermogravimetric analysis (TGA), electron microscopy, Raman, infrared (IR) and UV/visible spectroscopy, atomic force microscopy (AFM) and X-ray

photoelectron spectroscopy (XPS) have been applied. Only recently, NMR has been used to identify and to determine regiochemistry of nanotube-bound functional groups. All of these available tools have their limitations and thus cannot provide direct evidence unambiguously. Thus judicial combinations of different techniques are always critical to distinguish covalent functionalization from surface defects. Information and limitations of commonly used characterization techniques are compiled in the **Table 4.1**.

Table 4.1. Common characterization techniques for functionalized CNPs

Technique	Information	Limitation
TGA	Functionalization ratio based on mass loss with respect to temperature and atmosphere	No direct evidence of covalent functionalization
Infrared (IR), ATR-IR	Substituent groups	Weak signal-to-noise ratio makes identification ambiguous
UV/Visible	Van Hove singularities indicate extended conjugation or disruption due to functionalization	Not specific. Loss of Van Hove singularities may be due to surface defects or covalent bonding
^{1}H NMR	Substituent	Requires high solubility, broad signals, chemical shift variations based on size and different binding sites
Solid state ^{13}C NMR	Substituent, evidence for sp^3 molecular motions	Require high functionalization, longer signal acquisition time
XPS, ICP	Element identification, functionalization ratio	Not specific and no direct evidence of covalent functionalization

Microscopy (AFM, TEM along with EDX, STM)	Morphology and heavy element identification	Small portion of the sample can be observed, no evidence of covalent functionalization
Raman	Identification of sp^3 bonding	Not specific, quantification is not reliable
Cyclic voltammetry	Electroactive group identification	Not specific, limited to certain groups only

4.2 Experimental Procedures

Materials Sodium**,** lithium, magnesium sulfate and ferrous sulfate were purchased from J.T. Baker., Ethyl bromoacetate, lauroyl chloride, ferrocene, paraformaldehyde, hexadecanol, phosphorus trichloride, iodomethane, triethylamine, N-methylglycine, L-cysteine hydrochloride and methoxypolyethylene glycol were purchased from Aldrich. Oxalyl chloride, 1-bromohexadecane, phosphotungstic acid hydrate and oleum were purchased from Acros. Sodium bicarbonate and potassium carbonate were purchased from Mallinckrodt. Potassium iodide was purchased from Fisher. Sodium nitrate was purchased from Allied Chemicals. 1-Naphthylamine was purchased from Eastman Organic Chemicals. 3,4-dihydroxybenzaldehyde was purchased from Lancaster. 1-Hydroxybenzotriazole hydrate (HOBt) and *N,N,N′ ,N′* -Tetramethyl-*O*-(1*H*-benzotriazol-1-yl)uronium hexafluorophosphate (HBTU) were purchased from ApexBio. All the chemicals were used as obtained, and without further purification, unless otherwise mentioned.

Thermogravimetric analysis (TGA) TGA analyses were done on Thermal Analysis Hi-Res TGA 2950 instrument. In a typical run 3–5 mg of the sample was loaded

in a platinum pan. For all the analyses, a Hi-Res dynamic ramp (50 °C·min^{-1}, res 4.0 °C to 1000 °C) was used under constant airflow (60 mL·min^{-1}).

TGA-MS TGA-MS was carried out using a temperature ramp of 10 °C·min^{-1} to 550 °C in a 100 mL·min^{-1} flow (metered at STP) of argon. Online mass spectra were acquired for specific mass ions present in the gas exiting from the TGA furnace.

^{1}H NMR spectroscopy ^{1}H NMR spectra were recorded on Varian Gemini-400 and Gemini-200 spectrometers at room temperature and were referenced to residual solvent peaks.

High-resolution mass spectrometry High-resolution electron impact (EI) ionization mass spectra were recorded at 25 eV on JEOL JMS-700T MStation and were referenced to perfluorokerosene (PFK).

Zeta potential measurements Zeta potential experiments were conducted on a zeta potential analyzer (ZetaPlus, Brookhaven instrument, USA). For all measurements, disposable cells were used to avoid contamination.

Cyclic voltammetry measurements Cyclic voltammetry measurements were made using 1 M H_2SO_4 as the electrolyte and screen-printed electrodes from Pine Instruments. The reference and counter electrodes were Ag/AgCl and carbon respectively. Conductive carbon adhesive tape was used to attach the nano-onions to the carbon working electrode (2 mm in dia.).

ICP analysis ICP analysis was done on VISTA-PRO CCD simultaneous ICP-OES analyzer using yttrium (0.1 ppm) as an internal standard. Analysis conditions were

set at Power 1.20 kW, PlasFlow 15.0 L/min, AuxFlow 1.50 L/min, NebFlow 0.90 L/min, Replicate Time 5.000 s and Stab Time 15 s.

A known amount (0.035 g) of CNO sample was taken in an acid digestion tube, followed by addition of 5 mL concentrated HNO_3 (69 - 70%, OmniTrace, EMD Chemicals). Temperature of the digestion unit was raised to 110 °C and the material was predigested for 15 min in HNO_3. Then 5 mL of concentrated HCl (34-37%, OmniTrace, EMD Chemicals) was added to the tube and the material was kept for digestion for another 0.5 h. 10 mL of 50% V/V H_2O_2 (30%, from Fisher) in deionized water was slowly added to the tube and the material was magnetically stirred. The temperature was maintained at 110 °C and digestion was continued for 48 h with intermittent volume make-up using deionized water. After the digestion, the mixture was carefully filtered through a 0.2-μm membrane filter and washed with small amount of deionized water. The exact volume of the filtrate was recorded. The same procedure was followed to prepare a digested sample of the starting material (CNO-COOH) along with a blank and two known concentrations (10.00 and 20.00 ppm) without CNO sample. Five standard solutions of concentrations 0.5, 1.00, 5.00, 10.00 and 50.00 ppm and two spiked solutions with known volume of CNO-CO$NC_3H_6O_2S$ and CNO-COOH digested samples were prepared by adding calculated volume of 1000 ppm sulfur standard (Fisher Chemicals) in deionized water.

4.3 Functionalization via Billups reductive alkylation

In a typical procedure, approx. 50–60 mL of ammonia was condensed in a three-necked round-bottom flask under N_2. CNOs (0.200 g) of were added to it and stirred for 10–15 min for better dispersion. An excess amount of lithium was added to the above

mixture, which instantly turned liquid ammonia into a deep blue solution and stirring was continued for another 30 min at -78 °C. The electrophile in the weight ratio of 1:4 to that of CNOs was added slowly, using a syringe. The reaction mixture was stirred for another 15 min at -78 °C and then warmed to room temperature. After room temperature was attained and the liquid ammonia was evaporated, the reaction was quenched with water (30 mL). The product was repeatedly washed with water followed by acetone and dichloromethane and then vacuum-dried overnight at 45 °C. This procedure was followed for the following electrophiles:

- (iodomethane, MeI) [A]
- (ethyl bromoacetate, $BrCH_2COOEt$) [B]
- (lauroyl chloride, $C_{11}H_{23}COCl$) [C]
- (t-butyl bromoacetate, $BrCH_2COOCMe_3$) [D]
- Ferrocene derivative (chloromethylferrocene)

Step I Synthesis of hydroxymethylferrocene. To a mixture of ferrocene (0.93 g, 5.0 mmol) and paraformaldehyde (0.75 g, 25 mmol) at 0 °C, H_2SO_4 (95%, 3.7 mL) was added dropwise with constant stirring for 30 min. The mixture became deep red in color. Distilled water (100 mL) was added slowly to the reaction mixture, followed by addition of $NaHCO_3$ (17.5 g). A small amount of sodium dithionate was added to the mixture until the color became orange-yellow. The product was extracted with ethyl ether and dried over $MgSO_4$. Ethyl ether was removed *in vacuo* and the product was recrystallized from

hexane. Yield: 76%. Mp: 79-80 °C ^{1}H NMR (400 MHz, $CDCl_3$-*d*, ppm): δ 4.158 (t, 2H, ^{3}J = 1.6 Hz, Cp), 4.164 (s, 5 H, Cp), 4.224 (t, 2H, ^{3}J = 1.6 Hz, Cp), 4.311 (s, 2H, HOCH_2).

Step II Synthesis of chloromethylferrocene. Hydroxymethylferrocene (0.50 g, 1.0 mmol) was dissolved in dry THF (20 mL) under N_2, followed by slow addition of pyridine (0.18 mL, 1.0 mmol). In another flask, a solution of PCl_3 (0.15 mL, 0.50 mmol) in dry THF (15 mL) was prepared. This solution was added dropwise to the hydroxymethylferrocene reaction mixture and continued stirring for another 4 h at room temperature under N_2. The product (yellow precipitate) formed was cannula-filtered to another flask and washed with fresh THF (3 × 10 mL). The filtrate was evaporated under vacuum. The orange-yellow product was stored under N_2.

Step III Synthesis of ferrocenylmethyl-derivative of A-CNOs [E]. Birch reduction of CNOs was carried out as described above using freshly prepared chloromethylferrocene as electrophile. The product was repeatedly washed with water followed by dichloromethane and ethyl ether until the yellow color of the filtrate disappeared. The material was rewashed with dichloromethane in a Soxhlet extractor for 24 h and then vacuum-dried overnight at 45 °C.

4.4 Functionalization *via in situ* cycloaddition reaction

Synthesis of pyrrolidine derivative of N-CNO *via* 1,3 cycloaddition

4.4.1. ($OC_{41}H_{75}NO_2$) –N-CNO [F]

Step I Synthesis of 3,4-bis(hexadecyloxyl)benzaldehyde. To a stirred solution of 3,4-dihydroxybenzaldehyde (4.10 mmol, 0.565 g) in 60 mL dry DMF under N_2, 16.8 mmol (5.00 mL) of 1-bromohexadecane was added, followed by potassium carbonate

(8.18 mmol, 0.805 g) and potassium iodide (0.076 g). Temperature of the reaction mixture was maintained at 70-72 ºC in a silicone oil bath for 20 h. A dirty white product was obtained. Water was added to the reaction mixture and the product was extracted with chloroform. The upper aqueous layer was discarded and the lower layer containing a mixture of $CHCl_3$ and DMF was dried *in vacuo*. The residual white solid was recrystallized from chloroform and methanol and dried under vacuum overnight at 45 °C. A bright silver, shiny solid was obtained. Mp: 78-79 ºC; yield: 33.9%; ^{1}H NMR (400 MHz, $CDCl_3$-*d*, ppm): δ 0. 886 (t, 6H, ^{3}J = 6.4, Hz, CH_3), 1.307 (s, 48H, CH_2), 1.830 (m, 4H, ^{2}J = 6.8 Hz, CH_2), 4.040 (t, 2H, ^{3}J = 4.8 Hz, OCH_2), 4.069 (t, 2H, ^{3}J = 6.4 Hz, OCH_2), 6.931 (d, H, Ar-H); 7.400 (d, 2H, Ar-H); 9.820 (s, H, -CHO); ATR-IR (cm^{-1}): 2916, 2844 (s, sp^3 C-H), 1684 (s, C=O), 1273 (s, C-O-C); MS (EI): m/z 586 (M^+), 362 (M^+-$C_{16}H_{32}$), 138 (M^+- ($C_{16}H_{32}$)$_2$).

Step II *In situ* synthesis of pyrrolidine derivative of CNOs. To a 1:1 mole ratio of 3,4-bis(hexadecyloxyl)benzaldehyde (0.327 g, 0.560 mmol) and N-methylglycine (0.050 g, 0.560 mmol) in dry toluene under N_2, N-CNOs (0.050 g) were added. The suspension was refluxed for 5 days. It was then brought to room temperature and the solvent was decanted by centrifuging. Fresh toluene was added to the functionalized N-CNOs and bath-sonicated for 10 min to remove the adsorbed organics. The dispersion was centrifuged, solvent was decanted and the material was vacuum-dried. The material was rewashed in a Soxhlet extractor with dichloromethane for 36 h to ensure complete removal of adsorbed byproducts and dried under vacuum overnight at 45 °C.

4.4.2. $(CH_3)_3COONCH_2$–N-CNO [G]

To air-cleaned NCNOs (0.100 g), 2-(*tert*-butoxycabonylamino)acetic acid (0.500 g, 0.0028 moles) and paraformaldehyde (0.495 g, 0.0168 moles) were added and homogeneously mixed by stirring in absolute ethanol (5–7 mL) at room temperature overnight. The ethanol was evaporated, the reaction mixture was put in a round-bottom flask under N_2 and the temperature of the silicone bath was maintained at 200 ºC for 12 h. The product was cooled to room temperature and washed with acetone (50 mL) followed by continuous Soxhlet extraction in ethanol for 24 h. Finally the product was vacuum-dried at 70 ºC overnight.

4.5. Functionalization via Sandmeyer reaction [H]

To a stirred solution of 1-naphthylamine (2.0 g, 12 mmol) in aqueous acetic acid (20 mL in 10 mL H_2O) at 0 °C, a well-dispersed (15 min bath sonication) suspension of CNOs (0.15 g) in acetic acid (20 mL) was added. After 30 min of continuous stirring at 0 °C, an aqueous solution of sodium nitrate (1.0 g in 10 mL H_2O) and ferrous sulfate (4.0 g) was added to the reaction mixture and stirred continuously for another 8 h. The material was filtered through a 2 μm membrane filter, washed with water (3 × 100 mL), acetone (100 mL) and dichloromethane (100 mL), and dried *in vacuo*. The modified CNOs were again treated with refluxing oleum for 3 h. The final dispersion was centrifuged, decanted and the precipitate was washed with water (3 × 100 mL) and vacuum-dried at 45 °C overnight.

4.6. Functionalization via oleum oxidation

A sample of A-CNOs (0.25 g) was dispersed in oleum (35 mL, 18-23% SO_3) in a 250 mL sidearm round-bottom flask. The dispersion was magnetically stirred for 36 h at room temperature under N_2. A mixture of oleum (15 mL) and HNO_3 (70%, 22 mL) was slowly added to the CNO-oleum dispersion with continued stirring. During this addition, an ice bath was used to maintain the temperature close to room temperature. After about 10 min, the ice bath was removed and the resultant mixture was warmed to 80–82 ºC in a water bath and stirred continuously for 2 h. The dispersion was carefully poured into a beaker containing distilled water (300 mL) while being cooled by using an ice bath. The slurry was centrifuged for 0.5 h and the dark brown solvent was decanted. CNOs settled in the centrifuge tube were bath-sonicated in acetone for 10-15 min and again centrifuged and decanted. This process was continued until a clear solvent of neutral pH was obtained. Due to the small size and high dispersibility of the material, it takes several hours to filter the solvent through a 0.2 μm membrane filter. Moreover, the filtrate contains a large portion of dissolved CNOs in highly acidic condition. Thus, the centrifuge method was found to be more efficient to recover the maximum amount of material. The product, **A-CNO-COOH [I],** was transferred to a Petri dish and vacuum-dried overnight at 45 ºC.

A similar procedure was followed for N-CNOs, although room temperature stirring in oleum was reduced to 24 h and the high temperature (80–82 ºC) stirring in oleum/HNO_3 was also reduced to 1 h to synthesis **N-CNO-COOH [J].**

Further functionalizations

Chlorination of oleum-oxidized A-CNOs [I]/N-CNOs [J]. A sample of oleum-oxidized CNOs (0.050 g) was taken in a two-necked round-bottom flask under N_2. Oxalyl chloride (3 mL) was dispensed into the flask and the mixture was bath-sonicated for 1 h for better dispersion of the CNOs. After removing from bath sonication, a drop of DMF was added to the mixture and continuously stirred for 1 h at room temperature. The material became sticky after the reaction and the excess oxalyl chloride was evaporated *in vacuo*.

4.6.1. Nucleophilic addition of methoxypolyethylene glycol (Mw ~5000) [K]

In a 250-mL round-bottom flask, a calculated (1:4 weight ratio of A-CNO: PEG) amount of methoxypolyethylene glycol was added in approximately 15 mL of anhydrous DMF under N_2 and the mixture was warmed to 60 ºC to give a clear solution. A calculated amount (1:1 mole ratio) of Na metal was added to the solution and the mixture was continuously stirred until the Na dissolved completely. The light yellow solution was cannula transferred to a freshly prepared sample of A-CNO-COCl in another flask under N_2. The resultant mixture was stirred at 80 ºC for 6–7 h. After the reaction, the mixture was brought back to room temperature and the black solid was separated by centrifugation. The resulting black powder was washed with fresh DMF (2 × 40 mL), dichloromethane (2 × 40 mL) and vacuum-dried overnight at 45 ºC.

4.6.2. Nucleophilic addition of cysteine followed by coupling of ferrocene methyl amine

Step I Nucleophilic addition of cysteine [L]. To freshly prepared A-CNO-COCl (~0.110 g) under N_2, dry THF (15 mL) was added, bath-sonicated for 15 min and to this well-dispersed mixture L-cysteine hydrochloride (0.444 g, 3.00 mmol) was added,

followed by slow addition of triethylamine (1.00 mL, 9.90 mmol). The reaction mixture was stirred for 12 h at room temperature under N_2. The product was washed with fresh THF followed by CH_2Cl_2. The material was rewashed with ethanol in a Soxhlet extractor for 48 h to ensure complete removal of adsorbed byproducts and dried under vacuum at overnight 45 °C.

Step II Synthesis of ferrocenylmethylammonium chloride. The synthesis was carried out according to the reported procedure.[78] The yellow product was recrystallized from MeOH with a yield of ~51%.

Step III Amidation via coupling reaction [M]. Cysteine-functionalized CNOs (from Step A, 0.05 g) were dispersed in DMF (10 mL) in a bath sonicator for 30 min. To the dispersion, HOBt (0.027 g in 10 mL DMF, 0.02 M) followed by HBTU (0.076 g in 10 mL DMF, 0.020 M) were added and stirred for 10 min under N_2 at room temperature. DIPEA (0.16 M) was added to the reaction mixture, stirred for another 10 min, and finally ferrocenylmethylammonium chloride (0.05 g in 10 mL DMF, 0.02 M) was introduced and the whole reaction mixture was stirred under N_2 overnight at room temperature. The reaction mixture was centrifuged and the yellow solution was decanted. The product was washed (3 × 50 mL DMF, 2 × 50 mL MeOH) and vacuum-dried overnight at 70 ºC.

4.7 Results and Discussion

4.7.1. Reductive alkylation of CNOs

Various electrophiles have been used to functionalize A-CNOs *via* Billups reductive alkylation. Initially, short chain and very reactive electrophiles such as iodomethane and ethyl bromoacetate were used to study the physical and thermal changes

of A-CNOs. Later, long-chain polar groups were attached to improve the solubility/dispersibility of functionalized A-CNOs. Moreover, to study the interaction of A-CNOs and functional groups, the electroactive ferrocene group was used and the product was characterized by cyclic voltammetry.

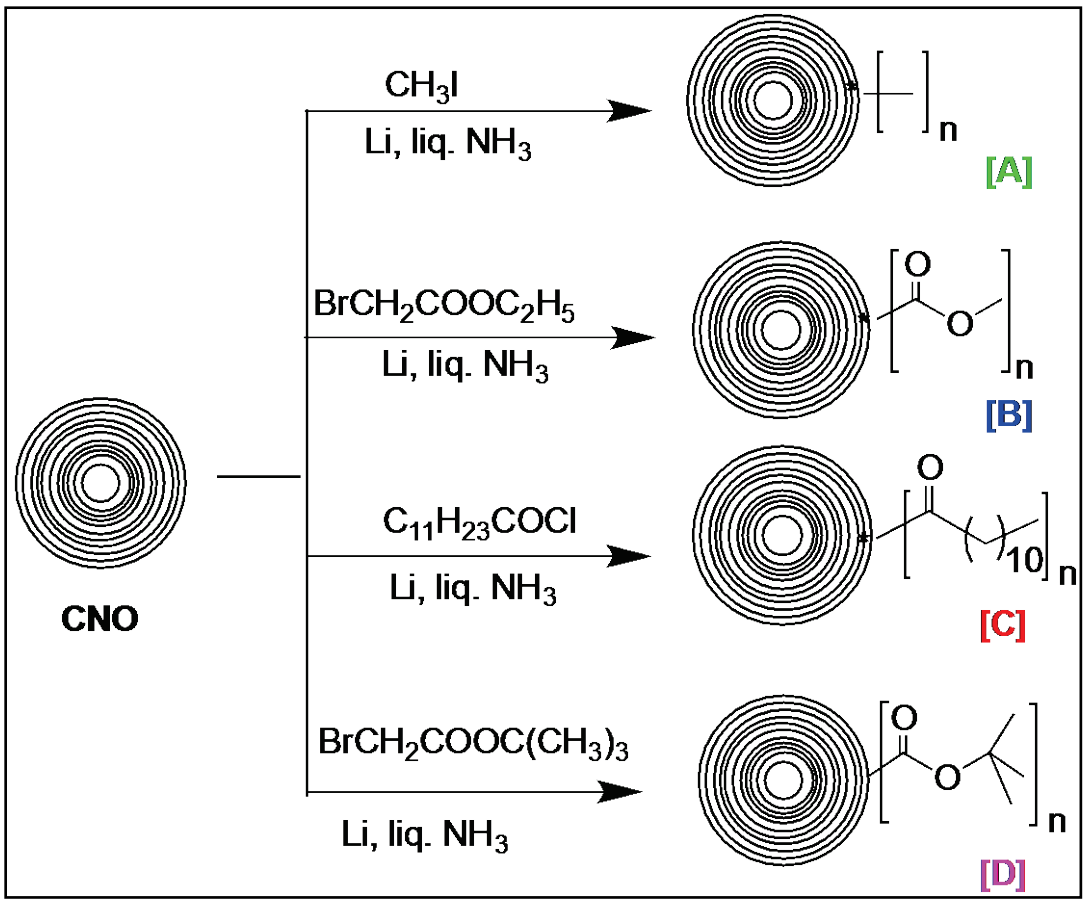

Scheme 4.1. Reductive alkylation approaches to attach hydrocarbon chains to A-CNOs.

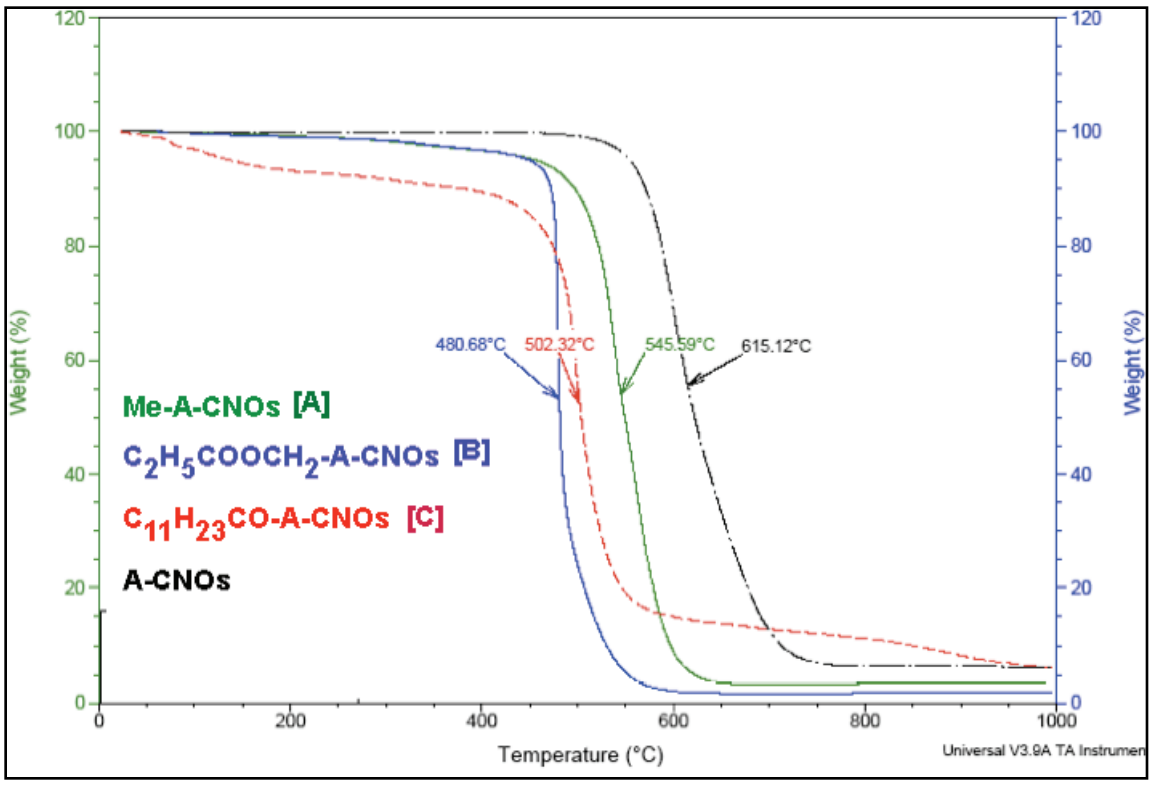

Figure 4.1. TGA (under air) compilation of **Me-A-CNOs, [A]; $C_2H_5COOCH_2$-A-CNOs, [B]; $C_{11}H_{23}CO$-A-CNOs, [C];** and **A-CNOs.**

A comparison of onset combustion temperatures of A-CNOs and Billups-functionalized A-CNOs is shown in **Fig. 4.1**. The large changes in onset temperature of these functionalized materials indicate the change of surface morphology of as-produced A-CNOs, probably *via* reduction of double bonds and forming C-C bond between the electrophile and CNO carbon network.

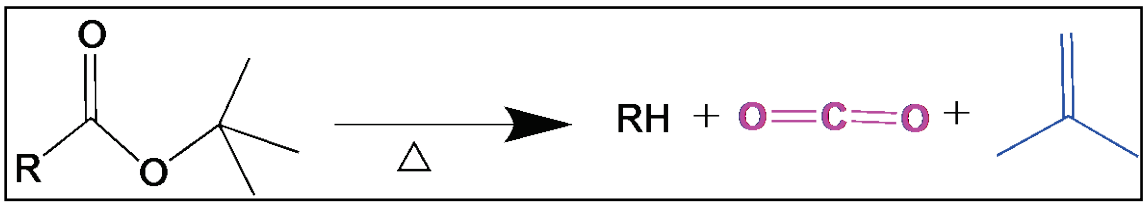

Scheme 4.2. Thermal decomposition of *t*-butyl ester at elevated temperature.

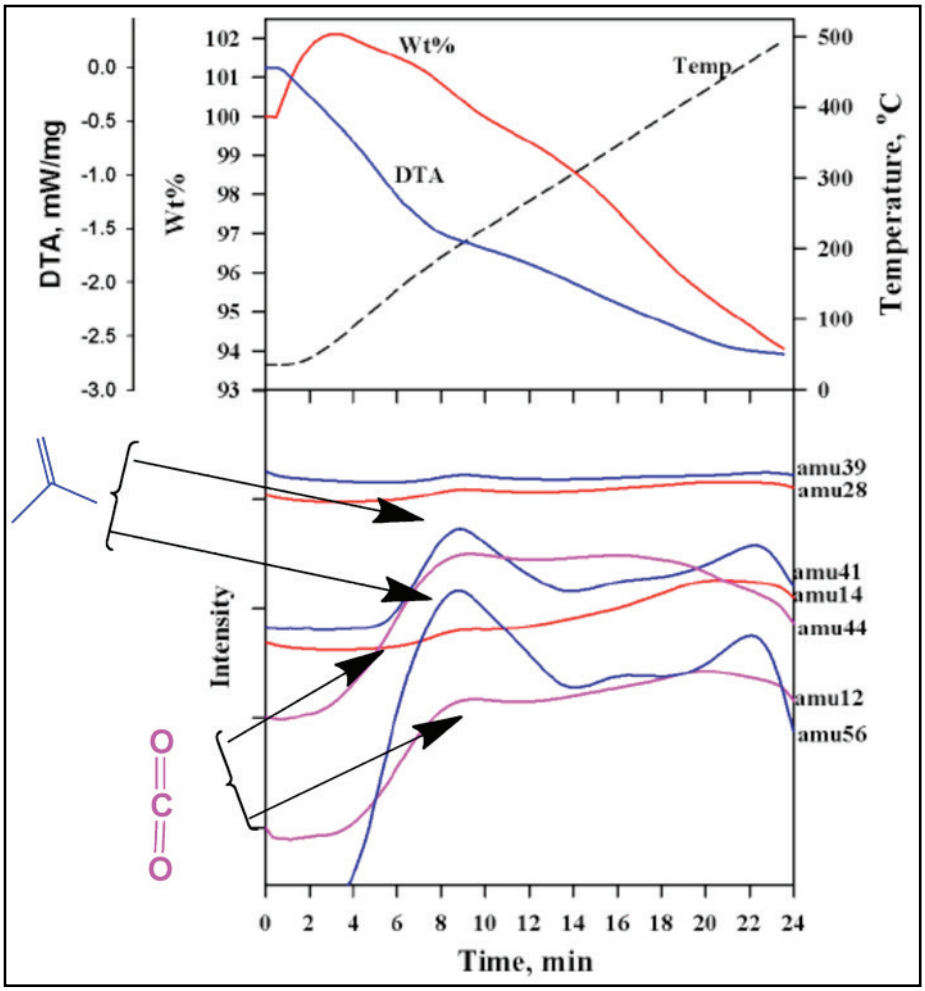

Figure 4.2. TGA-MS of **$(CH_3)_3CCOOCH_2$-A-CNOs, [D].**

Fig. 4.2 shows TGA-MS analysis of $(CH_3)_3CCOOCH_2$–A-CNOs, [D], monitoring ions at 12 (C^+), 14 (N^+), 28 (N_2^+, CO^+), 39 ($C_3H_3^+$), 41 ($C_3H_5^+$), 56 ($C_4H_8^+$), 44 (CO_2^+, N_2O^+), amu. Evolved NO and NO_2 yield N^+, NO^+ and NO_2^+. Evolved CO and CO_2 yield C^+, CO^+ and CO_2^+, but N_2^+ interferes with CO^+ and N_2O^+ interferes with CO_2^+.

The major mass ions for isobutene are, in decreasing abundance, 41, 39 and 56 amu. The prominent parallel curves for 41 and 56 amu ions at ~8 min. corresponding to a mass loss ~400 ºC in the TGA-MS indicates the presence of isobutene in the product gas mixture. Similar parallel curves (12 and 44 amu) are observed for the evolution of CO_2.

These observations also support the presence of *t*-butyl ester groups on the surface of the functionalized CNOs obtained via Billups reductive alkylation.

The electroactive ferrocene group was used to functionalize CNOs *via* Billups reductive alkylation. The advantage of this group is that electrochemical studies could be done to quantify attached functional groups. Controlled coulometry study and precise measurement of exact mass of the functionalized material should give a close estimate of the surface coverage on the nano-onions. Chloromethylferrocene was attached to A-CNOs *via* Billups reductive alkylation (**Scheme 4.3**). A TGA study indicated typical surface change of A-CNOs with lower onset temperature after the chemical modification (**Fig. 4.3**).

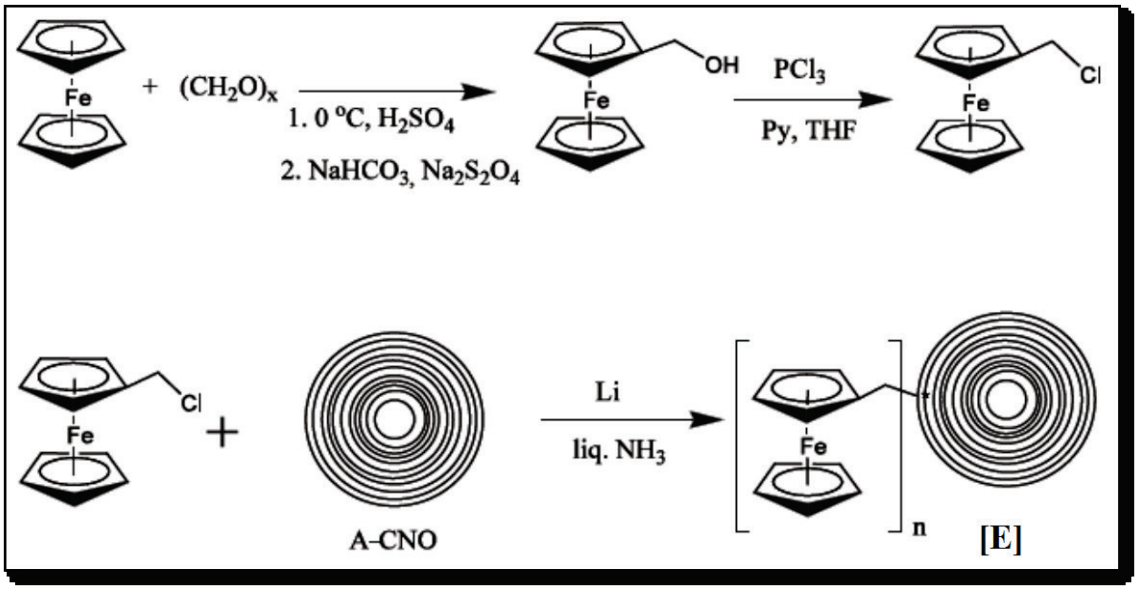

Scheme 4.3. Reductive alkylation approach to attach electroactive ferrocenyl groups on A-CNOs.

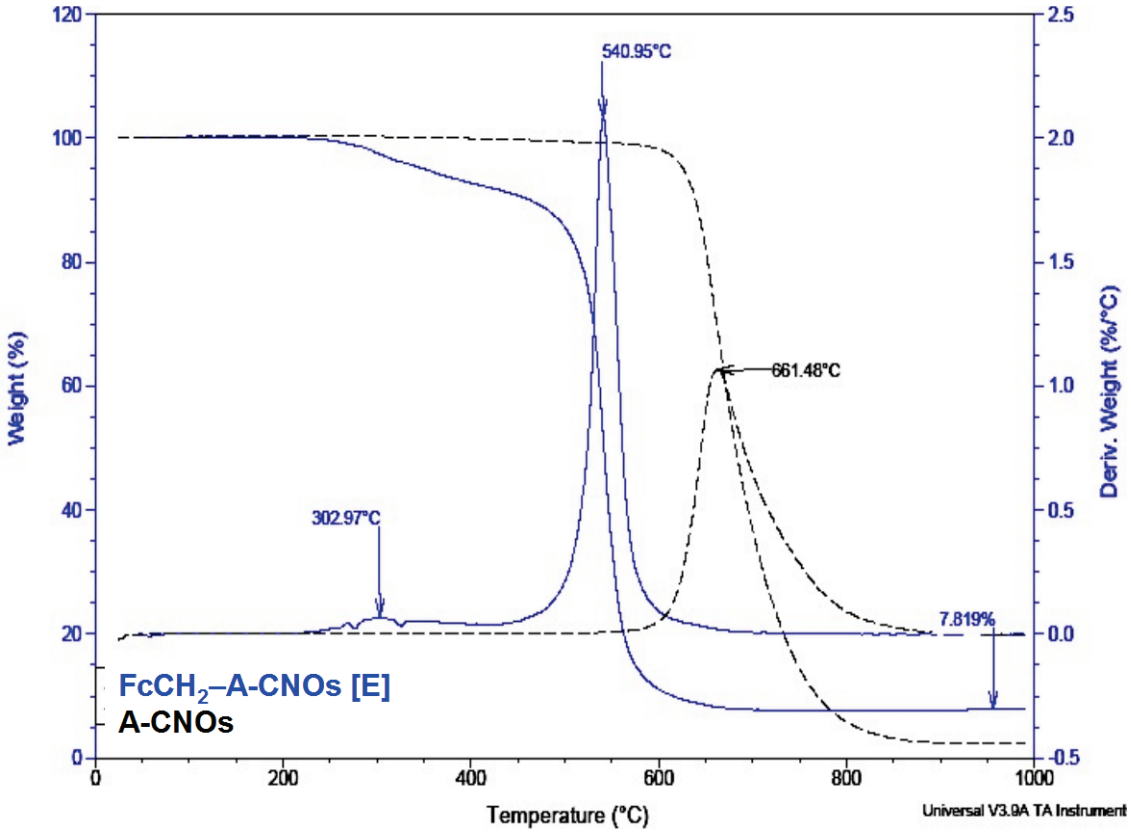

Figure 4.3. TGA compilation of **ferrocenylmethyl-derivatized A-CNOs [E]** and **A-CNOs.**

Cyclic voltammetry measurements were made using 1.0 M H_2SO_4 as the electrolyte. The CV was run for the carbon current collector by itself, the carbon current collector and carbon adhesive tape together, and finally the carbon current collector, carbon adhesive tape and carbon nano-onions together. The current collector and adhesive tape are found to be electrochemically "inert"; thus 1.0 M H_2SO_4 is an acceptable electrolyte for this study.

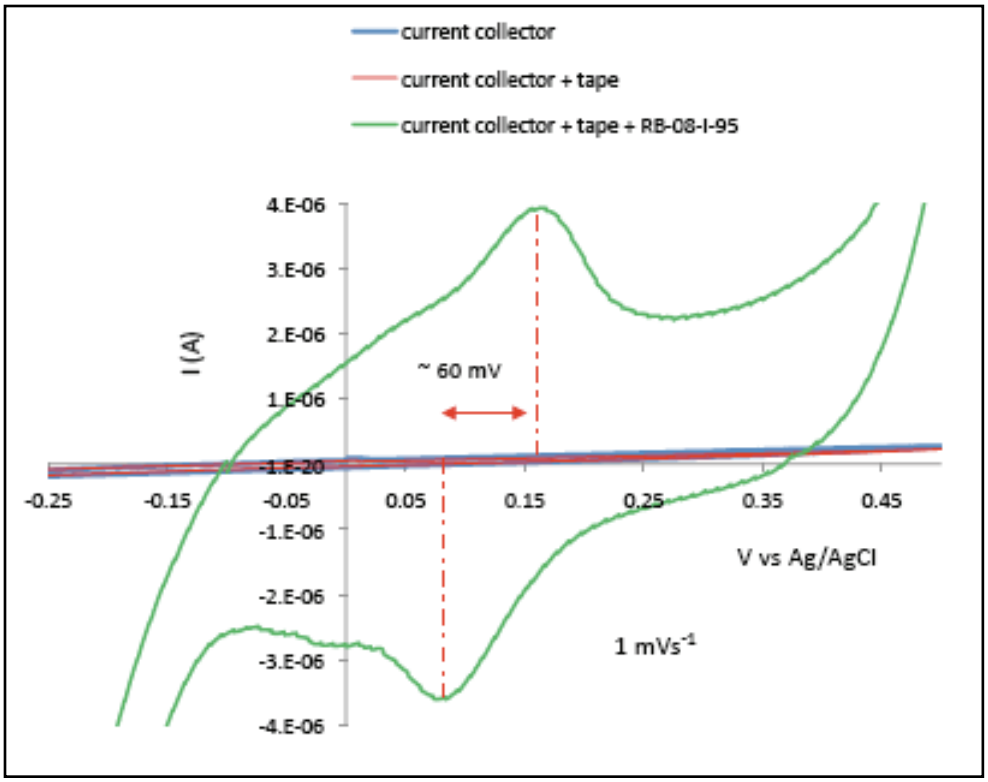

Figure 4.4. Cyclic voltammogram of **Fc–CH_2- A-CNOs [E]**

The ferrocenylmethyl-functionalized CNO sample [E] has coupled oxidation and reduction waves (peak separation ~60 mV) at a sweep rate of 1 mV/s. Thus the redox reaction appears to be reversible. The columbic efficiencies for the oxidation and reduction waves were also found to be very similar (**Fig. 4.4).** The CV data suggests successful functionalization of A-CNOs *via* Billups reductive alkylation. According to Faraday's principle, the amount of current is directly related to the number of electrons undergoing redox reaction; thus, the low current intensity of the material indicates a small number of functional groups on the surface. However, by measuring the active mass of the material, a controlled coulometric experiment can be done to count the number of electroactive functional groups present on the CNO surface. However, the experiment was not performed due to unavailability of the required facility.

4.7.2. *In situ* cycloaddition of N-CNOs (Prato reaction)

1,3-Cycloaddition of azomethine ylides is a well-studied *in situ* functionalization method for fullerenes (C_{60})[79] and CNTs,[80]. Azomethine ylides are highly reactive 1,3-dipoles generated *in situ* by dehydration and subsequent thermal decarboxylation. Recently, there are growing interests in the functionalization of CNOs using similar ylide chemistry. Prato *et al* reported a pyrrolidine derivative of CNOs using long-chain amino acids and paraformaldehyde.[81] Azomethine ylide-functionalized CNOs could be more useful in term of solubility/dispersibility if long alkyl chains are introduced *via* aldehyde or amino acid precursors. Thus, 3,4-bis(hexadecyloxyl)benzaldehyde, synthesized from 3,4-dihydroxybenzaldehyde, was used as precursor along with N-methylglycine (sarcosine) for *in situ* cycloaddition of a azomethine ylide to CNOs (**Scheme 4.4**). The functionalized material is readily dispersed in semi-polar solvents ($CHCl_3$). Zeta potential measurements done in absolute ethanol showed ζ = + 22.32, thereby indicating the expected medium dispersibility in polar solvents due to the presence of long alkyl chains. TGA under air showed 13% mass loss due to surface groups, which starts at around 330 °C and ends at around 470 °C (**Fig. 4.5**). The mass loss at higher temperature (> 300 °C) signifies very strong interactions between CNOs and the functional groups, rather than simple adsorption.[82] Simply adsorbed organics typically undergo desorption at about 200–300 °C. To ensure that the electrophiles are not simply adsorbed on the surface of CNOs, TGA was done with functionalized material under inert gas (Ar). No mass loss was observed near the onset combustion temperature of the material, as shown in **Fig. 4.5**. Therefore, chemical changes at the surface reactive sites of CNOs, either by

functionalization of desired electrophile or by groups that have been generated through decomposition of the added electrophile during the reaction condition, are supported.

(X)

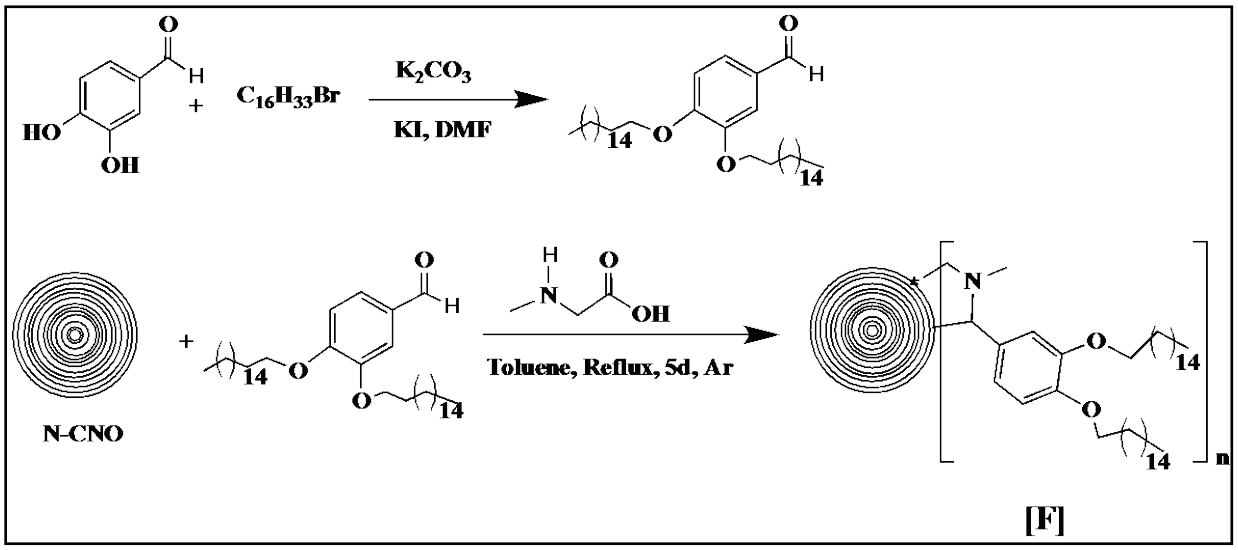

(Y)

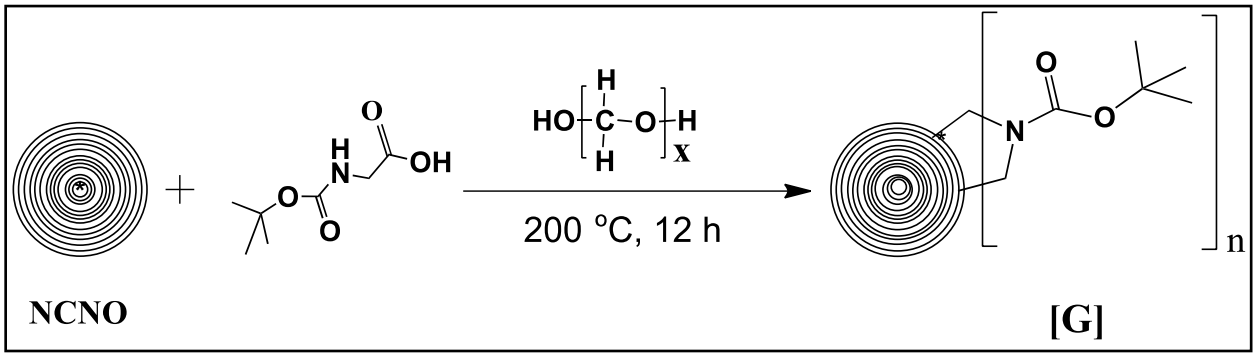

Scheme 4.4. (X), (Y) Stepwise synthetic route to pyrrolidine derivative of CNOs.

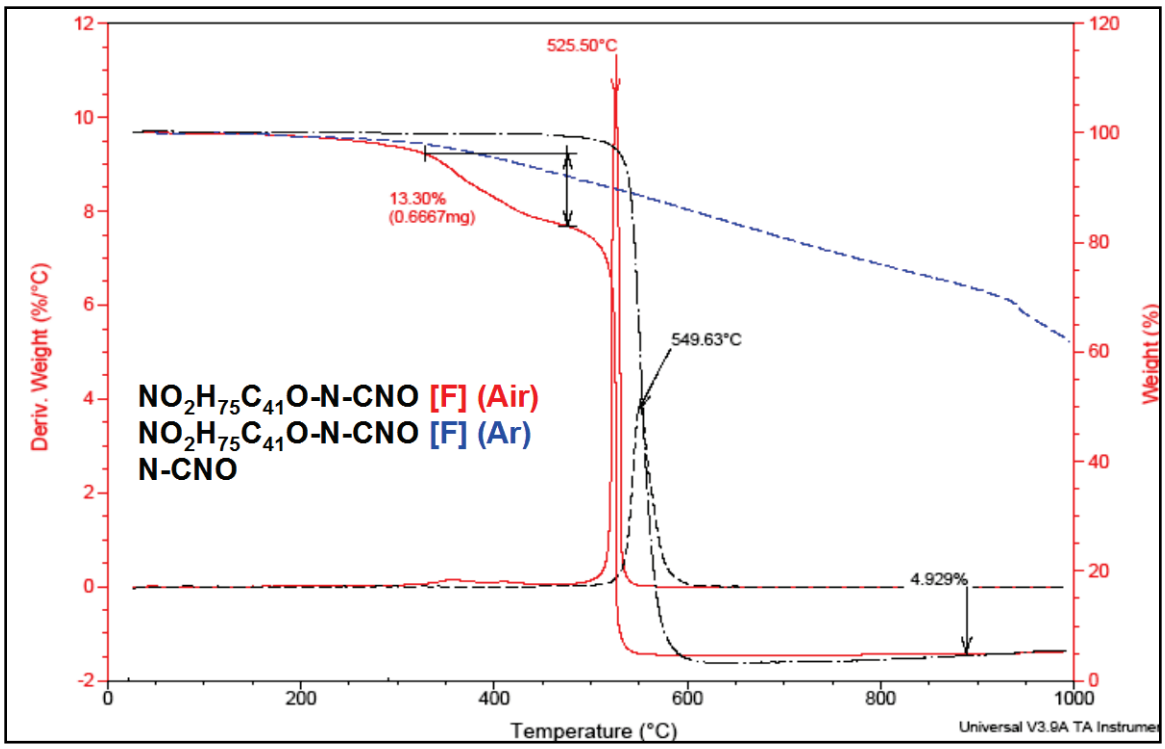

Figure 4.5. TGA overlay of **pyrrolidine-functionalized N-CNOs [F] under air** and **argon.**

^{1}H NMR in $CHCl_3$ showed broad resonances, making identification ambiguous. In **Scheme 4.4.B,** *t*-butyl groups are added to the surface of CNOs so that the presence of desired functional groups can be identified via TGA-mass spectrometry, as described in the earlier characterization of Billups reductive alkylation products. **Fig. 4.6** shows the presence of isobutene (44 and 56 amu), thus indicating the presence of the t-butyl functional groups on the pyrrolidine-functionalized N-CNOs **[G]**.

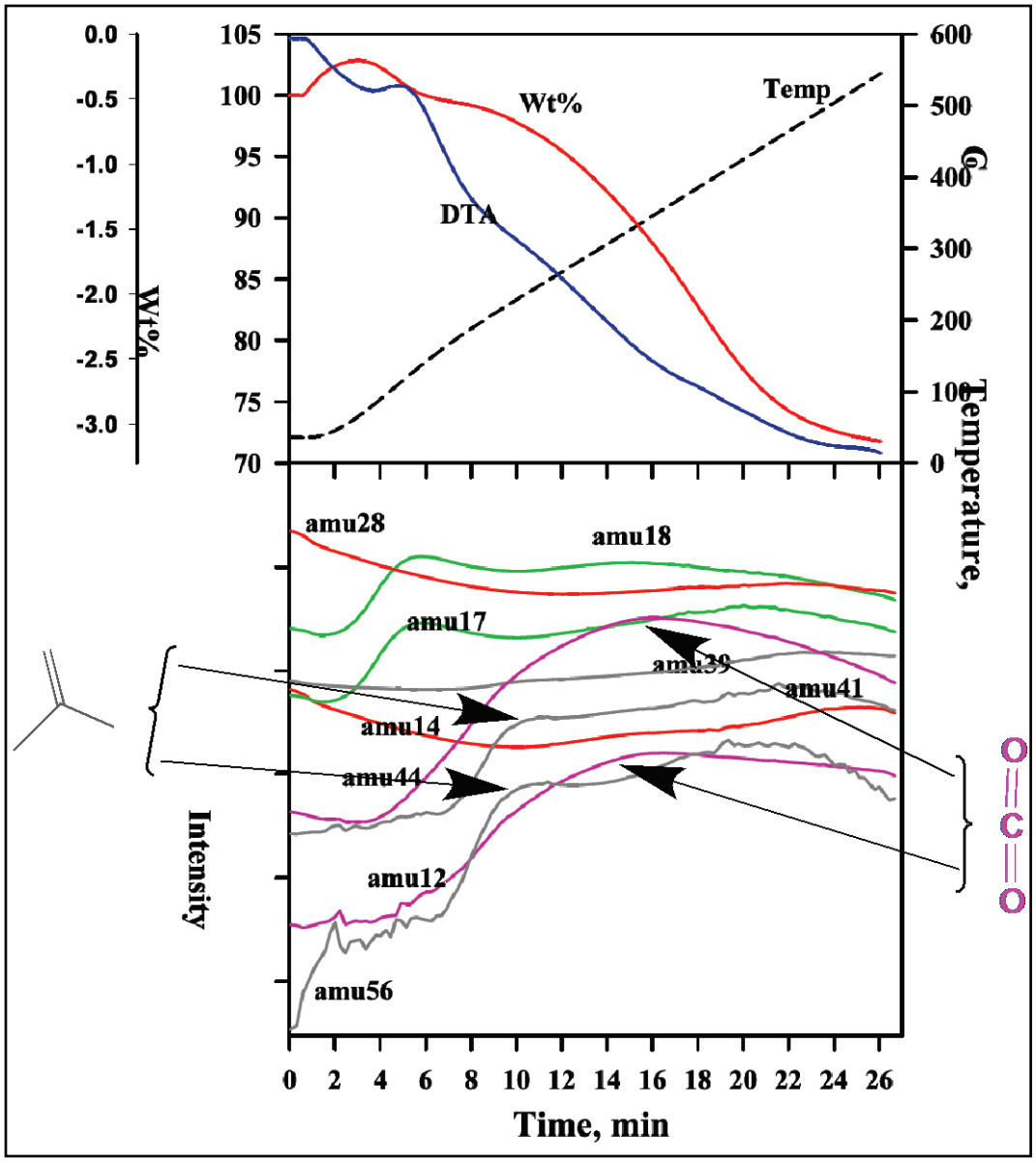

Figure 4.6 TGA-MS of **[G]**

4.7.3. Functionalization *via* Sandmeyer reaction

Gergely *et al.* reported that Sandmeyer reaction on SWNTs significantly increase their dispersibility in polar solvents.[83] A similar attempt has been made on N-CNOs using $FeSO_4$ as catalyst. **Scheme 4.5** shows stepwise depiction of N-CNOs modification by Sandmeyer reaction and subsequent sulfonation of the naphthalene moiety.

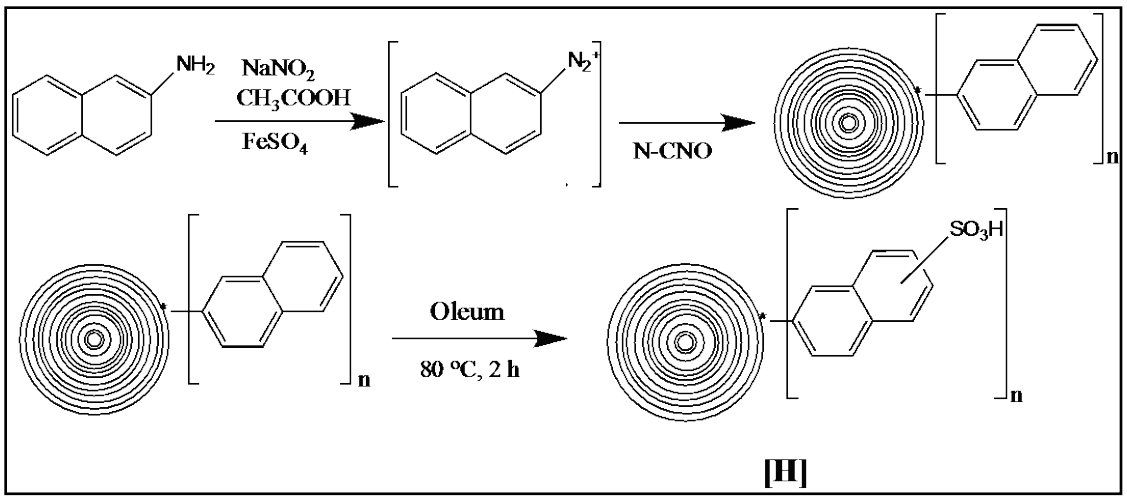

Scheme 4.5. Sandmeyer reaction and subsequent sulfonation of N-CNOs **[H]**

Thermogravimetric analysis (TGA) under air indicates a change in thermal stability of CNOs. Oxidative removal of the functional groups starts at about 440 °C and is complete at about 500 °C with ~19.6% mass loss (**Fig. 4.7**).

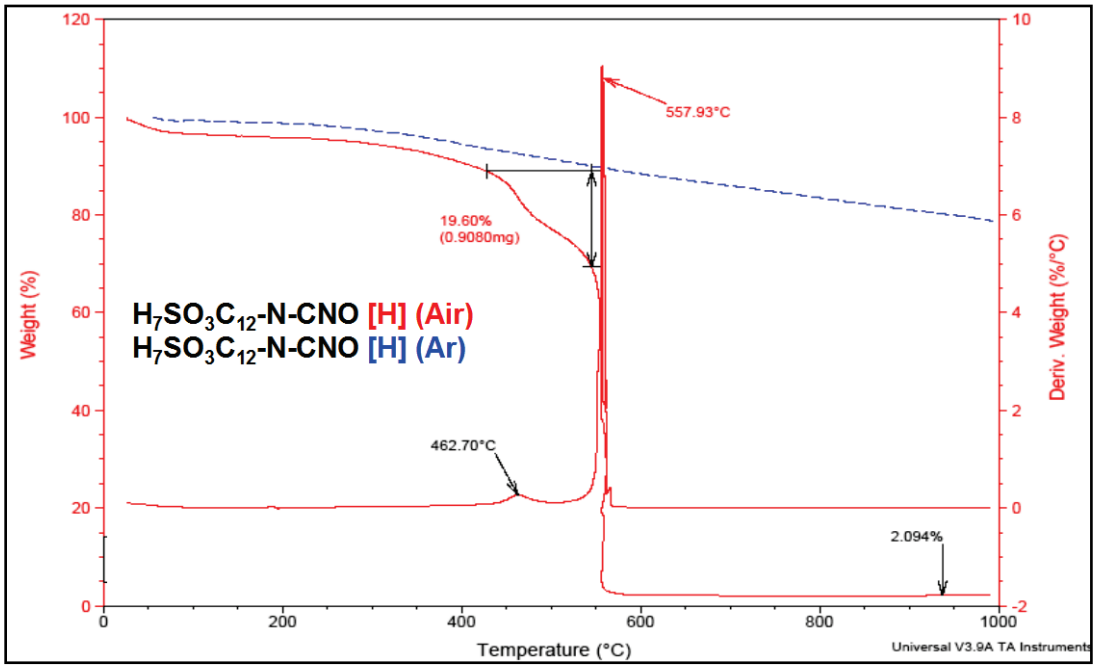

Figure 4.7. TGA (air and argon) compilation of functionalized CNOs *via.* Sandmeyer reaction **[H]**

Solubility/dispersibility of these modified CNOs was checked with nonpolar and semi-polar solvents. Very stable dispersions of the material were obtained in ethanol and DMF. Zeta potential measurements done in ethanol showed ζ = - 25.38 mV, which also supports high dispersibility of the sulfonated naphthalene-modified N-CNOs. However, the dispersibility was not good enough to observe strong enough ^{1}H NMR and IR signals to support the covalent functionalization of the desired groups.

4.7.4. Functionalization via oleum oxidation

Oleum can efficiently intercalate between highly entangled SWNTs, thereby enhancing their processability.[84] Introduction of –COOH groups *via* HNO_3 treatment of CNTs and CNOs is a well-established method. Tour *et al* have reported the use of oleum in combination with nitric acid to introduce –COOH groups on oleum-intercalated SWNTs.[66] We adapted a similar method to functionalize highly aggregated A-CNOs.

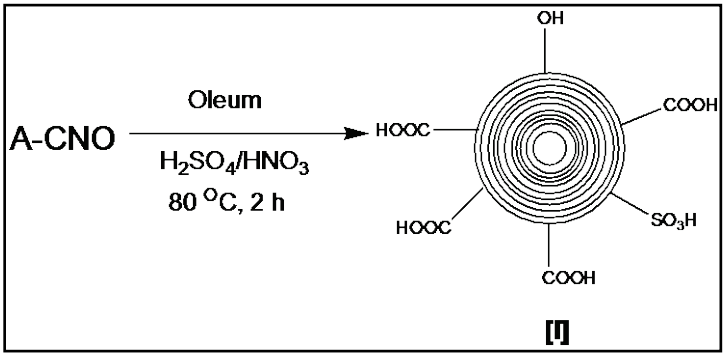

Scheme 4.6. Oleum-assisted functionalized groups on A-CNOs **[I].**

After oleum-assisted oxidation of A-CNOs, particles were found to be nicely dispersed in polar solvents such as water, ethanol, NMP and DMF. High dispersibility in polar solvents prevents these particles from coagulation even after several hours of centrifugation.

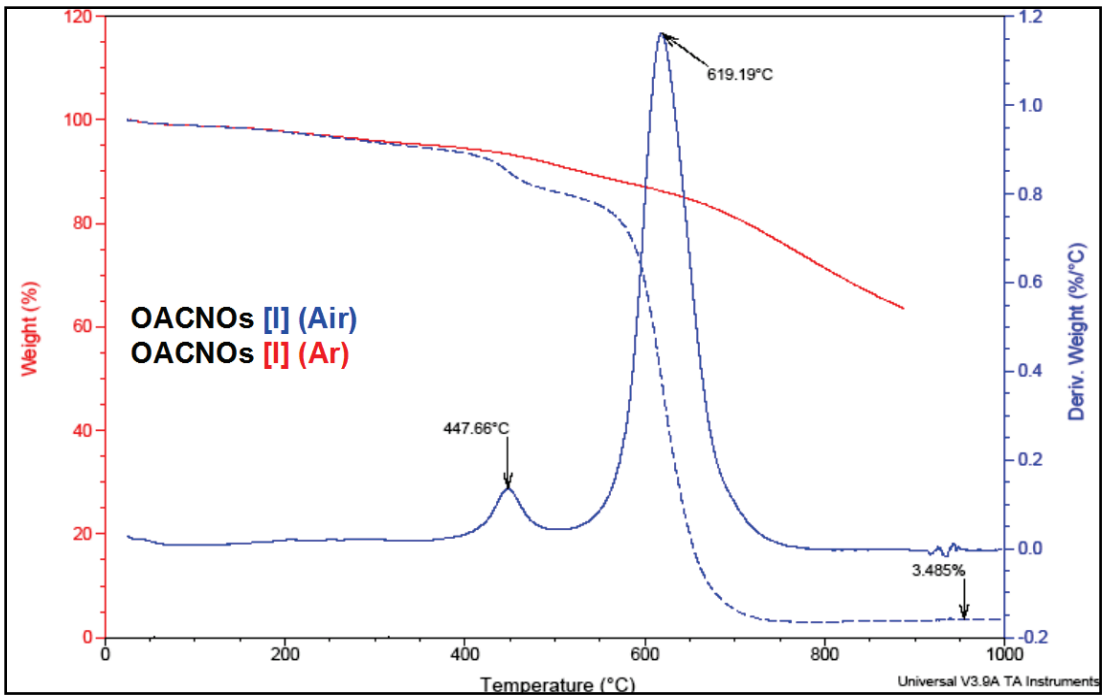

Figure 4.8. TGA overlay of oleum-treated A-CNOs under air and argon atmosphere

TGA also supports oxidative cleavage of functional groups bound to CNOs. A mass loss of 11% at about 448 °C under air indicates considerably high surface coverage by these functional groups. Moreover, TGA under argon showed no mass loss near 400–500 °C, supporting strong surface interactions **(Fig. 4.8)**.

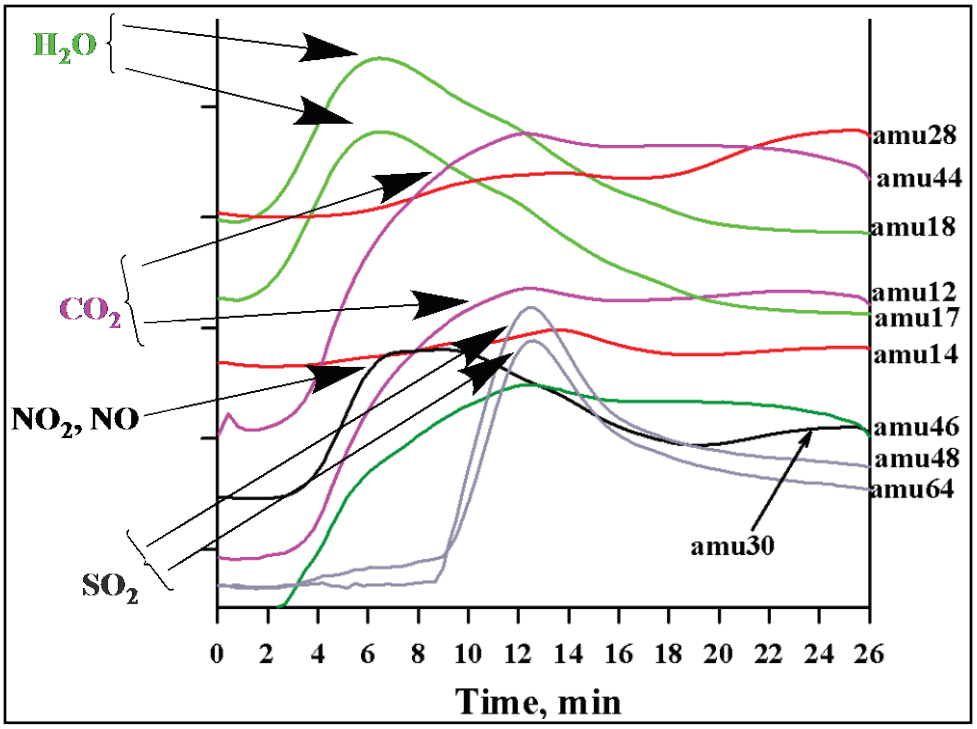

Figure 4.9. TGA-MS of O-A-CNOs **[I]**

Fig. 4.9 shows TGA-MS analysis of O-A-CNOs **[I]**, monitoring ions at 12 (C^+), 14 (N^+), 17 (OH^+), 18 (H_2O^+), 28 (N_2^+, CO^+), 30 (NO^+), 44 (CO_2^+, N_2O^+), 46 ($NO_2^{+)}$, 48 (SO^+) and 64 (SO_2^+) amu. Evolved H_2O yields OH^+ and H_2O^+. Evolved NO and NO_2 yield N^+, NO^+ and NO_2^+. Evolved CO and CO_2 yield C^+, CO^+ and CO_2^+, but N_2^+ interferes with CO^+ and N_2O^+ interferes with CO_2^+. Evolved SO_2 and SO_3 yield SO^+ and SO_2^+, but SO_3^+ is outside the range of the mass spectrometer.

The prominent parallel curves for 12 (C^+) and 44 (CO_2^+) amu ions at ~12 min. and 48 (SO^+) and 64 (SO_2^+) amu ions at ~12.5 min. correspond to CO_2 and SO_2 respectively indicate the presence of carboxylic acid groups along with sulfonic acid groups. Moreover, presence of prominent broad peak for 30 amu ion (NO^+) at ~7–10 mint. is also indicative of possible nitration of CNO surfaces.

Thus, TGA-MS analysis indicates that oleum-oxidized CNOs contain –OH, –COOH, $–NO_2$. and $–SO_3H$ functional groups.

Based on these acid groups on CNOs, further functionalizations were carried out *via in-situ* generation of acyl chloride and subsequent reactions with alcohols and amines to give esters and amides (**Scheme 4.7**).

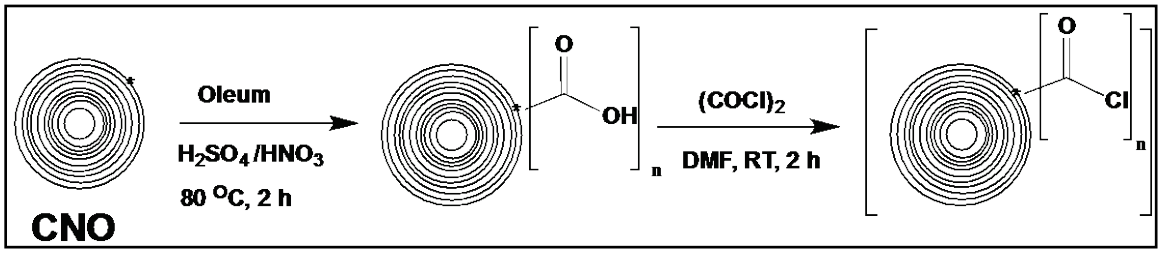

Scheme 4.7. Oleum-assisted carboxylation followed by conversion to chlorocarbonyl A-CNOs.

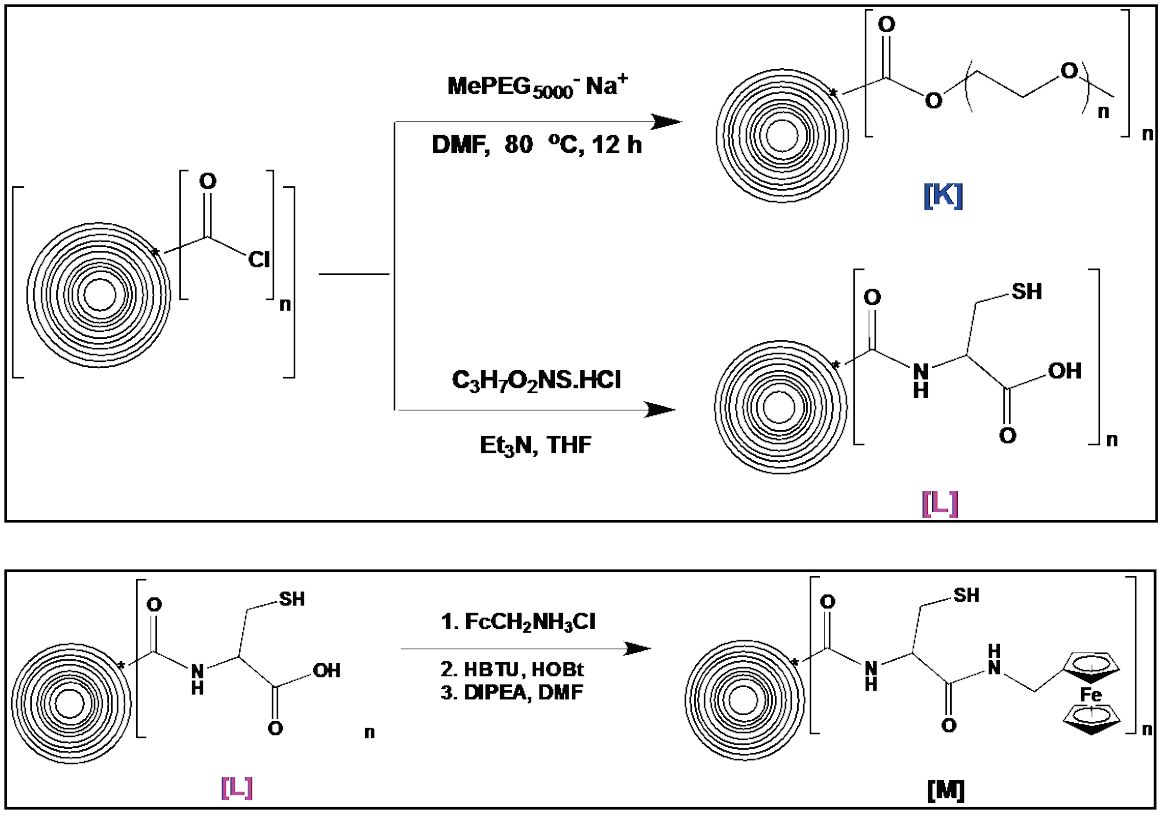

Scheme 4.8. Further functionalization approaches of chlorocarbonyl A-CNOs.

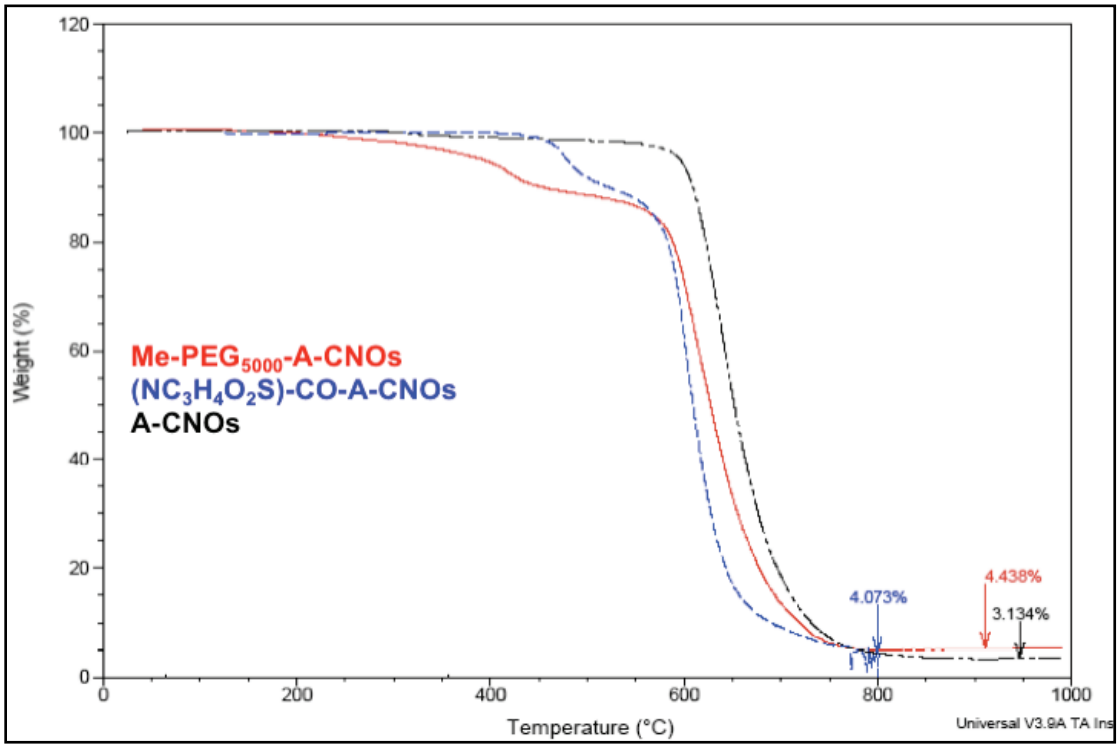

Figure 4.8. TGA compilation of **$MePEG_{5000}$-A-CNOs, [K]**; **$(C_3H_7O_2NS)$-CO-A-CNOs, [L]** and **raw A-CNOs**

Oleum functionalized CNOs, both A-CNOs and N-CNOs, were further functionalized with L-Cysteine. L-Cysteine-functionalized A-CNOs were studied by TGA, which showed ~10% weight loss at ~500 °C. This observed temperature is too high for the release of a weakly physisorbed species. To confirm that the mass loss was due to surface functional groups and to measure the surface coverage of CNOs, ICP analysis was done. A surface reactivity comparison was made between L-Cysteine-functionalized A-CNOs and L-Cysteine-functionalized N-CNOs via. ICP analysis.

ICP analysis detected a considerable amount of sulfur in the oleum-treated CNOs. This is in agreement with the fact that $–SO_3H$ groups are also active participants during oleum-assisted acid functionalization. The sulfur content per 1000 g of cysteine-

functionalized N-CNOs is approximately seven times greater than that of corresponding A-CNOs. This might be because of the high curvature and thus high reactivity of small onions. These reactivity differences are in agreement with results obtained by other groups.[33]

Based on the sulfur content, the surface coverage, i.e., number of functional groups per unit mass of CNOs, has been calculated as follows:

A-CNOs have an average diameter of 30 nm with 25-27 concentric shells. The inner core has an average diameter of 10 nm. Based on these dimensions, the surface area of a 30 nm spherical A-CNO is 2830 nm^2. Due to the larger size of A-CNOs than fullerene and N-CNOs, they can be considered more graphitic in nature. From the unit cell dimensions of graphite ($\alpha = \beta = 90°$, $\gamma = 120°$; a = b = 2.456 Å, c = 6.694 Å) and its surface area calculation, the number of carbon/nm^2 is estimated as 38.3. Using these approximations, the total number of carbons on the A-CNO surface is approximately 1.08×10^5. From ICP analysis, cysteine-functionalized A-CNOs have 2.8 g sulfur per kilogram of functionalized material. Based on the mole ratio of carbon calculated from the reported density of CNOs,[33] and functional groups, an empirical formula of $C_{89}S$ was obtained for total surface carbons. In other words, there is 1 sulfur for every 89 carbons on the A-CNO surface, corresponding to approximately 1.14% surface coverage of cysteine. Similar calculations for N-CNOs revealed an empirical formula of $C_{34}S$ with approximately 2.9% surface coverage. Also, ferrocene-attached A-CNO-cysteine materials were analyzed to quantify the Fe content of the sample. The Fe:S ratio tests the efficiency of converting cysteinyl acid [**L**] to cysteinyl amide [**M**]. The experimental

Fe:S ratio of ~0.91 indicates that the reaction (**Scheme 4.8**, [L] to [**M**]) proceeds in 91% yield.

Several other other amidation and esterification reactions of chlorocarbonyl A-CNOs were carried out. TGA analysis (**Fig. 4.8**) shows high combustion onset temperatures for surface-bound groups. These high-temperature mass losses indicate strong interaction of functional groups on CNOs' surface-active sites.

Zeta potential measurements were done on functionalized CNOs to account for their kinetic stability in suspension. A common polar organic solvent was chosen to compare differently functionalized CNO particles **(Table 4.2)**.

Table 4.2. Zeta potential measurements of functionalized and as-produced CNOs in ethanol

Material	**Material**	**ζ (mV)**	**Dispersibility**
A-CNO	As-produced	- 4.70	ND
N-CNO	As-produced	- 3.74	ND
A-CNO-COOH	**[I]**	- 14.71	D
N-CNO-COOH	**[J]**	- 53.28	WD
N-CNO-($OC_{41}H_{75}NO_2$)	**[F]**	+ 22.32	D
N-CNO-$C_{12}H_6SO_3H$	**[H]**	-25.38	D
A-CNO-CO($NC_3H_4O_2S$)	**[L]**	-36.16	WD
A-CNO-CO($MePEG_{5000}$)	**[K]**	- 29.20	WD

After bath-sonication for 5 min followed by centrifugation: ND = not dispersed, D = dispersed, WD = well-dispersed (stable after 2-3 h centrifugation)

In an organic medium without any other additional ionic species, the measured zeta potential is a direct approximation of particle surface potential. According to the DLVO (Derjaguin-Landau-Verwey-Overbeek) theory, there is equilibrium between the

van der Waals forces and the repulsion of the electrical double layer (EDL) around each particle, which provides colloidal metastability to the suspended particle. The double layer is formed either from surface ionic group dissociation or electron transfer between the medium and particle surface.[85, 86] The magnitude of the potential also depends upon the pK_a of the medium and the surface ionizing groups. In semipolar solvents with low dielectric constant, the π-network of the CNO surface can act as a Lewis acid by accepting electron pairs, rendering the surface potential negative. For raw CNOs, the zeta potential is mainly due to these electron-transfer interactions between the π-conjugated CNO surface and the medium. For functionalized CNOs, functional group (e.g., carboxylic acid) ionizations also contribute to the zeta potentials..

The negative zeta potential of the oleum-treated CNOs can be attributed to the ionization of carboxylic and sulfonic acid groups. The higher ζ value of N-CNO-COOH (-53.28 mV) compared to A-CNO-COOH (-14.71 mV) is consistent with the higher carboxylate surface coverage and concomitant greater dispersibility of N-CNO-COOH. A similarly negative potential, ζ = -36.16 mV, was observed for cysteine-derivatized CNOs, **L**. In case of pyrrolidine-functionalized particles, high positive zeta potential may be attributed to the amines acting as bases to form quaternary ammonium ions. However, low surface potentials observed may result from low ionization of these groups or high agglomeration of particles in absolute ethanol. Low ionization can be attributed to low dielectric constant or high pK_a of the ethanolic medium with respect to the surface functional groups, which in turn suppress sufficient electrostatic repulsion to prevent agglomeration. In most cases, physical observations made after sonication followed by

centrifugation of the dispersions in ethanol roughly agree with the empirical rule of $\zeta = \pm$ 30 mV for colloidal stability.

4.8. Summary

The initial goal of these studies was to achieve solubility/dispersibility of CNOs by covalent functionalization, and to thoroughly characterize the soluble CNOs. Several approaches effectively functionalized and solubilized both N-CNOs and A-CNOs. Strong van der Waals forces of CNOs make equal functionalization of individual CNO particles difficult; rather considering small aggregates with few CNOs is more plausible. Moreover, due to uncertainty in the molar masses of individual CNOs and their high polydispersity, functional groups in mole ratios can't be determined accurately. However, coulometric measurements and elemental analysis such as ICP can give a close approximation of the number of functional groups per unit mass of CNOs. This number is helpful in predicting solubility/dispersibility of CNOs in various solvents. Due to characterization difficulties of CNOs involving high-absorption of light, polydispersity, low-dispersability etc. no direct functional group characterization methods such as IR, NMR, UV-Vis, Raman can be used unambiguously. Thus proper combinations of different methods, such as TGA, TGA-MS, ICP-MS, CV and control reactions are utilized to provide sufficient data to support observed physicochemical changes in these materials.

Chapter V: Application of CNOs as Electrode Material for Electrochemical Double-Layer Capacitors

5.1. History

Electrochemical capacitors, also known as ultracapacitors or supercapacitors, store energy at the interface of the electrode and electrolyte. Therefore, they are also referred to as electrochemical double-layer capacitor (EDLC). The storage of electric chrage on metal surface have been studied since 1745 with the invention of the Leyden jar. The study and applications of EDLCs gained pace after the patent filed by General Electric in 1957, using porous carbon electrodes. The patent assumed that the charge was being stored in the pores of the carbon, producing exceptional charge storage.[87] In 1966, The Standard Oil Company, Cleveland, Ohio patented an energy storage device that stored chrage at the double-layer interface.[88] They utilized carbon paste soaked in electrolyte. Later SOHIO sold the license to Nippon Electric Company (NEC), which produced the first commercially available EDLC under the trade name of "supercapacitor".[89] These supercapacitors were initially used for memory back-up applications. In terms of energy density and power density, EDLCs serve as a bridge between high-energy-density batteries and high-power-density electrolytic capacitors.

5.1.1 Electrochemical double layer theory

For an ideal capacitor the charge is stored at the surface of the electrode by physical interactions of ions, and the charge–discharge can be carried out very rapidly over and over without any limitations. The performance of a capacitor is measured in capacitance. Capacitance is defined as the amount of electric charge stored in an electrode. In a capacitor, capacitance depends upon the area of the electrode, dielectric

constant of the electrolyte, and the distance between the electrodes, according to the **equation 1**.

$$\frac{C}{A} = \frac{\varepsilon_r \varepsilon_o^*}{d} \quad \textbf{(1)}$$

where C is capacitance (F), A is area of the electrode, $(\varepsilon_r\ \varepsilon_o^*)$ is the relative dielectric constant of the electrolyte, where ε_r and ε_o^* are the permittivity constant of the dielectric and vacuum, respectively.[90]

Thus, high surface area, more conductive electrolyte, and small separation between the electrodes are the key factors to achieve high capacitance from a material. Moreover, the redox properties of different chemical, such as metal oxide, polymer, organic groups can be used to further enhance the capacitance of a metarial. This enhanced capacitance obtained by redox properties of materials is known as pseudocapacitance. The schematic representation of an EDLC is shown in **Fig. 5.1**. Cations and anions accumulate on the oppositely charged electrodes. The ion-permeable separator is used to prevent electrical contact between the electrodes.

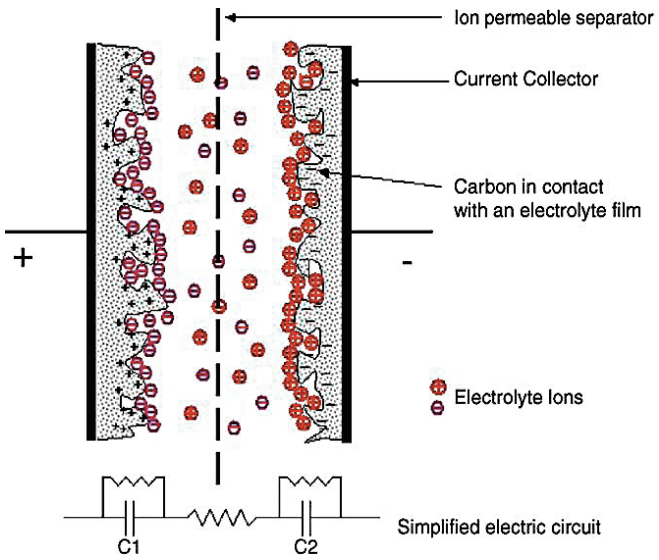

Figure 5.1. Formation of double layer in an EDLC cell configuration.[90]

The principle of electric double layer was initially proposed by three different models, namely HeImhotz model, Gouy-Chapman model, and Stern model as shown in **Fig. 5.2.**

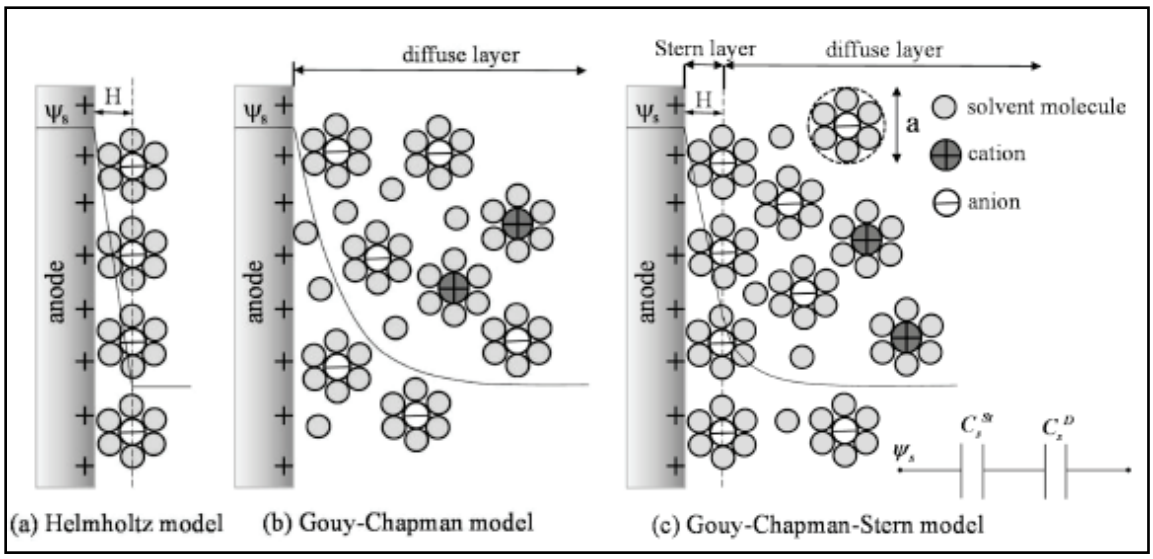

Figure 5.2. Comparison of theoretical models of double layer formation.[91]

In the Helmholtz model all the counterions were assumed to be adsorbed on the electrode surface; thus, the potential profile within the double layer is linear. This model does not include the effect of specially adsorbed ions and solvent molecules. The Gouy-Chapman model introduced the idea of diffuse layer to include the ionic mobility induced by diffusion and electrostatic forces; thus, the charge drops rapidly from the conducting electrode surface to the bulk of the electrolyte without any distinct layer separation. The Gouy-Chapman model can explain the effect of potential and temperature change only at low surface concentration of counterions. The Stern model combined the idea of a fixed Helmholtz layer model and diffuse layer model of Gouy-Chapman. At higher concentration of electrolytes, the effect of diffuse layer can be ignored. However, further

study is required to predict the double-layer behavior involving contribution from pseudocapacitance and nanoporous structure of electrode materials.

5.1.2 Supercapacitor vs. Battery

The fundamental difference in the principle of energy storage in supercapacitors vs. secondary or rechargeable batteries is the way in which the charge is stored. While in supercapacitors charge is stored directly at the surface of electrodes via physical interactions, batteries store energy in the bulk of chemical reactants that undergo redox reactions to generate charge. Thus, the rate of charge-discharge of batteries is limited by the reaction kinetics of the redox couples and the mass transport. On the other hand, an ideal supercapacitor is reaction kinetics independent and can undergo very rapid charge-discharge cycling, providing exceptionally high power capability. The important differences in the energy storage mechanism and applicability of battery and supercapacitor are summarized in **Table 1.**

Table 5.1. Basic comparison of batteries and supercapacitors.[90]

Property	Battery	Supercapacitor
Energy storage mechanism	Chemical	Physical
Energy storage determinants	Electrode active mass	Electrode surface area
Output voltage	Constant; state of charge (SOC) is unknown	Sloping value; SOC is known precisely
Specific energy ($Wh \bullet kg^{-1}$)	10–100	1–10 (for carbon)
Specific power ($W \bullet kg^{-1}$)	<1000	500–10000 (for carbon)
Charge/discharge rate, time	Governed by reaction kinetics and mass transport; hours	Very high; seconds–minutes
Cycle life limitations	Mechanical stability, chemical reversibility, ~1000 cycles	Side-reactions, >500,000 cycles

5.1.3 Non-ideality of electrochemical capacitors

Theoretically, an ideal capacitor shouldn't lose any power or energy during charge-discharge when cycled an infinite number of times. Also, a capacitor without current flow should retain the energy or charge indefinitely. However, in practice, no ideal supercapacitor exists. The non-ideality or aging of electrochemical capacitors comes from various factors such as:

(1) Voltage limitation

There is no issue of voltage limitation in an ideal capacitor. However, real capacitors operate only within the potential window determined by the electrolyte used. A voltage outside the window decomposes the electrolyte, resulting in cell damage. There are various advantages and disadvantages of aqueous and organic electrolytes. Organic electrolytes (~2.5 V) have higher potential window than aqueous electrolytes (~1.2 V); for high voltage requirements, multiple cells are connected in series. Commercial supercapacitors are unipolar; thus, voltage on the positive terminal is always more positive than the negative terminal, restricting the lower voltage limit to zero volt.

(2) Equivalent series resistance (ESR)

Due to the presence of resistance from the electrode itself, contacts and electrolyte, a real capacitor loses power during charge-discharge. The power loss is given by the equation, $P_{Loss} = i^2 ESR$, where i is current. The power is lost as heat, which can subsequently damage the cell.

(3) Leakage current (self-discharge)

Unlike an ideal capacitor, a real capacitor loses its voltage over time. Therefore, an external current, called as leakage current, is required to maintain the constant voltage

of the cell. Due to the leakage current, a charged capacitor without any external connections undergoes self-discharge.

(4) Cycle life

Unlike an ideal capacitor, the cycle life of a real capacitor depends on factors such as the rate of charge-discharge, voltage limits, ESR and cell type.

5.1.4 Electrode materials for EDLC

Different types of materials have been proposed as electrodes in EDLC. Most of the materials are based on carbon, such as amorphous carbon, carbon blacks, carbon fibers, carbon aerogels, glassy carbon, carbon nanotubes (SWNT, MWNT, FWNT), graphene, and transition metal oxides such as RuO_2, MnO_2, TiO_2 and Fe_2O_3. An ideal supercapacitor electrode has the following characteristics:

- high surface area
- appropriate porosity
- high conductivity
- good corrosion resistance
- high thermal stability
- processability and compatibility in composite materials
- low cost of manufacturing.

(A) Carbon. Carbon has four main crystalline allotropes: diamond (sp^3), graphite (sp^2), carbyne (sp), and fullerenes (distorted sp^2). Diamond and graphite are naturally found in the earth as minerals, and they are used to make engineered carbon materials by tuning surface area, porosity and conductivity. Charge storage in carbon materials is

predominantly double-layer capacitance. However, the presence of oxygenated groups on activated carbon surfaces induces pseudocapacitive charge storage. Tailored carbon particles possess a unique combinations of physical and chemical properties to meet the requirement of supercapacitor electrodes.

(B) Metal oxides. Transition metal oxides have been used to utilize the sequential redox reactions for high capacitance in EDLC. In these types of redox supercapacitors, the charge-storage mechanism involves both double-layer capacitance and pseudocapacitance of the materials. Carbon-only supercapacitors have the disadvantage of very low energy density (<10 Wh/kg) compared to batteries (35–150 Wh/kg). For higher energy density applications, other alternatives are redox active metal oxides, and their composites with high-surface-area carbons. Among metal oxides, RuO_2 gives the highest specific capacitance (~700–900 F/g), producing high energy and high power density in aqueous electrolytes. However, expensive RuO_2 supercapacitors are limited to military missile and aerospace applications only. Other metal oxides of interest are NiO, $Ni(OH)_2$, MnO_2, Co_2O_3, IrO_2, FeO, TiO_2, SnO_2, V_2O_5, and MoO.[92]

(C) Polymer. Conducting polymers such as polyaniline, polythiophene, poly(3-methylthiophene), are another type of material of interest for high-energy-density supercapacitor electrodes. These types of polymers undergo redox oxidation (doping) and reduction (dedoping) processes, where ions are transferred to and from the polymer backbone. The charge-discharge process takes place throughout the bulk of the material, unlike carbon particles.[93] As a result, high energy density can be achieved from polymer electrodes. However, low cyclic stability, and swelling and shrinking of these type of polymer electrodes is being a constant issue for practical applications. To address these

issues, composites of conducting polymer and carbon nanoparticles are being reported with limited success.[94, 95]

5.1.5 Electrolytes

Electrochemical capacitors can be categorized based on type of electrolyte used, which can be broadly divided into two types: organic and aqueous electrolyte. Both the electrolytes have it's own advantage and disadvantages. The breakdown voltages of organic electrolytes are usually in the range of 2.3–2.7 V, giving a much larger potential window (>2 times) than aqueous electrolytes. Since maximum stored energy is proportional to the square of cell voltage, organic electrolytes are commonly used for high-energy applications. However, the dielectric constants of organic electrolytes are much higher (~40 times) than aqueous electrolyte, resulting very high specific resistance. The high resistance of organic electrolytes affects the equivalent series resistance (ESR) of the cell, and consequently, as power is inversely proportional to the cell ESR, the maximum usable power reduces considerably. Another problem is associated with the presence of traces of water in the organic electrolyte. Therefore, extremely dry conditions are required to get higher voltage. On the other hand, preparing high-purity aqueous electrolytes needs less care. However, the breakdown voltage of aqueous electrolyte is only 1.2 V, typically 1.0 V is used, reducing the available energy significantly compared to organic electrolytes. The high dielectric constant of aqueous electrolyte (0.8 S/cm for H_2SO_4) keeps the ESR small, resulting in very high power density. Depending on the application, either organic or aqueous electrolytes are used for EDLC. Another interesting class of electrolyte is ionic liquids. Unlike organic solvents, ionic liquids are made up of anions and cations. Due to nonvolatility and nonflammability, they have the

advantages of thermal stability and safety over organic solvents. However, one of the basic criteria for solvents to use in EDLC is high electrolytic conductivity. Due to higher viscosity of ionic liquids, their electrolytic conductivity decreases rapidly with decrease in temperature.

5.1.6 Performance evaluation of the electrochemical double-layer capacitor

5.1.6.1 Cyclic voltammetry

Fundamentals

Cyclic voltammetry (CV) is the most popular method to study EDLCs. CV is used to determine potential widow, capacitance and cycle life of an electrochemical cell. For an ideal capacitor, with no redox couples, as voltage is swept across a potential window, the current initially increases rapidly and attains a steady state with constantly varying potential. At the reversal of the potential, current also changes, giving a rectangular CV plot as shown in **Fig. 5.3**.

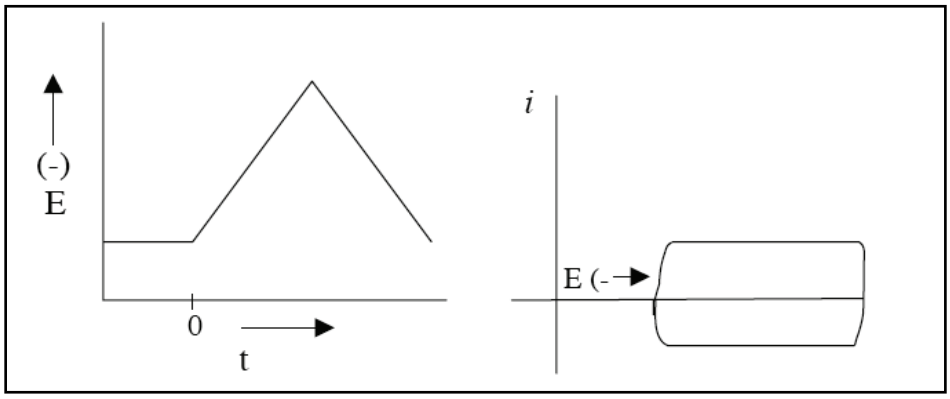

Figure 5.3. Time (t) vs. potential (E) and potential (E) vs. current (*i*) plots.[96]

We have

$$Q = CE \qquad (2)$$

where Q is the charge (coulombs), C is the capacitance (farads) and E is the cell voltage (volts).

Differentiating **Equation 2** we have,

$$\frac{dQ}{dt} = C\,\frac{dE}{dt}$$

or $$i = Cv \qquad (3)$$

where i is the current measured, which is determined by the integral of the area under the CV curve divided by the potential window, and v is the voltage scan rate.

In case of a redox couple, the Faradaic (electron-transfer) current is predominant over the capacitive current. Faradaic current depends on electron-transfer kinetics and the rate of diffusion of active species to the electrode surface. As shown in **Fig. 5.4.** for redox couples with fast electron-transfer kinetics, Faradic current obeys the Nernst equation

$$\boldsymbol{E = E^0 - 0.0592\log\frac{[R]}{[O]}}$$

where E is applied potential, E^0 is standard electrode potential and [R] and [O] are concentrations of reduced and oxidized species of the redox couple.

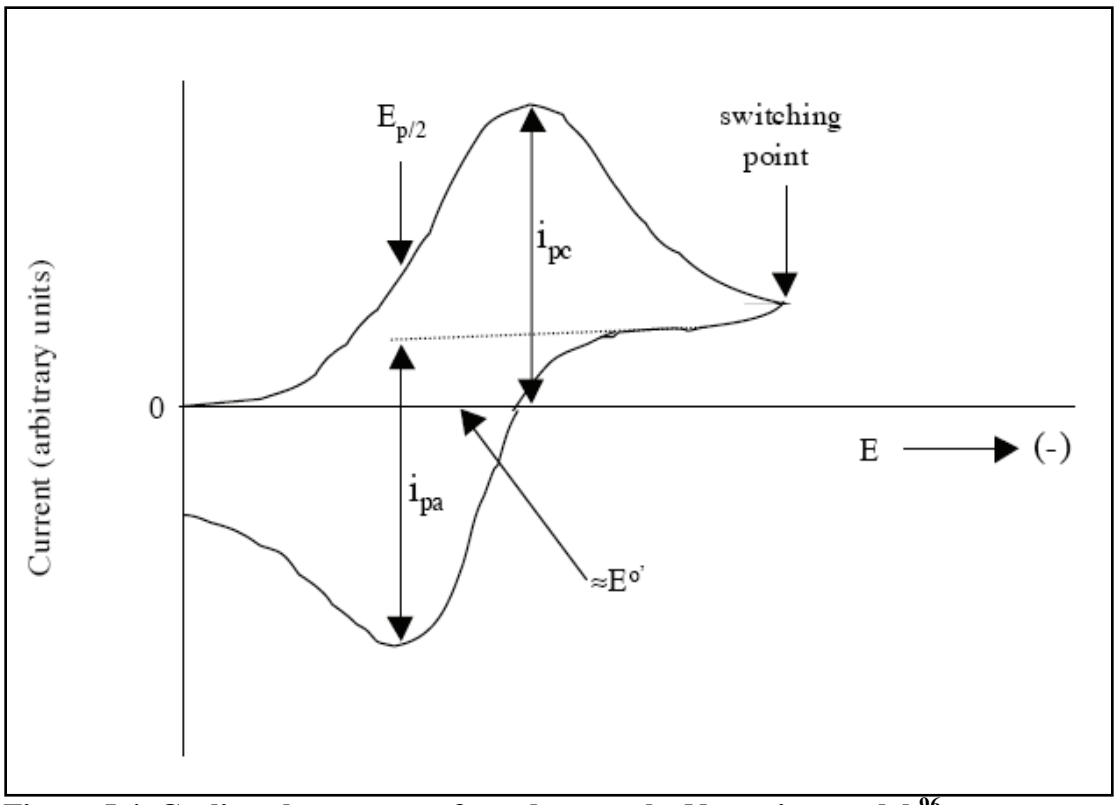

Figure 5.4. Cyclic voltammetry of a redox couple, Nernstian model.[96]

In case of redox supercapacitors, where both faradic and capacitive processes take place concurrently, the CV plot deviates from the ideal rectangular shape. **Fig. 5.5** compares an ideal capacitor eith a porous carbon capacitor with pseudocapacitive groups on its surface.

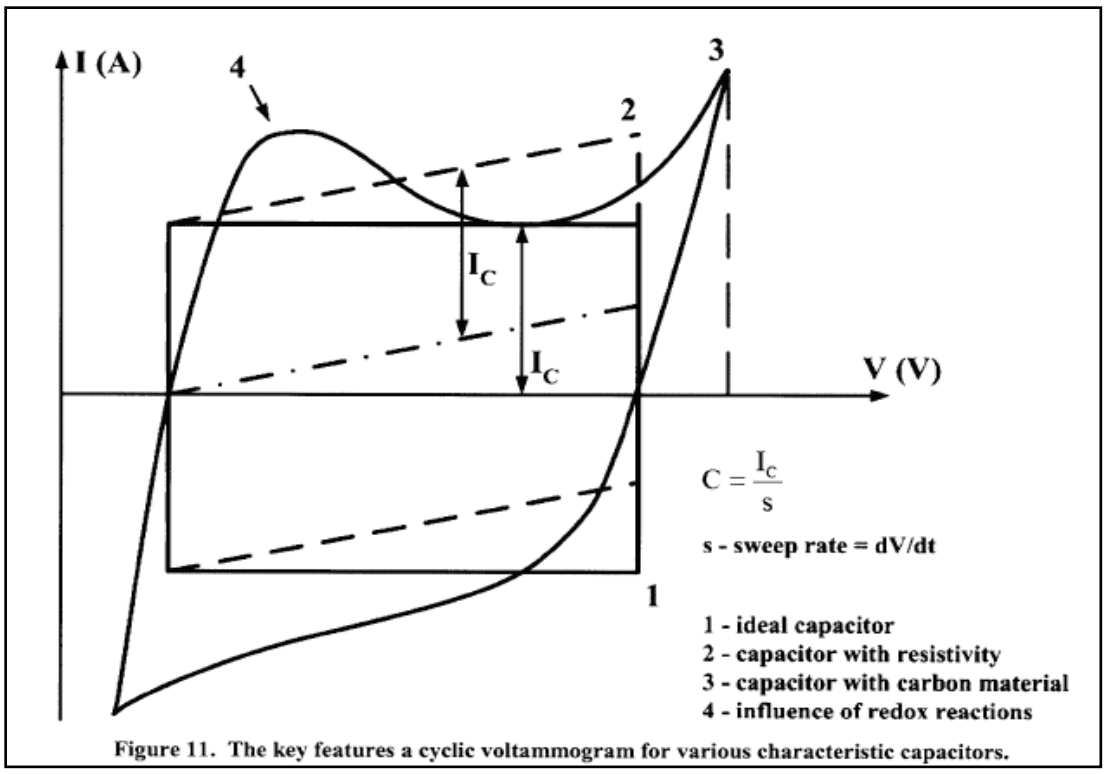

Figure 5.5. CV comparison of ideal vs. real capacitor electrode.[97]

In the case of redox supercapacitors, where metal oxides (RuO_2, MnO_2, Fe_2O_3 etc.) or electronically conducting polymers are used to obtain high pseudocapacitance compared to double-layer capacitance of carbon materials alone, the near-rectangular shape of the CV is due to successive multiple redox reactions of metal oxides, resulting high pseudocapacitive charge storage. **Fig. 5.6** demonstrates the successive redox cycles of a MnO_2 supercapacitor electrode.

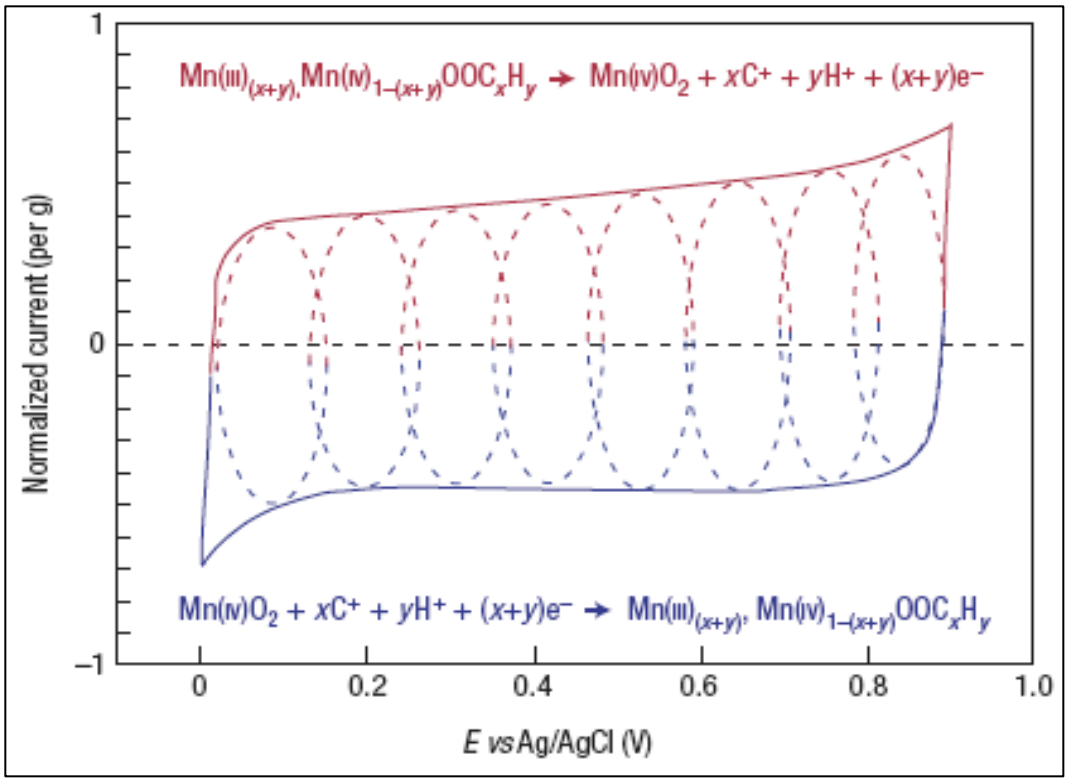

Figure 5.6. Pseudocapacitance from the successive redox cycles of MnO_2.[98]

1.1 Capacitance from cyclic voltammogram

The capacitance of an EDLC is determined from a CV plot, using the following equation:

$$\boldsymbol{C = dQ/dV = \frac{dQ/dt}{dV/dt} = \frac{i}{dV/dt}} \qquad (4)$$

where C is capacitance (F), Q is charge (C), t is time (s), i is current (A), V is potential window of measurement (V) and dV/dt is potential scan rate of the CV. The measured current is obtained from the height of the CV plot. A particular voltage is chosen, usually the midpoint of the potential window scanned, to measure the current in the vertical axis of i vs. V plot of CV. Alternatively the whole area under the CV can be integrated and divided by 2 X voltage widow to get the average current produced.

$$C = \frac{|I_a - I_b|}{dV/dt} \quad (5)$$

where C is the cell capacitance, I_a and I_b are the anodic and cathodic currents (A) obtained by integrating the voltammogram and dividing by the voltage range.

5.1.6.2 Galvanostatic charge-discharge

Fundamentals

Galvanostatic charge-discharge or constant current charging (CC) method has same principle as that of cyclic voltammetry but with a fixed current (*i*) value. The change in potential (E) is plotted in the Y–axis versus time (*t*) in the X–axis. A representative CC plot for ideal and real capacitor is shown in the **Fig. 5.7**. In absence of internal resistance (iR) ideal capacitor produces a perfect triangular shape t vs. E plot. In a real capacitor contribution from pseudocapacitance and iR drop significantly deviate the ideal rectangular shape of the *t* vs. E plot. A curved charging segment of the CC plot indicates presence of pseudocapacitance from Faradic processes. In the discharge segment of the CC curve an initial sharp potential drop i.e. ohmic drop indicates the internal resistance (iR) of the cell, which can be determined from the relation E=*i* × R. The reversibility of charging–discharging processes are determined from the coulombic efficiency (CE) of the electrodes. Coulombic efficiency (CE) is defined by the equation:

$$CE = \frac{t_{discharging}}{t_{charging}} \quad (6)$$

where $t_{discharging}$ and $t_{charging}$ are discharging and charging time respectively. For an ideal capacitor *CE* =1. **Fig. 5.7** shows the typical features of a CC curve of a symmetric capacitor.

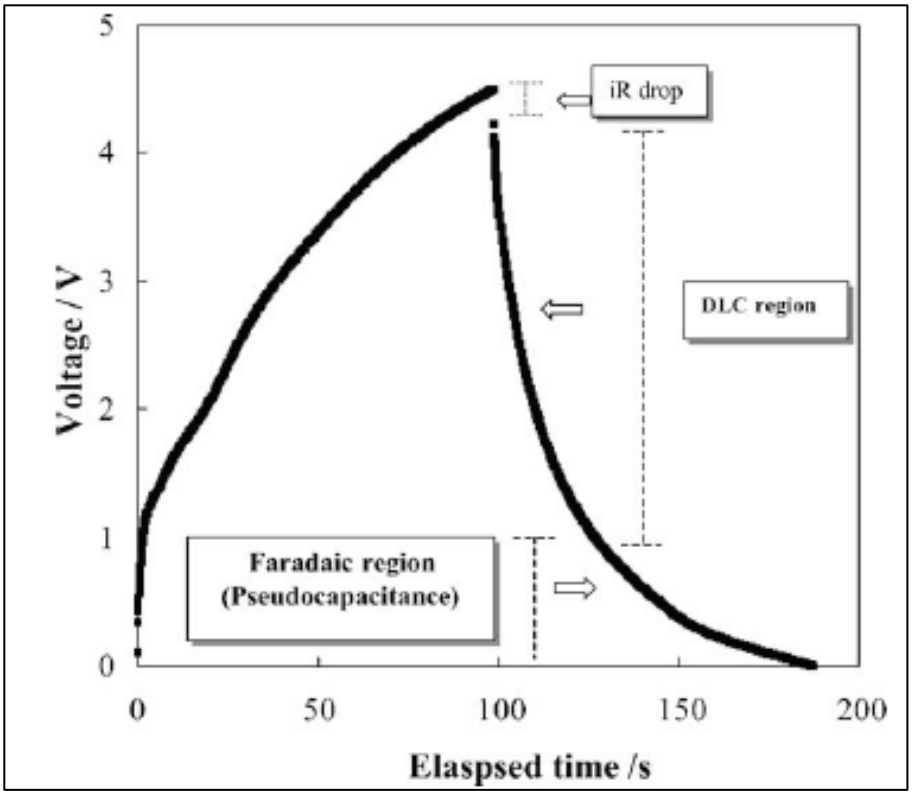

Figure 5.7. Galvanostatic charge discharge of capacitor electrode showing various features.[99]

The specific capacitance, C_{sp} can be determined from the slope of the discharge segment of the CC plot by using the following equation:

$$\boldsymbol{C_{sp} = \frac{C_1}{m_1} = \frac{2C}{m_1} = \frac{2i}{m_1(|\frac{dV}{dt}|)} = \frac{2i}{m_1(-slope)}} \qquad (7)$$

where C_1 and C are the capacitance of single electrode and the cell respectively, i is the current applied, [dV/dt] is the slope of the discharge curve after the initial iR drop, and m_1 is the mass of active electrode materials on one electrode.

5.1.6.3 Electrochemical Impedance spectra

Fundamentals

Electrochemical Impedance spectra is a measurement of the response of a circuit to the applied alternating current (AC) or voltage as a function of frequency (ω). When a potential is applied across an electrochemical cell, a current will flow through the circuit with a value governed by the mechanism of the reactions taking place. If the applied potential is sinusoidal ($\Delta E \sin\omega t$) the resultant current flow observed is also sinusoidal ($\Delta i \sin(\omega t+\phi)$), along with other hermonics of this sinusoidal current (2ω, 3ω, etc.). Where ω is frequency in radians per second ($=2\pi f$, f= frequency in Hertz), t is time, ϕ is phase shift in radians. This relationship of sinusoidal potential and current is known as impedance. **Figure 5.8**, showing the relationship of resistor, capacitor, and indicator in an AC circuit.

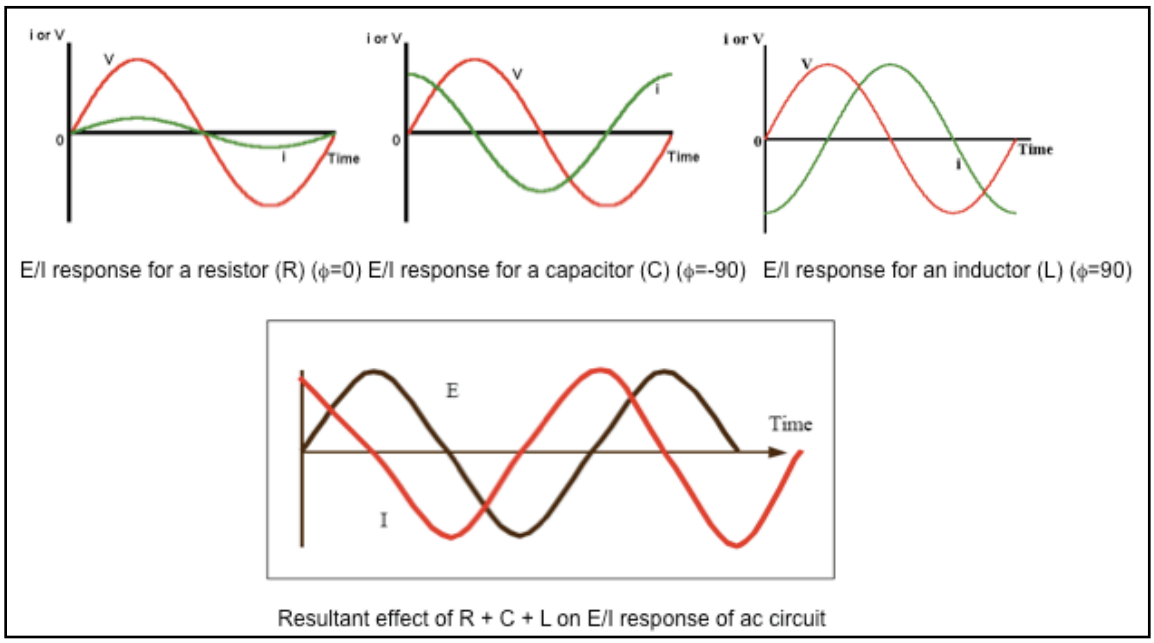

Figure 5.8. Illustrating behavior of **resistor (R), capacitor (C),** and **inductor (L)** in an AC circuit.

For Direct Current (DC) (ω=0), according to the Ohm's law $E=i \times R$, where R(Ω) is the resistance in the circuit. While in AC, with non-zero frequency, Ohm's law can be

written as $E=i \times Z$, where $Z(\Omega)$ is the impedance of the circuite. Resistance (R) in DC circuit and impedance (Z) in AC circuit impede the flow of current. However, in DC circuits only R resists the flow of current, but in AC circuits a combined effect of resistor and two other circuit elements namely capacitor (C) and inductor (L) impede the flow of current. Thus the impedance in ac circuit is expressed as a complex number, where resistance alone is the real component and the combination of capacitance and inductance is the imaginary component. In an electrochemical cell, the flow of electron is impede by the combine effect of slow electrode kinetics, slow Faradic reactions and ionic diffusion, which is analogous to resistor (0º phase shift), capacitor (90 º phase shift) and inductors in an AC circuit respectively. Another factor that influences the rate of electrochemical reactions is the diffusion of ions from the active surface to the bulk of the electrode. This particular component of the ac circuit, especially for porous electrode, towards total impedance is knowm as Warburg impedance (W). For such a diffusion-controlled electrochemical system, the current is 45º out of phase with applied potential.

The electric circuit containing all the components that influence the shape of the impedance spectra is called as equivalent circuit. For EDLC with porous electrodes, containing all the components namely resistor, capacitor, inductor, Warburg impedance, the equivalent circuit is represented by a Randles circuit (**Fig. 5.9**).

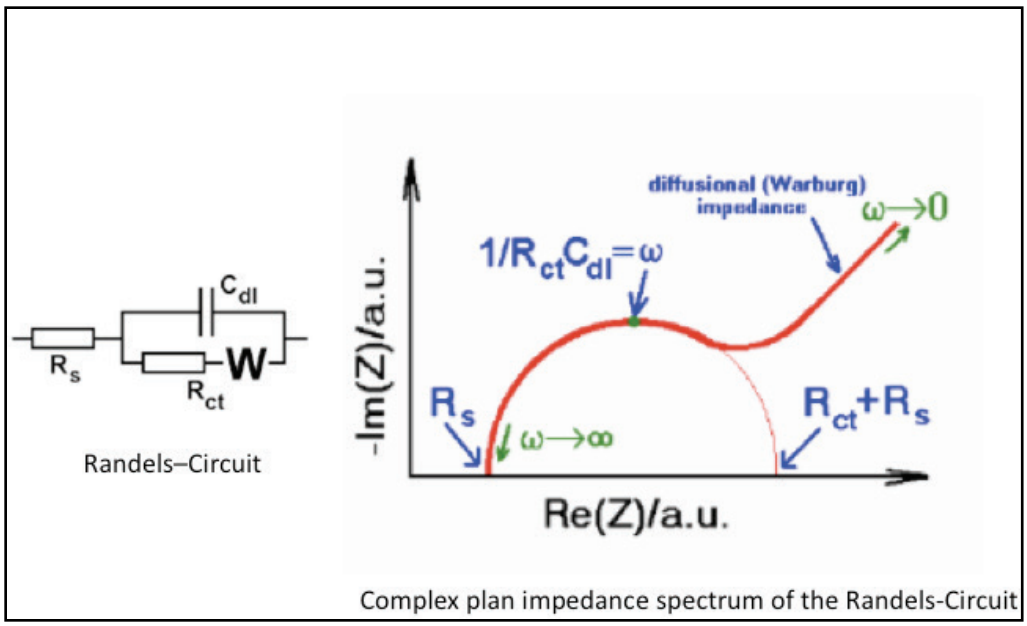

Figure 5.9. Model impedance spectra of Randels circuit for porous electrode.[100]

where R_s is solvent resistance, R_{ct} is charge transfer resistance, C_{dl} is double-layer capacitance, and W is diffusion (Warburg) resistance. **Fig. 5.10**, showing the Nyquist plot of an ideal capacitor and porous capacitor.

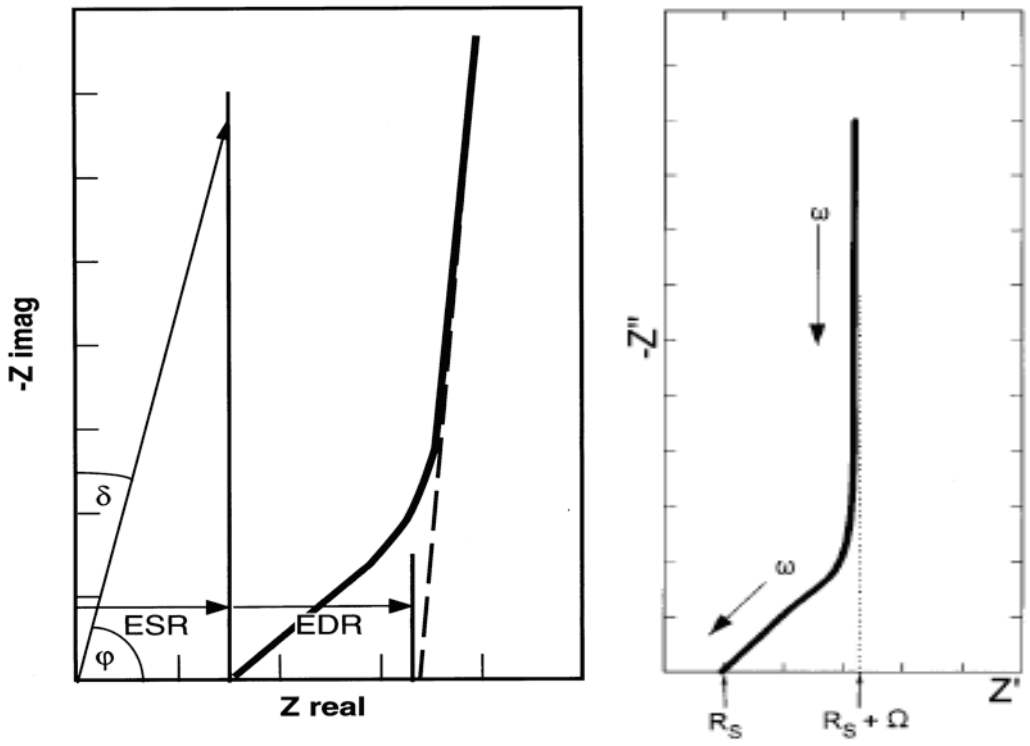

Figure 5.10. Model impedance spectra of ideal vs. porous EDLC.[98, 101]

Capacitance measurement

In EIS measurements, a very small excitation amplitude (usually 5–10 mV) is used so that the electrochemical system experiences only minimal perturbation. The imaginary part (Z'') of the impedance spectra at a particular frequency is used to find out the capacitance of the cell by using the following equation:

$$\boldsymbol{Z''(\omega) = -\frac{1}{\omega C}} \qquad (8)$$

where Z'' is the imaginary part of the impedance at frequency ω, and C is the capacitance.

Determination of specific capacitance

Electrochemical performance of materials for EDLC can be determined by different types of electrochemical cells. These cells are broadly divided in to two categories, namely three-electrode (half) cell and two-electrode (full) cell. The difference in cell type is schematically shown in the **Fig. 5.11**.

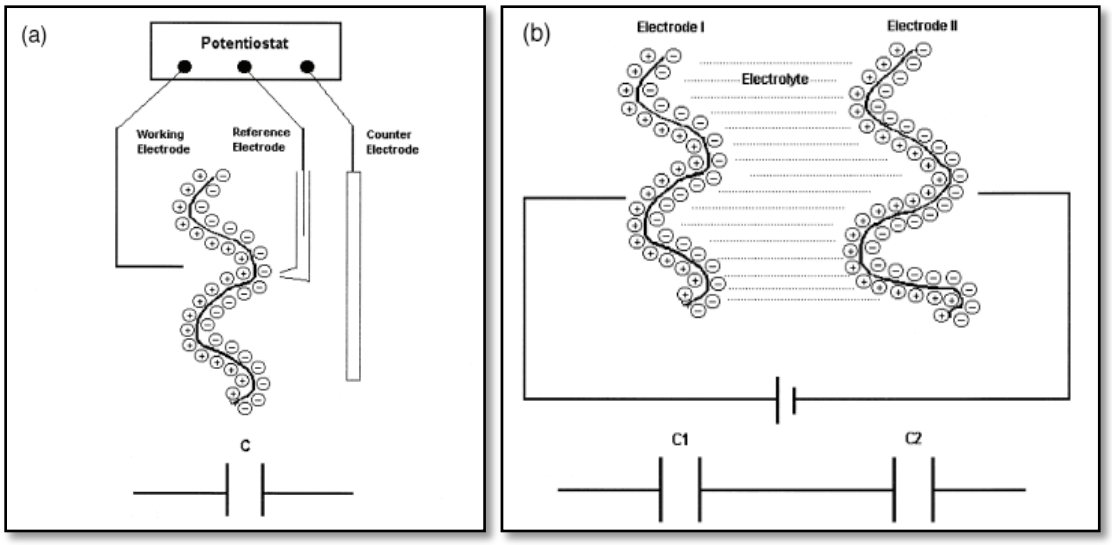

Figure 5.11. Three-electrode (half) cell vs. two-electrode (full) cell.[102]

In a three-electrode cell, active materials deposited on the current collector serve as a working electrode, a high-surface-area electrode such as graphite or Pt acts as a counter electrode with a reference electrode, usually Ag/AgCl. On the other hand, in a two-electrode cell, similar or different active materials are coated on two current collectors and stacked face-to-face. The electrodes are seperated by a thin, electrolyte-permeable membrane. In this type of two–electrode cell, no external reference electrode is used and the potential of the working electrodes are referred to each other. Due to these differences, during a potential scan, voltage experienced by the working electrodes is different in three-electrode half-cells and two-electrode cells. For example, for a scan of

0–1.0 V, while the working electrode in a half-cell experiences the complete voltage range, only half of the voltage applied (0–0.5 V) is experienced by each working electrode in a two electrode full cell. This results in double the capacitance measured in a three-electrode cell versus a two-electrode cell.[102, 103]

5.1.6.4 Notes on mathematical expressions

The definition of capacitance in farads (coulombs/volt) is

$$C = dQ/dV$$

Now,

$$C = dQ/dt$$

$$C = dQ/dV = \frac{dQ/dt}{dV/dt} = \frac{i}{dV/dt}$$

where i is electric current.

For supercapacitors, one quantity of interest is the specific capacitance, C_{SP}, which is expressed as:

$$C_{sp} = \frac{C}{m_{total}}$$

where m_{total} is the total mass (g) of active material in the symmetric supercapacitor including positive and negative electrodes. C_{SP} has the unit of F/g.

$$C_{sp} = \frac{C}{m_{total}} = \frac{Q}{\Delta E m_{total}}$$

The specific capacitance obtained from the above equation is with respect to the total cell capacitance. This equation is also used for measurements done in three-electrode cell. However, to express the specific capacitance of a single electrode, either

the positive or negative electrode in the symmetric cell, we must consider the configuration of a two-electrode cell. In a symmetric cell, the two electrodes can be considered as two equivalent capacitors connected in a series. For such a symmetric cell the total capacitance (C) can be expressed as

$$\frac{1}{C} = \frac{1}{C_1} + \frac{1}{C_2} \tag{9}$$

where C_1 and C_2 are the capacitance of individual electrodes with mass m_1 and m_2, respectively.

For a symmetric cell, $C_1 = C_2$ and $m_1 = m_2$; thus,

$$\frac{1}{C} = \frac{1}{C_1} + \frac{1}{C_1}$$

$$\frac{1}{C} = \frac{2}{C_1}$$

$$C_1 = 2C$$

So the specific capacitance of a single electrode can be given as

$$\boldsymbol{C_{sp} = \frac{C_1}{m_1} = \frac{2C}{m_1} = 2\frac{Q}{\Delta E m}} \tag{10}$$

where m = m_1 is the mass of a single electrode. C ($C = dQ/dV$) is obtained from either CV or CC measurements.

Again, to express the total specific capacitance of the cell

$$\boldsymbol{C_{sp\,(Cell)} = \frac{C}{m_{total}} = \frac{C_1}{2m_{total}} = \frac{C_1}{4m_1} = \frac{1}{4} C_{sp}} \tag{11}$$

where $m_{total} = m_1 + m_2 = m_1 + m_1 = 2m_1$ in a symmetric cell.
Thus, the single-electrode specific capacitance of a symmetric cell is four times larger than total cell specific capacitance.

The specific capacitance of the material is commonly expressed in terms of mass of the active material with a common unit of F/g. To account for the mass of binder and other additives, a correction factor (mass of active material/mass of total electrode) to the equation is used. For this correction factor, the capacitance of the binder and other additive should be negligible compared to that of active material. For non–negligible capacitance of additives, the real capacitance of the material is obtained by subtracting the capacitance of other additives.

Areal capacitance

The specific capacitance can also be expressed in terms of either geometric device area (F/cm^2) or the total surface area of the active materials (mF/cm^2). In theory, the capacitance of a material is directly proportional to the surface area (S) and relative permeability (ε) of the electrolyte, and inversely proportional to the thickness of the double layer (d); $C = S\varepsilon/d$. For example, if the average double-layer capacitance at the electrode/electrolyte interface of carbon with surface area 1000 m^2/g is 25 $\mu F/cm^2$, the theoretical specific capacitance of this carbon material is 250 F/g. However, in practice only about 1/10 of the theoretical capacitance is usually obtained. This is because of the non-accessible pores (micropores <2 nm) of the material, which contributes to the total surface area but are not available for double layer formation with electrolytes.[97] Thus, an areal capacitance with respect to geometric device area provides more information about material performance.

The areal capacitance (C_a) of a single electrode based on geometric device is calculated by using the following equation.[104]

$$C_a = \frac{2C}{m_1} = \frac{2i}{m_1(|\frac{dV}{dt}|)} = \frac{2i}{m_1(-slope)} \quad (12)$$

where i is the current applied, dV/dt is the slope of the discharge curve after the initial iR drop, and m_1 is the mass of active electrode materials on one electrode per square centimeter. For small devices with significant area restrictions, performance based on capacitance per area is more significant than performance related to mass.

Volumetric Capacitance

Capacitance per unit volume ($F \cdot cm^{-3}$). For commercial applications, volumetric capacitance of the EDLC is very important and in general, a value of the order of 60 F/cm^3 is required.[105] Volumetric capacitance is a combination of both gravimetric capacitance and density of electrode material. Intuitively, with increase in porosity and surface area of material the density of the material should decrease, resulting in high volumetric capacitance. However, with a highly porous structure the number of conductive pathways within the material also decreases, resulting in lower volumetric conductivity. Moreover for carbon materials, although they have similar porosity and surface area, the expected trend is infrequently observed due to the differences in physical and/or chemical structures.[90] Thus, an optimized condition is required to prepare materials with desired porosity and density to maximize volumetric capacitance.

The volumetric capacitance C_V, (Fcm^{-3}) of the single electrode is calculated by using the following equation.[106]

$$C_V = \frac{2C}{v} = \frac{2i}{v(|\frac{dV}{dt}|)} = \frac{2i}{v(-slope)} \quad (13)$$

where i (A) is the current applied, [dV/dt] is the slope of the discharge curve after the initial iR drop, and v (cm^{-3}) is the volume of the single electrode.

5.1.6.5 Determination of power density, energy density and Ragone plot

The power density and energy density of a supercapacitor electrode are expressed in the units of W/kg and Wh/kg respectively. The following relationships are used for unit conversions:

$$1\,J = 1\,CV = 1\,F\,V^2$$

$$1\,J = 1\,Ws = \frac{1\,Wh}{3600}$$

$$1\,J/g = \frac{1\,Wh/g}{3600} = \frac{1}{3.6}\,Wh/kg$$

The maximum energy density of a capacitor cell is given by

$$\boldsymbol{E_{max} = \frac{1}{2}\frac{C_{SP(Cell)}V^2}{3.6}\ (Wh/kg)} \qquad (14)$$

In terms of the specific capacitance of a single electrode, C_{sp} ($C_{sp} = 4C_{sp\,(cell)}$),

$$\mathbf{E_{max} = \frac{1}{2}\frac{C_{sp(Cell)}V^2}{3.6}\ (Wh/kg)}$$

$$\mathbf{E_{max} = \frac{1}{2}\,\frac{1}{4}\frac{C_{sp}V^2}{3.6}\ (Wh/kg)}$$

$$\mathbf{E_{max} = \frac{1}{8}\frac{C_{sp}V^2}{3.6}\ (Wh/kg)} \qquad (15)$$

where V is the cell voltage (potential window used to measure the capacitance).

The maximum power density of a capacitor is given by the following equation

$$\mathbf{P_{max} = \frac{1}{4}\frac{V^2}{R \times m_{total}}\ (W/kg)} \qquad (16)$$

where R is the equivalent series resistance obtained from the electrochemical impedance spectra (EIS) measurements or from the initial iR drop in the discharge curve of charge-discharge (CD) measurements.

The power density (P_{max}) and the energy density (E_{max}) of the supercapacitor calculated based on potential limits of the cell are defined as the theoretical maximum. In practice, usable cell potential for charge-discharge is limited to half of the theoretical limit.

Ragone plot:

A Ragone plot is a representation of power density vs. energy density of a device. It indicates the energy storage capability of EDLCs with respect to change in power. By applying different charging current a range of energy and power density values are obtained. The Ragone plots usually follow a knee shaped curve, where after certain critical power level energy density decreases rapidly (**Fig. 5.12**).

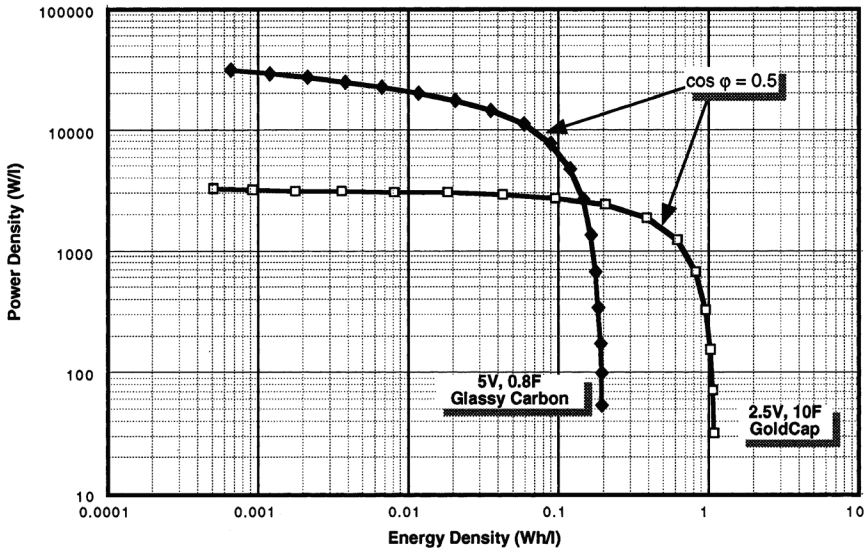

Figure 5.12. Ragone plot of two model EDLCs.[98]

5.1.6.6 Symmetric vs. asymmetric cell

A full cell is defined as symmetric or asymmetric, which is based upon whether the same or different types of electrode materials are coated on the current collectors. The asymmetric capacitor was introduced to increase the energy density of EDLC. Two different mechanism of charge storage are realized in the asymmetric or hybrid capacitor; while one electrode (negative electrode) stores energy via double-layer capacitance, the other electrode (positive) undergoes electrochemical reactions. So, asymmetric cells differ from symmetric ones in the availability of a "non-polarizable" electrode, where Faradaic electrochemical reactions take place. The presence of a non-polarizable electrode increases the capacity as well as potential window of the cell. This results in increased specific energy density in asymmetric cells by 2–5 times compared to the symmetric design. Another advantage of asymmetric cells is their low self-discharge due to the presence of only one carbon electrode, which is responsible for self-discharge in symmetric cells. However, the presence of a faradaic non-polarizable electrode reduces the cycle life of an asymmetric capacitor. Another disadvantage of asymmetric cells is their slower response (miliseconds), which is limited by Faradic reaction kinetics at the non-polarized electrode, compared to symmetric cells (20–40 microseconds) with two carbon electrodes. Therefore, the discharge time constant of an asymmetric cell is >1 sec, while that of an carbon-carbon capacitor is in the range of 50–300 ms.[107]

5.2 Experimental

5.2.1 Cavity Micro Electrode (CME)

A microelectrode was constructed as shown in **Fig. 5.13**. A Cu wire (length 8 cm, diameter 1.6 mm) was spot-welded to a thin Pt wire (length 1 cm, diameter 0.3 mm), and

3/4 of the wire was sealed in a soft glass tube (diameter 6 mm), leaving 2 cm of naked Cu wire to connect to the potentiostat. The other end of the electrode was polished to expose clean Pt surface for microcavity formation. The electrode was placed vertically in 15 mL of 1:3 v/v ratio of HNO_3:HCl at 80 ºC for 6 h. A conical microcavity formed on the Pt tip after the etching process. The electrode was washed several times with water and the volume of the cavity was measured under optical microscopy. The measured volume of the microcavity was ~19 × 10^{-6} cm^3. To measure the electrochemical performance of materials, the CME was pushed 3–4 times against the sample placed an a planar surface. To remove the sample after electrochemical measurements, the CME was bath sonicated in water for 3–4 minutes and dried under vacuum. This microelectrode served as the working electrode in a 3-electrode cell.

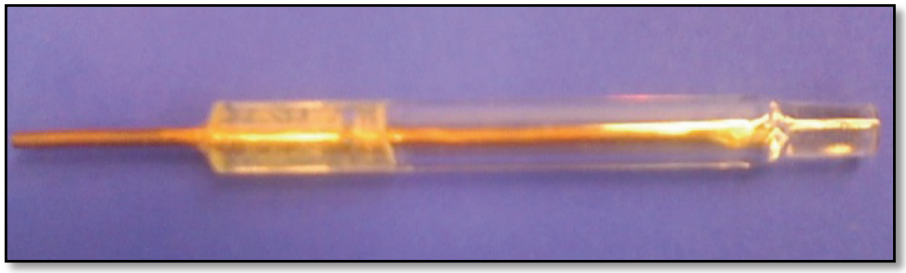

Figure 5.13. Cavity microelectrode **(CME).**

5.2.2 Swagelok cell

A Swagelok type cell was constructed by using two stainless steel rods pressed against each other tightly, as shown in Fig. 5.14. The electrodes were prepared by fabricating a thin layer (~6 μm) of 90–95 wt% active materials with 5–10 wt% poly(vinylidene fluoride) (PVdF) binder on gold plates (9.7 mm diameter × 0.14 mm thickness). The two electrodes were separated by a microporous tri-layer polypropylene

membrane (Celgard 3501, 25 μm) soaked with electrolyte and were assembled into the Swagelok cells.

Figure 5.14. Swagelok cell and Au plates coated with active materials.

5. 3 Synthesis

5.3.1 Preparation of OCNOs

A sample of CNOs (0.050 g) was dispersed in concentrated H_2SO_4 (35 mL) by stirring for 24 h at room temperature. A mixture of H_2SO_4 (15 mL) and HNO_3 (70%, 22 mL) was slowly added to the CNO dispersion with continuous stirring. During this addition, an ice bath was used to maintain the temperature close to room temperature. After about 10 min, the ice bath was removed and the resultant mixture was heated to 80−82 °C in an oil bath with continuous stirring for another 0.5 h. The dispersion was carefully poured into a beaker containing distilled water (300 mL) in an ice bath. The dispersion was centrifuged at 3500 rpm for 20 min and the water was decanted. The centrifugate was resuspended in distilled water (300 mL), centrifuged, decanted, resuspended in distilled water (300 mL), collected by filtration on a 0.2 μm microporous membrane, and finally vacuum-dried overnight at 45 °C.

5.3.2 PDDA-ONCNO

ONCNOs (0.120 g) were added to 200 mL deionized H_2O and stirred vigorously for 10 min, followed by horn sonication for another 5 min to obtain a well-dispersed solution. To this solution PDDA (0.2 mL) was added dropwise and stirring was continued at room temperature for 10 min. The resultant viscous reaction mixture was centrifuged and the product was separated out. The sample was washed several times (5 × 200 mL) with distilled water and filtered through a 0.2 micron membrane filter. The final product was dried under vacuum at 60 ºC overnight.

5.3.3 Preparation of RuO_2/OCNOs composites

$RuCl_3 \cdot 3H_2O$ (400.0, 100.0, 50.0, 37.5, 25.0, 10.0, and 5.0 mg) was dissolved in 120 mL distilled water. To this solution, 0.35 g/L glycolic acid was added and stirred for 10−15 min. The pH of this solution was adjusted to 7 by slowly adding 1.0 M NaOH. ONCNOs (100 mg) were added to the above solution, and the pH of the final mixture was again adjusted to 7. This reaction mixture was horn-sonicated (Sonic & Materials Inc. VC 600 sonicator, 50% duty cycle, microtip 2) for 10 min with cooling in an ice bath to minimize surface damage to the ONCNOs. The reaction mixture was stirred at 60 °C for 24 h in air and the resulting precipitate was washed with plenty of water. The material was vacuum-dried overnight at 60 ° C and annealed at 160 ° C for 4 h in air.

5.3.4 Layered MnO_2

Thin sheets of delaminated MnO_2 were prepared via an ion-exchange method reported in the literature.[108-110] In brief, a wet sample of K_xMnO_2 was proton-exchanged with 1-M HNO_3 at room temperature for 24 h followed by subsequent ion-exchange with

amines (TBA, DAO, 1:1 amine: Mn mole ratio). The delaminated MnO_2 layers form a yellow dispersion in water.

5.3.5 Preparation of MnO_2/OCNOs composites

In a typical synthesis of the MnO_2-PDDA-ONCNO composite, PDDA-ONCNO (0.040 g) in distilled H_2O (150 mL) was horn-sonicated for 10 min using an ice bath. To the well-dispersed PDDA-ONCNO solution, a calculated amount of delaminated MnO_2 dispersion was added and stirred at room temperature overnight followed by stirring at 70 ºC for 6 h. The resultant product was centrifuged, washed with water, and dried under vacuum at 60 ºC overnight.

5.4 Characterization

Thermogravimetric analysis (TGA). TGA analyses were carried out using a TA Hi-Res TGA 2950. In a typical run, 3–5 mg of the sample was loaded in a platinum pan and analyzed with a Hi-Res dynamic ramp (room temperature to 800 °C at 50 °C min^{-1} with a resolution factor of 4) under constant airflow (60 mL•min^{-1}). **Electron microscopy.** Size and morphology of the samples were imaged using a JEOL 2010F field-emission transmission electron microscope (TEM) equipped with an energy-dispersive spectrometer (EDS, Oxford).

BET surface area. The textural parameters of composite materials were determined by N_2 gas adsorption-desorption isotherms at a temperature of 77 K on an Accelerated Surface Area and Porosimetry System (ASAP 2020). Pore size and pore volume distributions were analyzed using density functional theory (DFT) calculation using the DataMaster™ software developed by Micromeritics Instrument Corporation.

Electrochemical measurements. Electrochemical tests were carried out using a potentiostat (MPG2, BioLogic) and an impedance analyzer (VMP3, BioLogic). Electrochemical behavior of the capacitor electrodes was studied by means of cyclic voltammetry, galvanostatic cycling, and electrochemical impedance spectroscopy (EIS). Cyclic voltammetry was conducted in the voltage range of 0 to 1 V. Galvanostatic cycling was carried out at a constant current density of 5 A/g in the voltage range 0–1 V for 3000 cycles. For EIS, the amplitude of the AC signal applied to the electrodes was 10 mV and the frequency was varied from 10 kHz to 10 mHz.

5.5 Results and Discussion

As-produced CNOs have high surface area, good conductivity and appropriate mesoporosity to serve as electrode materials for supercapacitor applications. In particular, nanodiamond-derived carbon nano-onions (NCNOs) with an average diameter of ~5–7 nm can be prepared in bulk quantities with homogeneous size distribution and high purity. NCNOs have BET surface area of ~520 m^2/g, electrical conductivity of 4 $S.cm^{-1}$ and high mesoporosity. Thus NCNO is a suitable candidate for high-performance composite electrodes for supercapacitor applications. Although the study of NCNOs for supercapacitors is not extensively documented, recent studies revealed their competitiveness with CNTs and other well-studied carbon allotropes.[36, 111, 112] **Table 5.2** comprises the single electrode specific capacitance of as-produced and modified CNOs in a two-electrode Swagelok cell with Au current collectors. 1.0 M H_2SO_4 was used as electrolyte and a potential scan rate 20 mV/s was applied.

Table 5.2. Specific capacitance of carbon materials in aqueous electrolyte (1.0 M H_2SO_4).

Material	Synthesis Condition	Ratio,	Conductive Carbon % wt.	CV average Specific Capacitance (F/g)
A-CNO	Under water arc	–	–	10
N-CNO	1650 ºC, He	–	–	27
N-CNO	1900 ºC, He	–	–	25
OACNO	H_2SO_4/HNO_3	–	–	36
ONCNO	H_2SO_4/HNO_3	–	–	45
ONCNO	H_2SO_4/HNO_3	–	Super C65, 2.5	75
ONCNO	H_2SO_4/HNO_3	–	Super C65, 5	76
ONCNO	H_2SO_4/HNO_3	–	Super C65, 10	80
OACNO + ONCNO	H_2SO_4/HNO_3	1:2	–	60
OACNO + ONCNO	H_2SO_4/HNO_3	2:1	–	50

To increase their surface wettability, carbon nano-onions were functionalized with polar carboxylic acid groups. For aqueous electrolyte, hydrophilicity of the electrode facilitates access of the ions to the electrode/electrolyte interface, enhancing charge storage. To maximize the capacitance of ONCNO and OACNO, functionalization conditions (oxidation time, temperature and concentration) were optimized. Although oleum-assisted carboxylic acid-functionalized CNOs are very well dispersed in aqueous media, CV measurements showed more resistive plots with small change (~1–3 F/g) in specific capacitance of the materials. This might be because of the disruption of the surface graphitic nature of the NCNOs under the harsh oleum oxidation conditions. This might also lead to lesser conductivity of the materials. Therefore, instead of oleum, a combination of H_2SO_4 and HNO_3 with shorter oxidation time (0.5 h) was used as mentioned in the section 5.3.a. To further enhance the conductivity of the material, a conductive carbon (SUPER65) was utilized with various proportions to ONCNOs. The addition of Super65 (~2.5 wt%) increased the specific capacitance of the ONCNOs to

~75 F/g. However, even at higher concentration (10 wt%) of Super65, the specific capacitance of ONCNOs increased only by ~5 F/g. Although we anticipated that a mixture of OACNOs and ONCNOs could enhance conductivity of the material via better interparticle contact and also maintains appropriate porosity for ion diffusion, as seen from the table 2, the combinations increased the specific capacitance only by ~5–15 F/g as compared to ONCNOs.

Metal oxide-CNO composite materials for EDLC electrodes

RuO_2/OCNOs. To maintain a homogeneous distribution of RuO_2 particles on the surface, carboxylic acid-functionalized CNOs were used. **Scheme 5.1** depicts the synthesis of composite material.

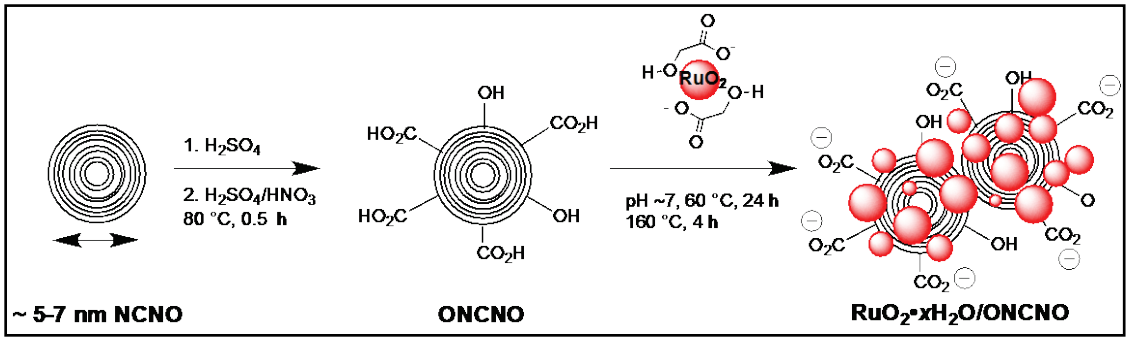

Scheme 5.1. Decoration of the surface of NCNOs with RuO_2•xH_2O nanoparticles.

The formation of acid groups on the surface of carbon nanoparticles by treatment with nitric acid is well documented.[66, 73] After this treatment, oxidized NCNOs (ONCNOs) are very well dispersed in aqueous solvents. However, care must be taken so that during functionalization, the surface modifications do not abruptly change conductivity as well as thermal stability of the material. Oxidation for a short interval (30 min at ~80 ºC) gives the highest specific capacitance for ONCNOs. The presence of

strong interactions between the carboxylate groups and the RuO_2 nanoparticles helps to prevent agglomeration among the RuO_2 nanoparticles, thereby maximizing the RuO_2 surface area and facilitating access of protons into the pores. The presence of glycolic acid helps to grow homogeneous RuO_2 nanoparticles. In alkaline solution, glycolic acid dissociates to glycolate anion with the highest concentration of glycolate at pH > 6.[113] The glycolate anions induce a negative surface charge on the $RuO_2 \bullet xH_2O$ particles. As a result, electrostatic repulsion among particles controls the size distribution of growing $RuO_2 \bullet xH_2O$ nanoparticle precursors. A comparison of $RuO_2 \bullet xH_2O$/ONCNO nanocomposites synthesized with and without glycolic acid showed that glycolic acid increases the specific capacitance by ~20%. In the absence of glycolic acid, Kim and Popov found that the growth of larger $RuO_2 \bullet xH_2O$ particles caused a decrease in RuO_2 utilization and its rate capability.[114]

The $RuO_2 \bullet xH_2O$/ONCNO nanocomposites were prepared via precipitation from aqueous media. Maintaining pH ~7 is important not only after the initial mixing of $RuCl_3 \bullet 3H_2O$ and glycolic acid during the growth of nanoparticles, but also after addition of oxidized CNOs (ONCNO). The specific capacitance of composite materials was found to increase by ~60% when the final pH was ~7 rather than pH ~4.5 after mixing of ONCNOs into the neutralized solution of glycolic acid and $RuCl_3 \bullet 3H_2O$. Therefore, for all the syntheses glycolic acid (0.35 $g \bullet L^{-1}$) was used and the pH of the final solution was maintained at ~7.

In the second step of synthesis, water content and the amorphous nature of the $RuO_2 \bullet xH_2O$ were maintained by heating the composites to 160 ºC for 4 h. Above 200 ºC,

a phase transition occurs to form crystalline, rutile RuO_2, in order to prevent rapid faradic processes from occurring near the surface and lowering the specific capacitance.[115]

Fig. 5.15a compares the thermal stability of nanodiamond, NCNO and ONCNO. After high temperature (1650 ºC, He, 1 h) treatment of nanodiamond to form nano-onions, the thermal stability of the particles increases by ~80 ºC; the sharper combustion curve of NCNOs indicates a more homogeneous, single-phase material. For ONCNOs, a gradual mass loss is observed, which is a combination of loosely bound water molecules and the acidic functional groups at the surface of ONCNOs. TGA analysis under dry air was used to determine the Ru content of the composite materials. **Fig. 5.15b** shows the thermal stability and % RuO_2 of the nanocomposites. A small mass loss was observed for all the samples at ~100 ºC, assigned to the loss of loosely adsorbed water. In the temperature range 250–280 ºC, a gradual mass loss was observed for all samples. We attribute the mass loss in this range to a combination of the removal of acidic functional groups on the surface of ONCNOs and the conversion of metal oxide particles from $RuO_2 \bullet xH_2O$ to RuO_2 by losing strongly coordinated water molecules from the pseudocrystalline material. A sharp mass loss at 345–375 ºC is due to the complete combustion of NCNOs. Above 400 ºC, the residues are stable with no further mass loss, indicating the presence of pure RuO_2. The ratios of RuO_2 to NCNOs in the nanocomposites were calculated from the % residue at 800 ºC.

Nitrogen adsorption/desorption isotherms at 77 K were used to characterize the porous nature of the $RuO_2 \bullet xH_2O$/ONCNO nanocomposites. The adsorption/desorption isotherms are similar for both ONCNOs and composites, which indicates their similar porous nature. **Table 3** summarizes the pore size, pore volume, micropore volume and

corresponding specific capacitance of NCNOs and the nanocomposites. The BET surface areas decrease with increasing RuO_2 loading. Untreated NCNOs have BET surface area of 552 $m^2 \bullet g^{-1}$, while the acid-functionalized and metal oxide-impregnated nanocomposites have surface areas as low as 126 $m^2 \bullet g^{-1}$ (67.5 wt% RuO_2). When the concentration of RuO_2 particles (14.9 wt% RuO_2) is low, they also contribute to the overall surface area of the composite. With increasing RuO_2 loading, the cumulative surface area decreases rapidly (**Fig. 5.16a**). The decreasing trend is expected since the BET surface area is normalized per unit mass ($m^2 \bullet g^{-1}$) and Ru has much higher atomic mass than carbon. The presence of RuO_2 nanoparticles also effectively blocks the pores of the NCNOs, thereby preventing the access of N_2. However, the mesoporous (2–50 nm) nature of the NCNO/ONCNO starting material was maintained in all composite materials, which is essential for ion transport to the active mass of the electrode.

The reduction in pore volume of the composites compared to ONCNOs also indicates the blockage of mesopores (2–50 nm) by RuO_2 nanoparticles (**Fig. 5.16b**). Moreover, as shown in **Fig.s 5.16a** and 5.**16b**, there is only a small fraction of micropores (< 2 nm) available in all the composite materials. Since the micropore volume of the composites remains almost same, the concentration of RuO_2 has little to no effect on the micropore volume of the nanocomposites.

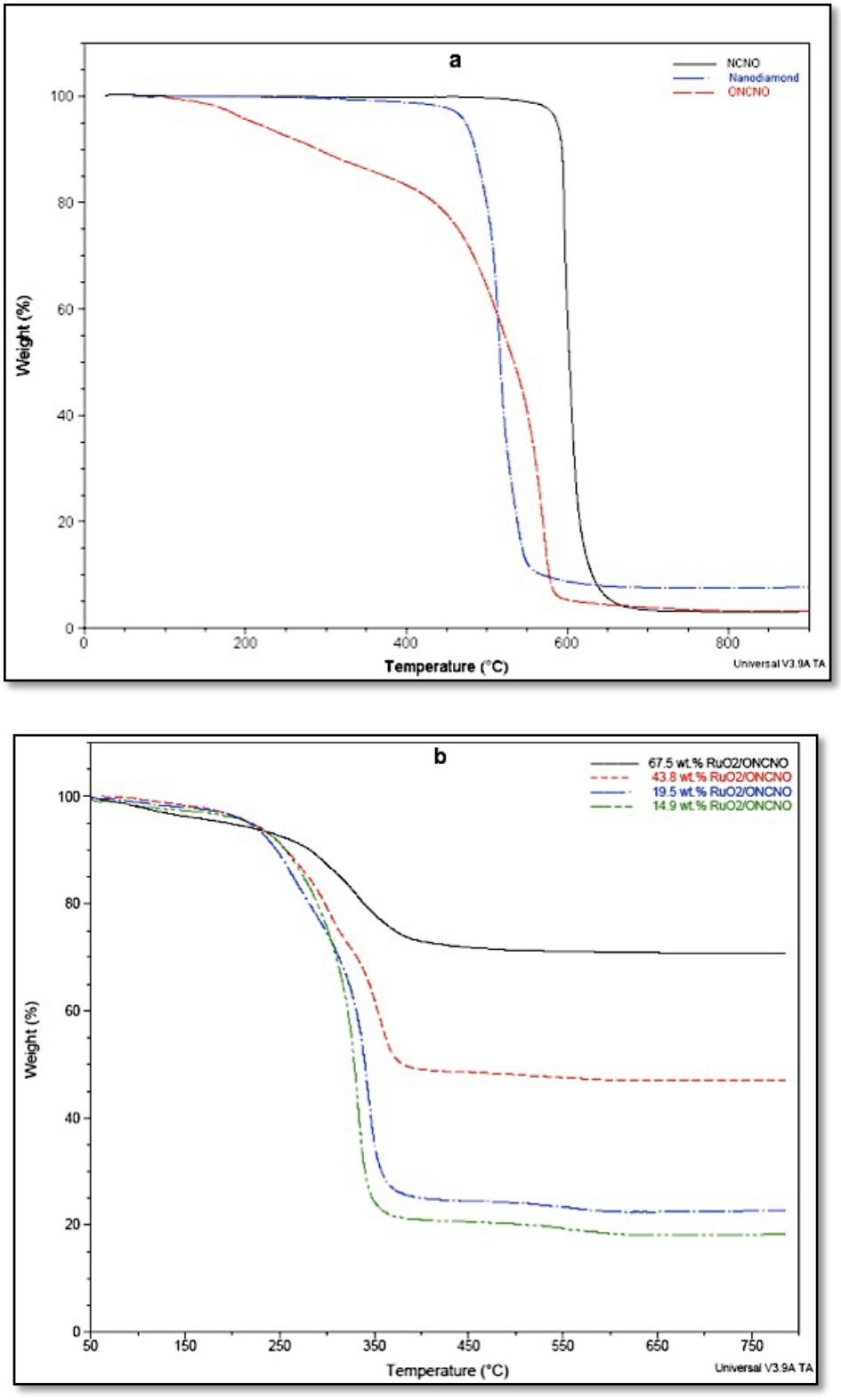

Figure 5.15. TGA overlay of (a) nanodiamond, NCNO and ONCNO (b) $RuO_2 \bullet xH_2O$/ONCNO electrodes with varying wt% Ru mass ratios.

Table 5.3. Textural parameters and capacitance of $RuO_2 \bullet xH_2O$/NCNO electrodes

Sample	Wt% RuO_2	BET surface area (m^2/g)	Pore size (nm)	Pore volume (cm^3/g)	Micropore volume (cm^3/g)	Capacitance (F/g)
NCNO	–	552	10.8	1.53	0.05	27
ONCNO	–	369	5.1	0.47	0.006	45
RuO_2/ONCNO	14.9	421	4.3	0.46	0.01	96
RuO_2/ONCNO	19.5	361	3.9	0.35	0.017	151
RuO_2/ONCNO	67.5	126	3.5	0.11	0.004	334

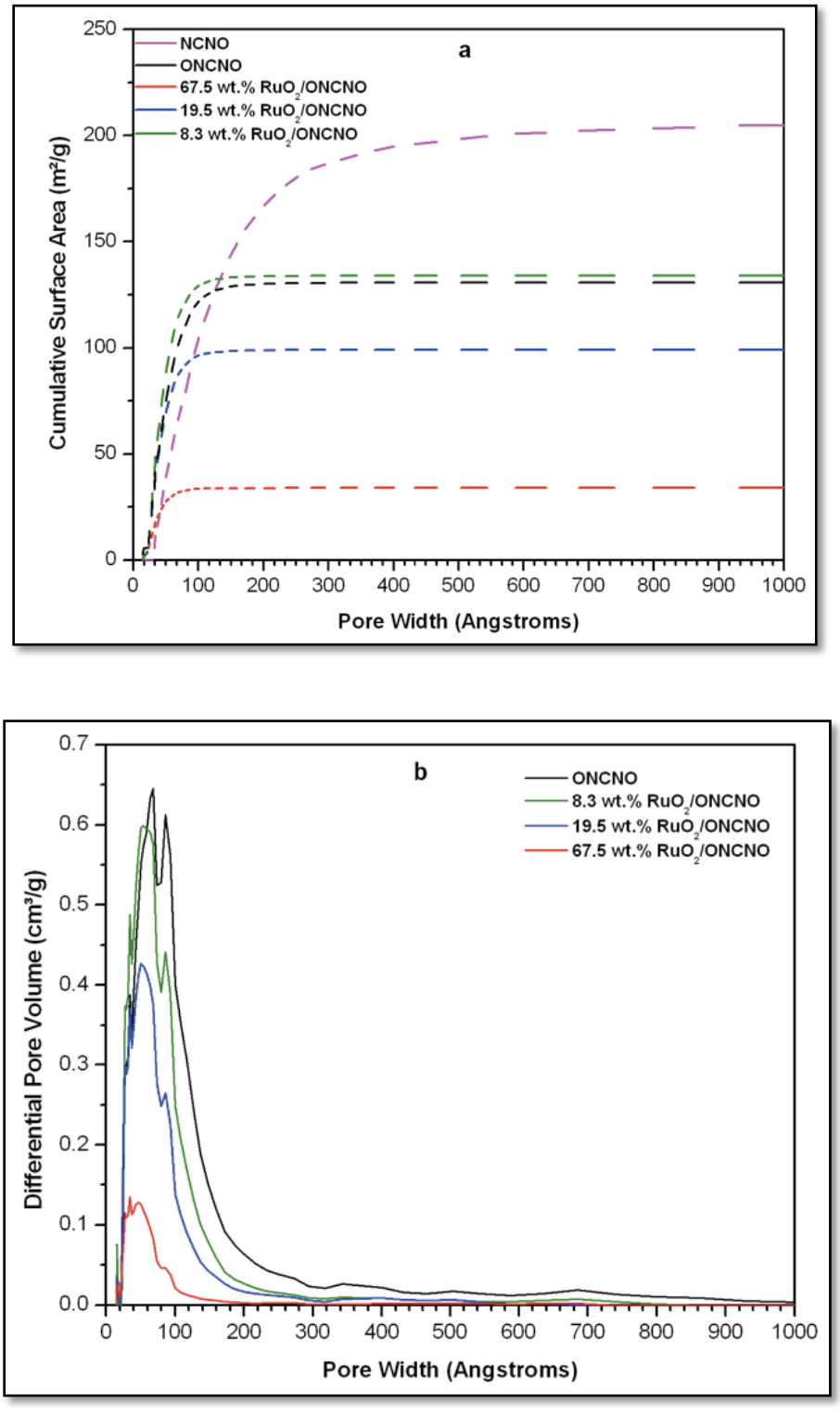

Figure 5.16. a. Surface area as a function of pore width of NCNOs and $RuO_2 \bullet xH_2O$/ONCNOs. **b.** Pore volume as a function of pore width of ONCNOs and $RuO_2 \bullet xH_2O$/ONCNOs.

The morphology of ONCNO and RuO_2•*x*H_2O/ONCNO composites was analyzed by HRTEM. In **Fig. 5.17** the dark spots indicate RuO_2 nanoparticles, as confirmed by EDS measurements. The RuO_2 particles, with an average size of ~2–3 nm, are homogeneously distributed throughout the sample. This is very important, since RuO_2 dispersion on carbon surfaces largely influences the pore size, interparticle conductivity and the efficient utilization of the active material for electrochemical double-layer capacitance.

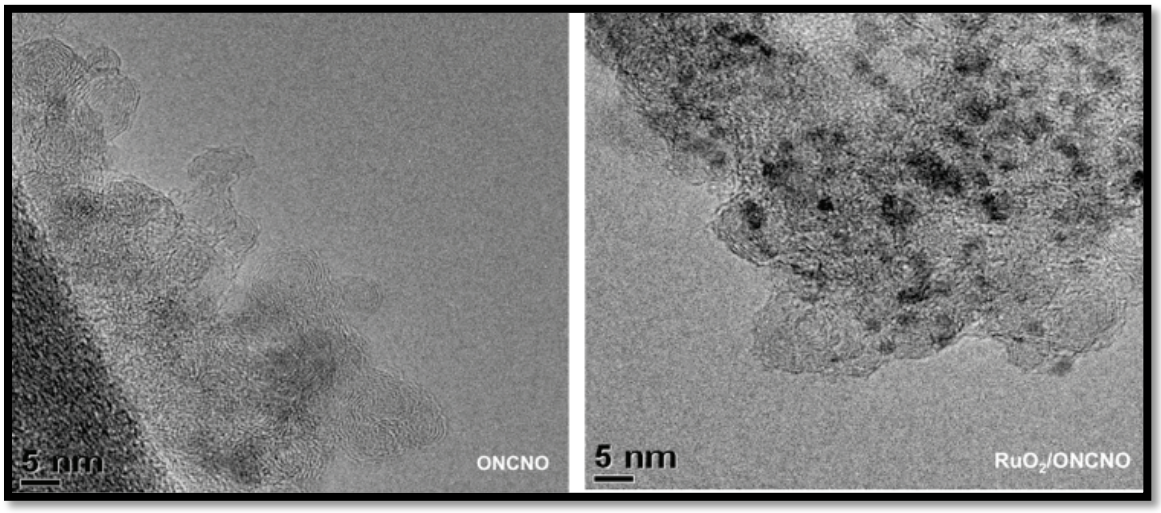

Figure 5.17. HRTEM images of ONCNO and RuO_2•*x*H_2O/ONCNO (67.5 wt% RuO_2)

Cyclic voltammograms of the NCNO, ONCNO and RuO_2•*x*H_2O/ONCNO nanocomposites were recorded at scan rates ranging from 20 mV•s^{-1} to 8 V•s^{-1} in 1.0 M H_2SO_4. **Fig. 5.18a** shows a compilation of CV study of NCNO and ONCNO. The higher specific capacitance of ONCNO is due to the pseudocapacitance of oxygenated groups on the surface. Broad peaks due to the faradic processes of oxygenated groups in ONCNO are observed from 0.2 V to 0.4 V in the voltammogram. These redox reactions of oxygenated groups in carbon particles are well documented.

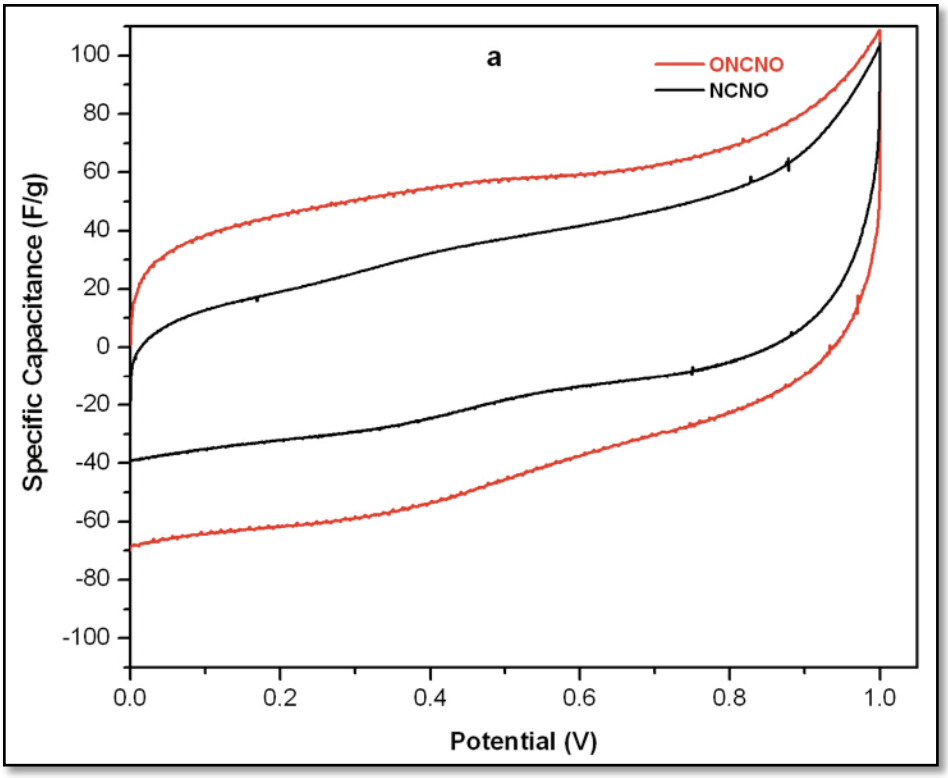

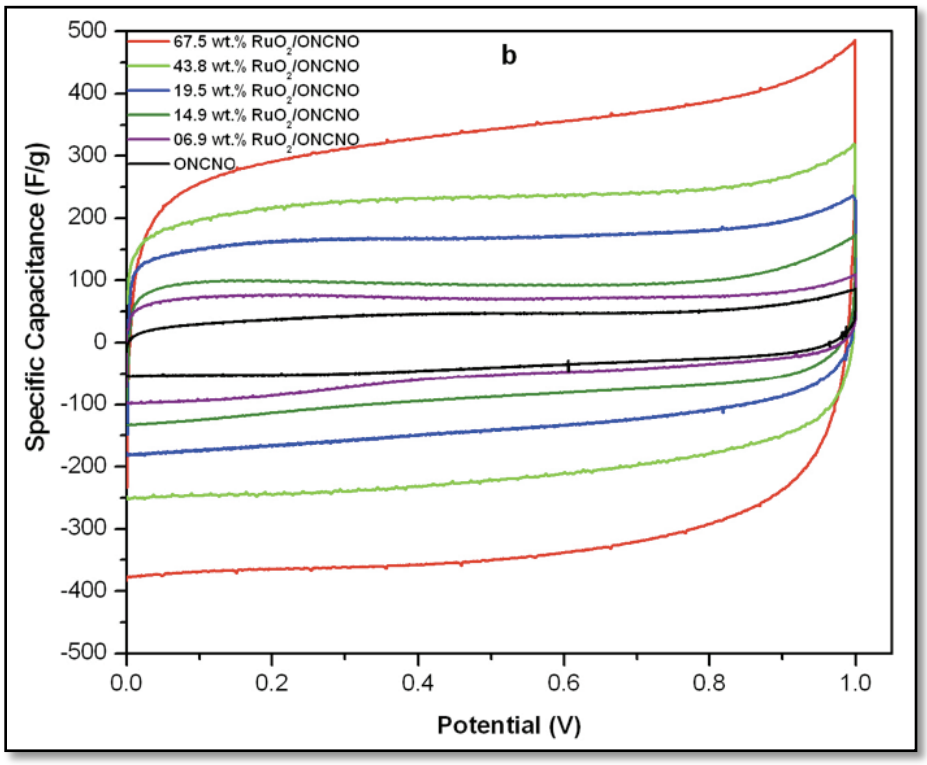

Figure 5.18. Cyclic voltammetry of (a) NCNO and ONCNO (b) $RuO_2 \bullet xH_2O$/ONCNO. The scan rate is 20 $mV \bullet s^{-1}$ in 1.0 M H_2SO_4.

Table 5.4. Specific capacitance NCNO, ONCNO and RuO_2•xH_2O/ONCNO composite electrodes

Sample	Wt% RuO_2	Average specific capacitance (F/g) [a]
NCNO	0	27
ONCNO	0	45
RuO_2/ONCNO	6.9	69
RuO_2/ONCNO	8.3	75
RuO_2/ONCNO	14.9	96
RuO_2/ONCNO	19.5	151
RuO_2/ONCNO	23.5	162
RuO_2/ONCNO	43.8	263
RuO_2/ONCNO	67.5	334

[a]Derived from cyclic voltammetry at a scan rate of 20 mV•s^{-1} in 1.0 M H_2SO

To compare the capacitance behavior of RuO_2•xH_2O/ONCNO composites, voltammograms of several materials at a fixed scan rate of 20 mV•s^{-1} are shown in **Fig. 5.18b**. The cyclic voltammograms of all RuO_2 composites show nearly perfect rectangular shapes, suggesting facile ionic diffusion and excellent electrochemical reversibility of the electrodes under these experimental conditions. The lack of exact symmetry in the CV curves indicates contributions of both double-layer capacitance and pseudocapacitive behavior of RuO_2•xH_2O/ONCNO nanocomposites to the total capacitance. Although the surface area of ONCNO is less than NCNOs, the redox property of surface groups on ONCNOs enhances the capacitance. The concentration of RuO_2 nanoparticles on the surface of NCNOs affects the overall porosity of the electrode for effective ion diffusion and the change in electronic conductivity with change in interparticle contact. As expected, the area under the CV plots increases, although not linearly, with increasing RuO_2 content in the nanocomposites, showing increasing

specific capacitance (Table 5.4). Specific capacitance (C_{sp}) of the single electrode in the symmetric cell was calculated from CV plots according to Equation **5**

The surface properties of ONCNOs make them effective supporting materials for RuO_2 composite electrodes. High capacitance even at higher concentrations of RuO_2 (67.5 wt% RuO_2) indicates that the high surface area and the presence of polar groups on the ONCNOs result in homogeneous distribution of the RuO_2 particles while maintaining mesoporosity of the material for ion diffusion. The polar groups on the surface help to increase hydrophilicity of the composite material, thereby increasing contact between the RuO_2 nanoparticles and aqueous electrolyte. The highly conductive carbon particles also act as an efficient current collector for rapid extraction of electrons from the faradic reaction of $RuO_2 \bullet xH_2O$. Measurement in three-electrode cells differs from two-electrode cells in several aspects. The values of specific capacitance measured from three-electrode cells are found to be approximately double that of a two-electrode system. The high sensitivity of three-electrode configuration can result in overestimation of the electrochemical performance of the composites. The efficiency of an electrode for high-power applications can also be judged from CV analysis at high scan rate. An ideal electrode for the purpose should maintain rectangular CV plots even at faster scan rates. At a very slow scan rate (1–2 mV/s), high specific capacitances are usually observed, that sharply reduce at faster scan rate; however, measuring electrochemical properties at very slow scan rates itself defeats the purpose of a supercapacitor. A minimum scan rate of 20 mV/s is desired for commercial applications. Many of the reported measurements concentrate on achieving high specific capacitance of redox supercapacitors by sacrificing high rate capability and electrochemical stability. During the redox processes in hydrous $RuO_2 \bullet xH_2O$, proton exchange takes place at the electrolyte/electrode interface.

Since this process is relatively slow, higher scan rates lead to either depletion or saturation of ions in the electrolyte inside the electrode pores. This increases the ionic diffusion resistivity, leading to a drop in the capacitance of the porous electrode. In our study, we focused on these factors along with capacitance to prepare electrodes with desirable electrochemical properties.

The ONCNO and $RuO_2 \bullet xH_2O$/ONCNO composites were scanned with sweep rates up to 8 $V \bullet s^{-1}$. Cyclic voltammograms of ONCNOs at various sweep rates (**Fig. 5.19a**) show that even at very high rate (8 V/s) the CVs maintain a nearly ideal rectangular shape. The excellent cyclic property of ONCNO is also maintained in the RuO_2 composites.

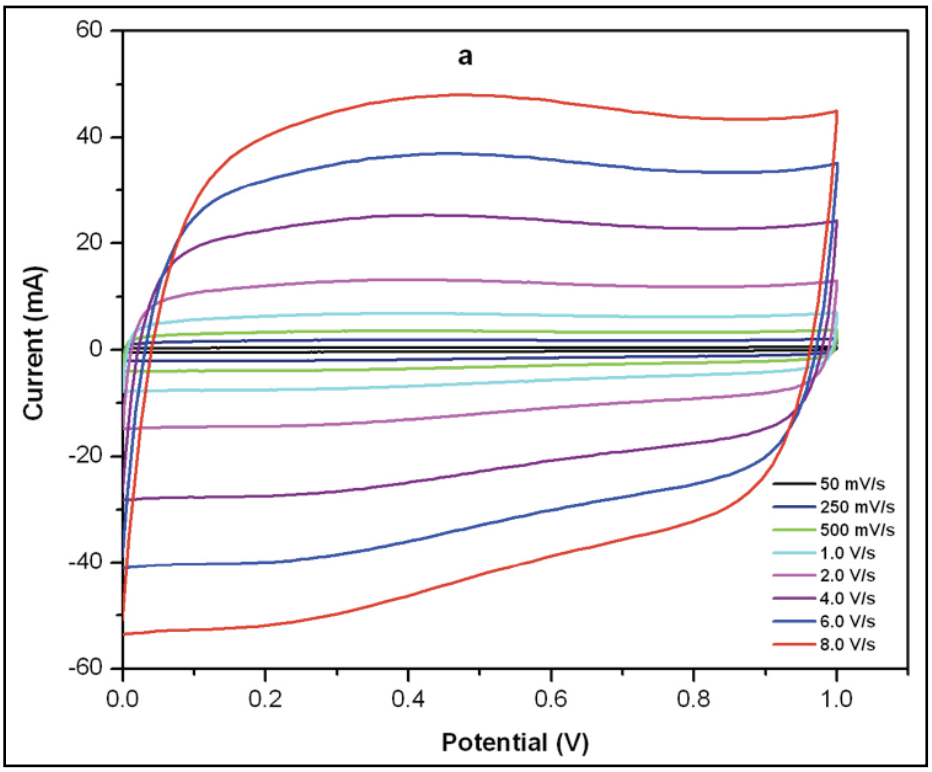

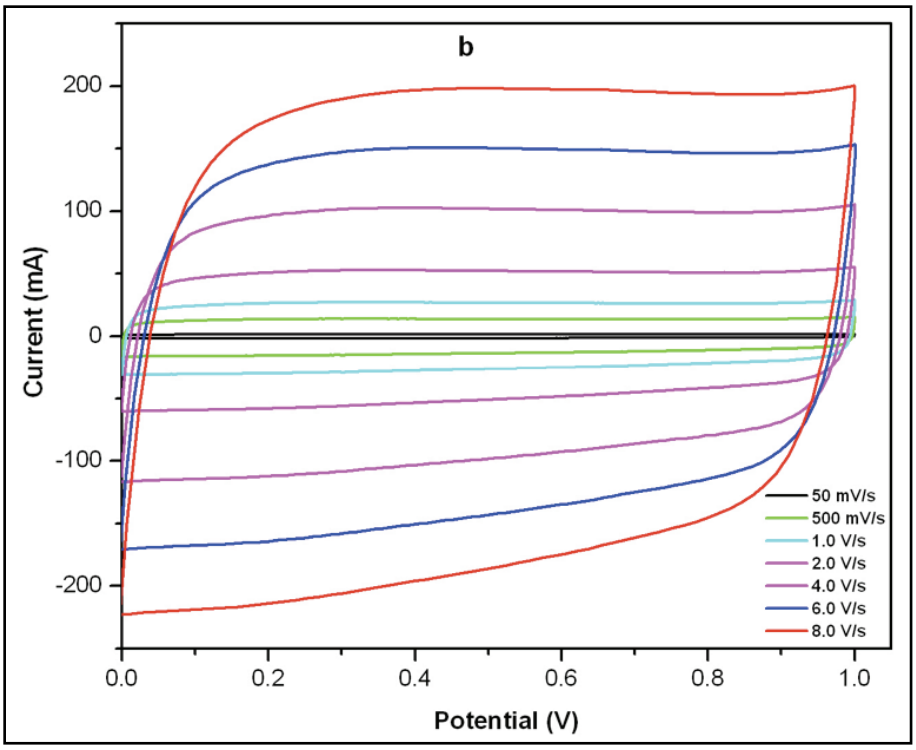

Figure 5.19. Cyclic voltammetry of (a) ONCNO and (b) RuO_2•xH_2O/ONCNO electrode (19.5 wt% RuO_2) at various sweep rates in 1.0 M H_2SO_4

Fig. 5.19b shows the capacitance behavior of RuO_2•xH_2O/ONCNO with 19.5 wt% RuO_2 at various sweep rates. Above 2 V•s^{-1}, only small deviations are observed from the nearly ideal rectangular shape all the way up to 8 V•s^{-1}, indicating low ESR and high power capability of the electrode. This excellent CV behavior of the materials at high sweep rate indicates rapid current response on voltage reversal and nearly ideal porosity of the electrode for electrolyte diffusion.

Fig. 5.20 shows the galvanostatic charge-discharge behavior of RuO_2•xH_2O/ONCNO composite electrodes. The slight curvature in the charge-discharge curve indicates the contribution of pseudocapacitance from RuO_2 to the total capacitance. Small ohmic drop in the discharge curve indicates improved contact between the current collector and the electrode. In the case of ONCNOs, a higher capacitance loss of ~14 % is

observed after 2500 cycles. The pseudocapacitance of acid-oxidized carbon precursors is due to the surface functional groups–acid, phenol, quinone, etc.–undergoing irreversible (pseudoreversible) redox processes at ~0.3–0.45 V vs. SCE in aqueous electrolyte. Other workers have also observed that the loss of some of these chemically oxidized groups upon repeated cycling, resulting in loss of capacitance, is common for carbon nanotubes as well as other high-surface-area carbon precursors. However, the presence of RuO_2 nanoparticles stabilizes the composite, producing very stable cycling behavior (~98% for the RuO_2•xH_2O/ONCNO composites in **Fig. 5.20**). Cheng *et al.* also observed similar behavior for RuO_2-graphene nanocomposites.[95]

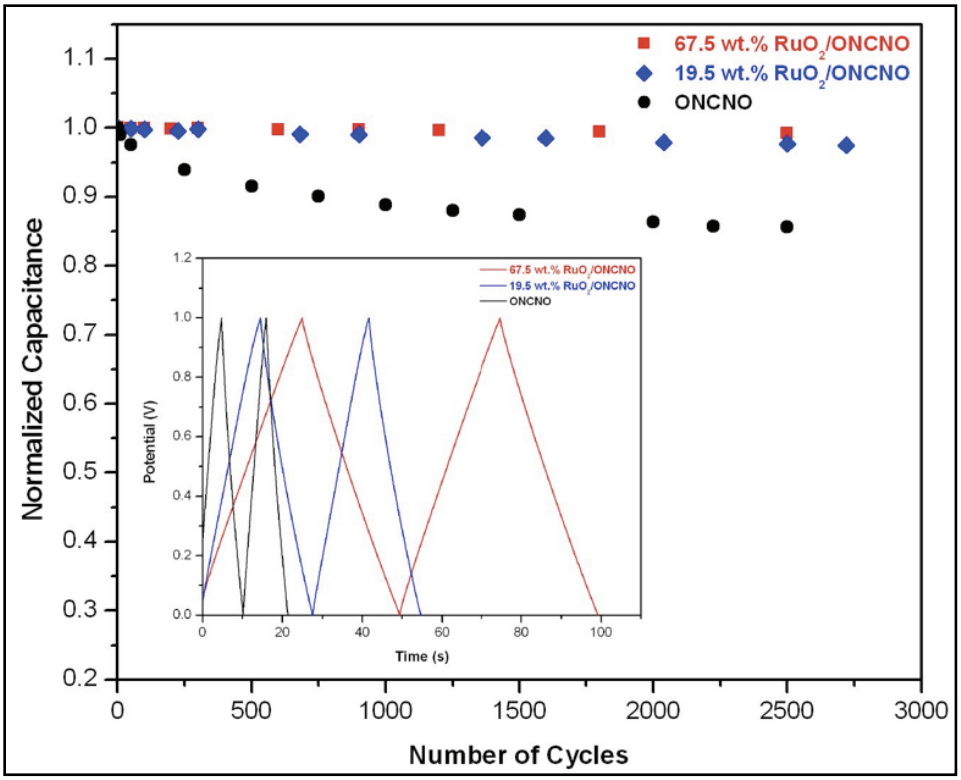

Figure 5.20. Galvanostatic cycling data and (inset) charge-discharge curves for RuO_2•xH_2O/ONCNO electrodes. The charge-discharge current density is 5.0 A/g in 1.0 M H_2SO_4.

EIS experiments were carried out in order to gain insight into the internal resistance and the influence of faradic reactions on the performance of electrode materials. **Fig. 5.21** shows the Nyquist plots of ONCNOs and RuO_2•xH_2O/ONCNO electrodes at two different Ru concentrations. At low frequency the imaginary part of the impedance increases vertically to the y-axis, indicating typical capacitive nature of the electrodes. At high frequency the diameter of the semicircular region of impedance spectra is associated with pseudocapacitance behavior and porous structure of the electrode material.[116]

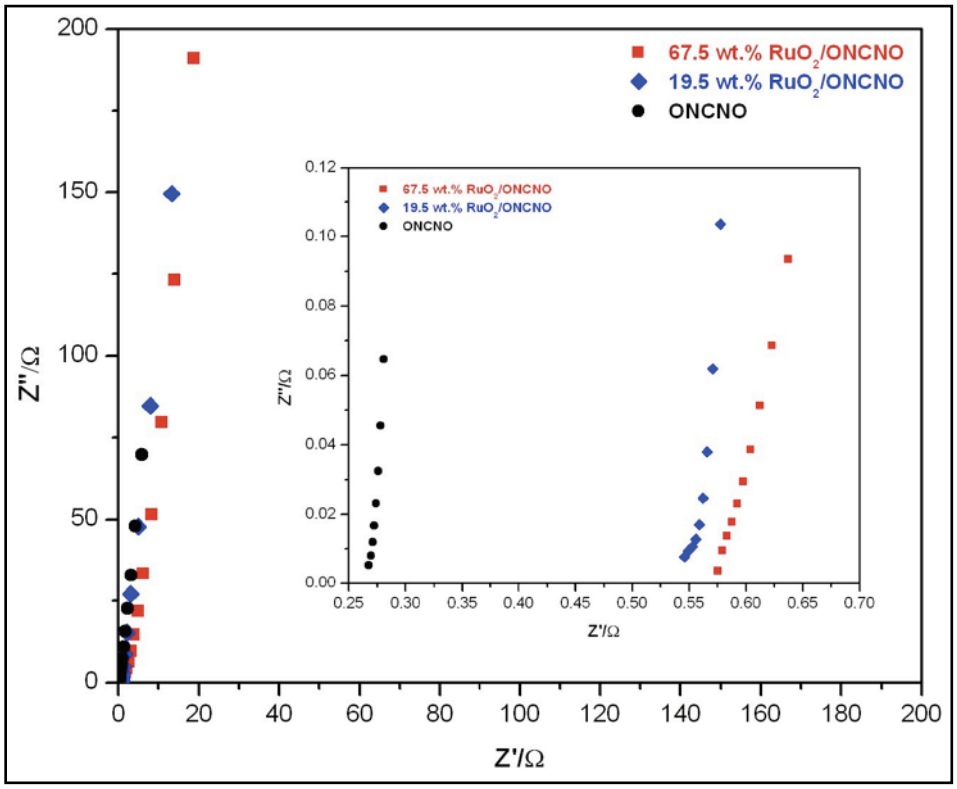

Figure 5.21. Nyquist diagram of ONCNOs and RuO_2•xH_2O/ONCNO electrodes in the frequency range 10 mHz–10 kHz. Insets show enlargements of the high-frequency regions.

The point of intersection with the Z' real axis in this region provides an estimate of the internal resistance of the electrode in terms of equivalent series resistance

(ESR). In the high-frequency region of **Fig. 5.21**, the small diameter of the semicircle indicates nearly ideal capacitive behavior of the electrode. The semicircle at higher frequency slightly increases with Ru loading. However, the semicircular loop at high frequency is too small to identify, indicating fast charge transfer between the metal oxide and the conductive carbon. The semicircular region at an angle of 45º, Warburg resistance, represents the frequency dependence of ionic diffusion into the porous electrode.[117] The short Warburg curves in **Fig. 5.21** indicate short ion diffusion path in the electrodes, facilitating rapid electrolyte access into the electrode surface.[118]

The ESR of ONCNO, 19.5 and 67.5 wt% RuO_2•xH_2O/ONCNO composite electrodes were estimated as 0.268 Ω, 0.558 Ω and 0.585 Ω, respectively. The low ESR value of ONCNOs and RuO_2•xH_2O/ONCNO electrodes is an advantage for high-power supercapacitor applications. The maximum energy density (E_{max}) and maximum power density (P_{max}) of the supercapacitor are calculated from equations **15** and **16**. P_{max} and E_{max} are calculated using the cell voltage of 1.0 V, ESR of 0.585 Ω and 0.558 Ω, and m of 1.76×10^{-3} g and 0.86×10^{-3} g for 67.5 wt% RuO_2/ONCNO and 19.5 wt% RuO_2/ONCNO composite electrodes, respectively. At a maximum power density of 242.8 kW•kg^{-1}, a 67.5 wt% RuO_2•xH_2O/ONCNO electrode can deliver an energy density of 11.6 Wh•kg^{-1}; for 19.5 wt% RuO_2•xH_2O/ONCNO electrode at a maximum power density of 540.3 kW•kg^{-1}, an energy density of 5.2 Wh•kg^{-1} can be achieved. The power densities obtained for RuO_2•xH_2O-modified ONCNO electrodes are significantly higher than other reported RuO_2-impregnated carbon materials and RuO_2 by itself. The high power capability of RuO_2/ONCNO composites could be useful for surge-power delivery.MnO_2/OCNOs

Hydrous oxides of amorphous manganese oxides undergo reversible redox reactions by proton and/or cation exchange with electrolytes, giving large pseudocapacitance. In neutral electrolytic conditions hydrous MnO_2 undergo following chemical changes:[119]

$$MnO_x(H_2O)_y \rightleftharpoons MnO_{(x+\delta)}(H_2O)_{(y-\delta)} + 2\delta H^+ + 2\delta e^-$$

We have utilized the birnessite structure of layered K_xMnO_2 to prepare MnO_2 single sheets via an ion exchange method. The delaminated MnO_2 single sheets carry partial negative charges that are stabilized by TBA ions in solution. Scheme 2 depicts the layer-by-layer approach to prepare the final composite. Initially, NCNOs were functionalized with acidic groups to form a negatively charged surface, which was coated with a thin layer of positively charged PDDA molecules. The PDDA-ONCNO composite possesses a positively charged surface, which further guides the negatively charged MnO_2 nano-sheets to deposit on it. The final MnO_2-PDDA-ONCNO composites, produced via layer by layer deposition, were expected to maximize the exposure of MnO_2 redox-active sites and also, to have a positive synergistic effect of MnO_2 layers with the functionalized CNOs for higher capacity and cycling stability.

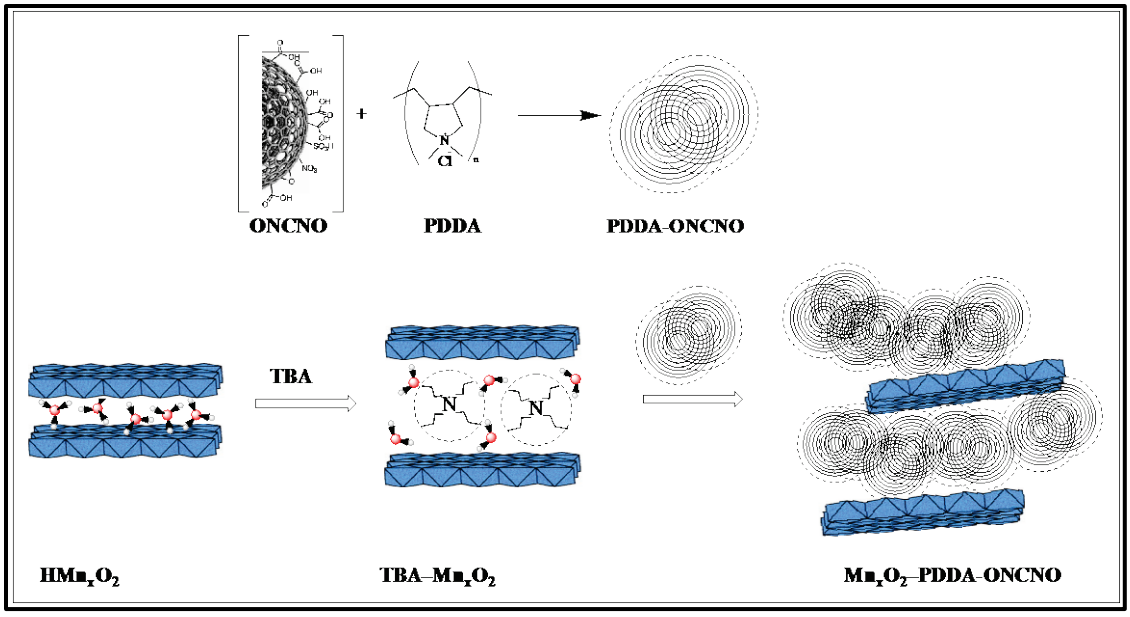

Scheme 5.2. Step by step depiction of the synthesis of MnO2-PDDA-ONCNO composite

The delaminated MnO_2 nano-sheets were examined by XRD analysis. After centrifugation (3500 rpm) of the MnO_2 dispersion, some of the materials are deposited at the bottom of the centrifugation tube, containing highly-separated MnO_2 nano-sheets, while the yellow supernatant solution contains single sheets of MnO_2. As shown in **Fig. 5.22**, XRD of wet samples (before washing with H_2O) indicate highly-separated MnO_2 nano-sheets with an ordered structure while exfoliated MnO_2 sheets (after repeated washing with H_2O) produce broad diffraction peaks with low intensities. These observations are in accordance with other reported results.[108, 109]

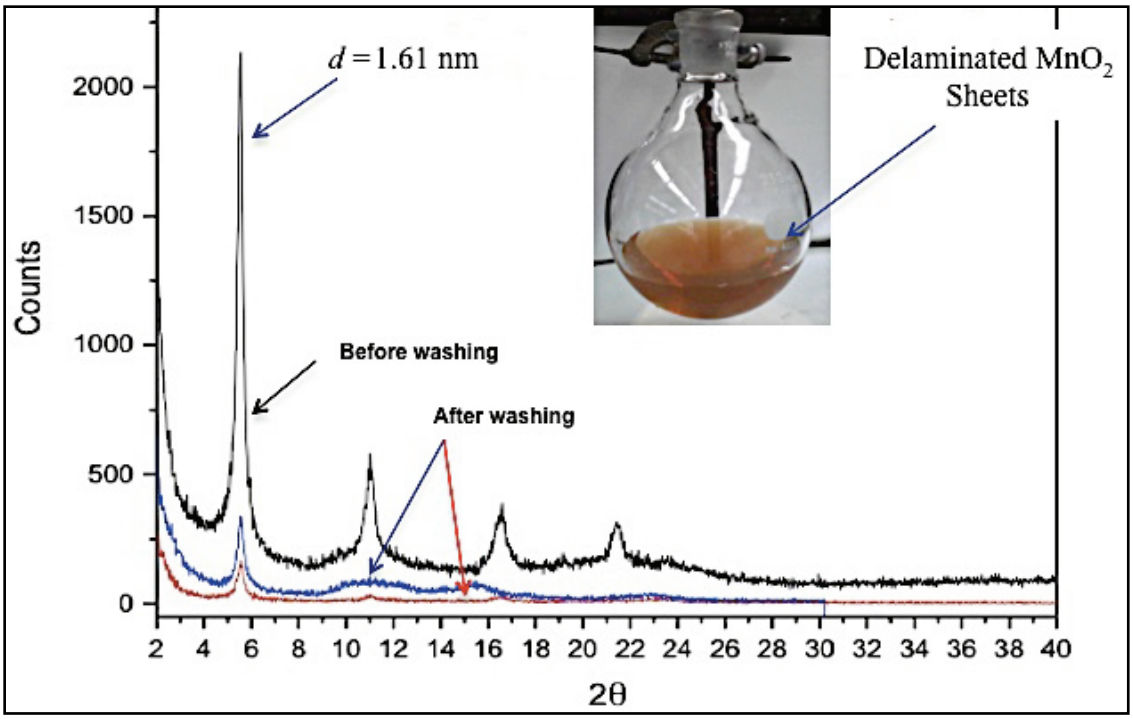

Figure 5.22. XRD of delaminated MnO_2 wet precipitate before and after washing.

It is important to control the thickness of the PDDA layer on ONCNO. A thicker polymer layer can prevent appropriate utilization of high surface area and electric conductivity of the carbon nano-onions, resulting in poor communication with the impregnated MnO_2 nano-sheets. AFM analysis on PDDA–ONCNO is shown in **Fig. 5.23**. The height profile measurements from different spots comprising mono-, bi- and multilayers of PDDA-ONCNO materials indicate an average of ~3 nm PDDA layers homogeneously coated on ONCNOs (6–7 nm). These PDDA–ONCNOs were used for the deposition of delaminated MnO_2 nano-sheets.

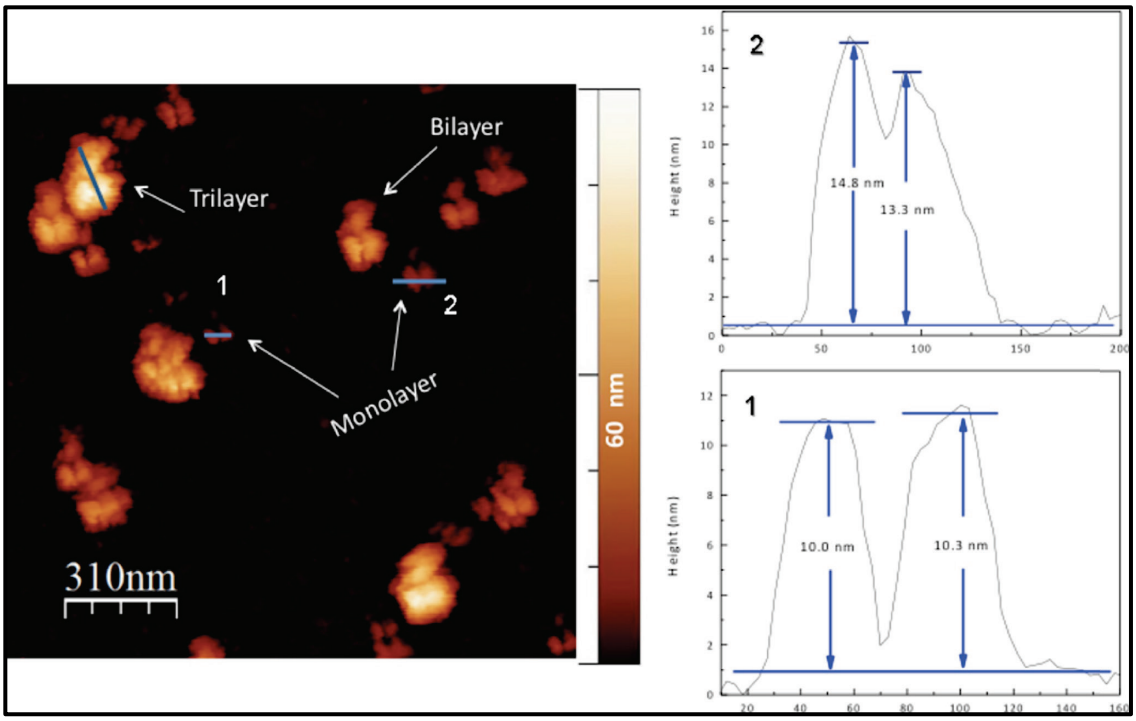

Figure 5.23. AFM analysis of PDDA-ONCNO.

The wt% of MnO_2 in the composites was determined from the TGA combuston residue (**Fig. 5.24**). Above 800 ºC organics and CNOs completely oxidize under air, leaving behind manganese oxides as residue. XRD analysis of the TGA residue shows that the residue is a mixture of Mn_2O_3 (major) and MnO_2.

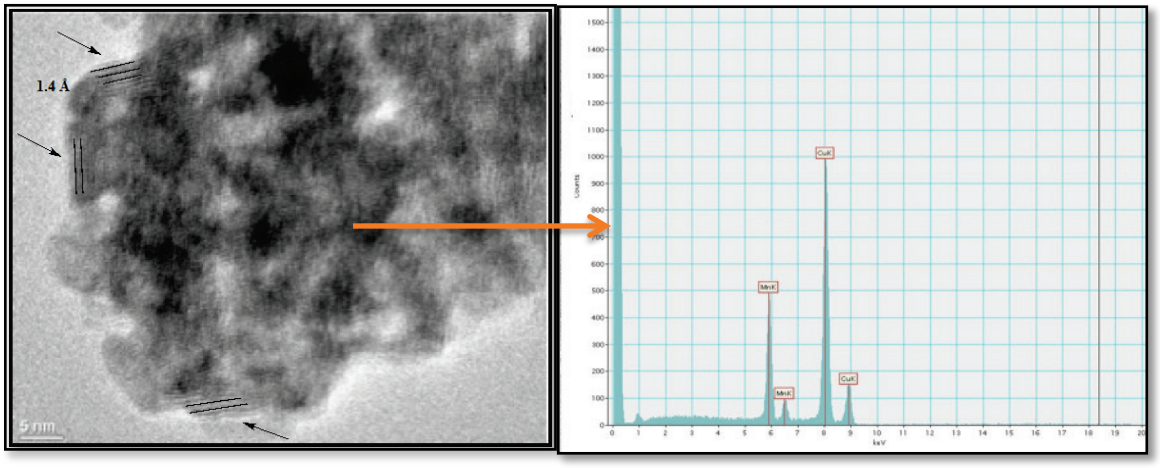

Figure 5.25. HRTEM and EDX analysis of MnO_2-PDDA-ONCNO composite showing amorphous and layered MnO_2 regions

Fig. 5.25 shows the HRTEM image of the MnO_2-PDDA-ONCNO composite (55 wt% MnO_2). Both amorphous and semi-crystalline phases of the delaminated MnO_2 layers were observed. While the presence of the amorphous regions indicate a single layer of MnO_2 deposited on PDDA-ONCNO, in the semi-crystalline phase a *d*-spacing of ~1.4 A indicates re-aggregation of MnO_2 nanosheets. The re-aggregation of delaminated MnO_2 layers upon drying is also reported by other groups.

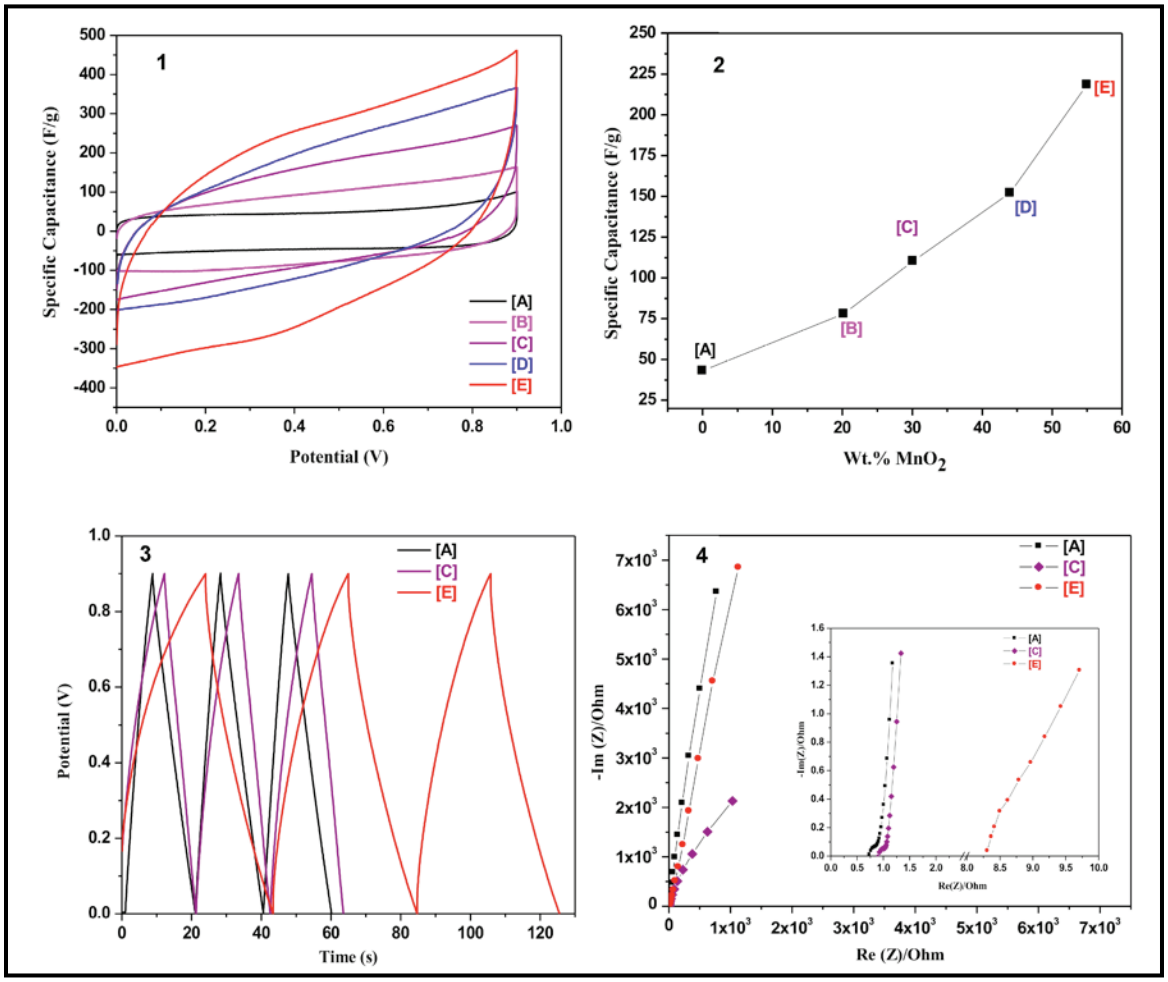

Figure 5.26. (1) Cyclic voltammetry **(2)** plot of wt% MnO2 vs. Specific capacitance (F/g) **(3)** Galvanostatic charge discharge **(3)** Impedance spectra of composites

The specific capacitance of the symmetric cell is determined by integrating the area under the cyclic voltammetry curve using **Equation 5**. Significantly, this capacitance was obtained from a two-electrode cell. While three-electrode cells usually overestimate the capacitance, two-electrode configurations give good agreement with industrial cells. The CV of the PDDA-ONCNO composite has a nearly ideal rectangular shape with a specific capacitance of 43 F/g. Cyclic voltammetry studies of composites containing varying concentrations of MnO_2 are plotted in **Fig. 5.26.2**. With increasing MnO_2 concentration, capacitance increases linearly with a maximum value of 218.6 F/g for 55 wt% MnO_2.

To compare the performance of composites with different wt% of MnO_2, a scan rate of 5 mV/s was used. As the scan rate increases, the capacitance drops rapidly. A thin, single layer of delaminated MnO_2 on conductive carbon was expected to overcome the inherent low conductivity of MnO_2 layers. However, as observed from the HRTEM (**Fig. 5.25**), MnO_2 layers re-aggregate upon drying, which lowers the conductivity and increases the ESR of the resultant materials. This is also reflected in the CV plots (**Fig. 5.26.1**) and the impedance spectra (**Fig. 5.26.4**) of the composites, which become more resistive with increasing MnO_2 concentration. Moreover, after the electrochemical measurements a thin brown ring on the Celgard separator was observed, which is due to the partial dissolution of MnO_2. At typical applied polarization potentials, MnO_2 is irreversibly oxidized to soluble Mn(VII) at the positive electrode and irreducibly reduced to soluble Mn(II) at the negative electrode in neutral electrolyte, as reported by other researchers.[119] We suggest that the interaction of the positively charged PDDA-ONCNO surface with the negatively charged MnO_2 layers stabilizes the composite. In the MnO_2-PDDA-ONCNO composites, the re-aggregated MnO_2 nano-sheets may have weaker

interaction with the positively charged PDDA-ONCNO surface. As the number of MnO_2 layers increases, the outermost MnO_2 layers that are not directly in contact with the positively charged PDDA-ONCNO are most likely to dissolve readily. At lower concentration of MnO_2, when the re-aggregation is limited, the materials exhibit lower capacitance but no noticeable brown rings were observed after electrochemical measurements, The rings became prominent for higher concentrations of MnO_2 in the composite (**Fig. 5.27**).

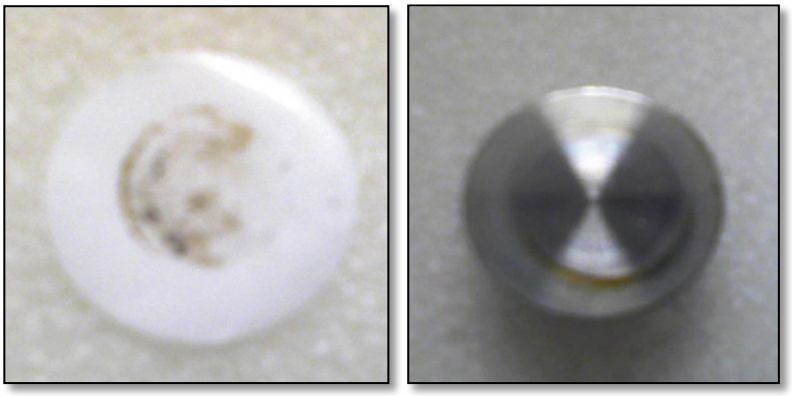

Figure 5.27. Formation of brown ring on the Celgard separator and the stainless steel Swagelok cell.

Other metal oxides/CNO composites

Preliminary studies on NiO_2/ONCNO and TiO_2/ONCNO composites prepared via precipitation of metal oxides from chloride precursors were performed. The specific capacitance values obtained from CV analysis for NiO_2 (TGA residue 27 %, 3 ED cell, dV/dt =20 mVS^{-1} , 1.0 M H_2SO_4 , C_{sp} = 55 F/g) and TiO_2 (TGA residue 27 %, 3 ED cell, dV/dt =20 mVS^{-1} , 1.0 M H_2SO_4 , C_{sp} = 10–15 F/g) were much lower than RuO_2 and MnO_2 composites having similar metal oxide content. Further study on NiO_2, TiO_2 is required to optimize the charge-storage capacity of these metal oxide/CNO composites .

5.6. Summary

In summary, we have exploited surface properties, both physical and chemical, of CNOs to use them as electrode materials for supercapacitor applications. In these EDLC studies, we preferred NCNO to ACNOs due to their easier preparation, higher purity and higher surface area. We functionalized the surface of NCNOs by chemical oxidation and synthesized metal oxide/ONCNO composite electrodes by controlled chemical precipitation and by layer-by-layer deposition. Under our synthetic conditions, the high surface area of NCNOs is effective for homogeneous impregnation of metal oxides, maintaining mesoporosity of the electrode for ion diffusion. Both ONCNO and $RuO_2 \bullet xH_2O$/ONCNO electrodes have excellent electrochemical reversibility, maintaining supercapacitive behavior even at high potential sweep rates, indicating low ESR and high power capability. Along with high specific capacitance we have significantly enhanced the cyclic stability and power density of the $RuO_2 \bullet xH_2O$/ONCNO composites by utilizing a carbon nano-onion support and by controlling the size of deposited metal oxide nanoparticles even at high concentration. In case of MnO_2-PDDA-ONCNO composites, although high-capacitance was achieved with 55 wt% MnO_2 loading, the cycling stability is still an issue. Both NCNOs and chemically modified NCNOs have good electrical conductivity, ideal mesoporosity for ion transport, and high electrochemical and thermal stability. Moreover, unlike other amorphous carbon sources, the sp^2–C network of NCNOs can enhance the charge transfer processes in metal oxide redox supercapacitors. Therefore, NCNOs/ONCNOs are a very competitive carbon support for supercapacitor composite electrodes, which can be prepared easily and cost-effectively in bulk quantities.

Chapter VI: Conclusions and Future Prospects of the Study

In this study synthesis, purification and surface properties of the carbon nano-onions were emphasized. Two types of CNOs, A-CNOs and N-CNOs, were considered for physicochemical modifications and to compare their surface properties in terms of surface area, conductivity, porosity, microstructure and chemical reactivity. N-CNOs were particluarly used for electrode materials in supercapacitor applications.

Various important properties of CNOs and their possible chemical surface modifications were realized. These new findings are very important for future development of composite materials, biomedical applications, electrode materials for energy storage, and also for the fundamental study of suface properties.

The newly desigened arc-discharge apparatus is very convenient for controlled synthesis of A-CNOs. The control over the arc plasma, power supplied, duty cycle and temperature of the surrounding water resulted in fewer impurities and narrower distribution of A-CNOs. Under our experimental conditions, an arc power of 825 W, 30% duty cycle, temperature below 60 ºC, and N_2 purging to avoid electrical contacts with surrounding water produces best quality of A-CNO samples.

Purification of carbon materials has always been a challenge in the area of carbon nanoparticle research. However, purification is essential for both fundamental property studies and materials development. We have developed a very efficient purification method based on distinctive physical and chemical properties of A-CNOs compared to other carbonaceous impurities. Polyoxometalate (POM) was used as a screening agent for

A-CNOs, and subsequent removal of POM molecules from A-CNO surfaces gives highly pure samples.

To study the fundamental surface chemical properties of CNOs and to incorporate CNOs in various composite materials, many different types of chemical functionalization were performed. These chemical functionalization include Billups reductive alkylation, Sandmeyer reaction, 1,3-cycloaddition, and oleum-assisted functionalization. A detailed analysis was done to quantify the functional groups and to compare reactivity difference between A-CNOs and N-CNOs. Smaller N-CNOs were found to be more reactive and were easily dispersible in various solvents depending on the surface functional group.

Due to higher purity, easier synthesis and higher surface area of NCNOs compared to A-CNOs, we have mostly focused on N-CNOs to use as electrode materials for supercapacitor study. The hydrophilicity of the carbon particles was tuned via. chemical functionalization for aquous electrolyte. Moreover, various metal oxides such as RuO_2, MnO_2, TiO, NiO were successfully impregnated on the surface of CNOs to enhance capacitance of the materials. We found that both N-CNOs and metal oxide impregnated N-CNOs can be modified for highly efficient electrode materials for supercapacitor applications.

The studies on CNOs reported in this dissertation have many future prospects. The well-characterized and purified A-CNOs can now be used for various applications such as catalyst supports, electrochemical sensors, capacitors and battery electrodes. A combined study with Dr. Kim at the Deparment of Chemistry, University of Kentucky on purified A-CNOs showed enhanced electrochemical sensing for biomolecules.

To develop cost effective and high performance supercapacitor electrodes, efficient methods of preparation can be developed to impregnate MnO_2 on the surface of N-CNOs. Our study on a MnO_2-N-CNOs composite results in higher capacitance but limited cycling stability. To enhance the cycling performance, electrochemical deposition of MnO_2 on N-CNOs (previously coated on Au current collector) can be performed as depicted in the figure below.

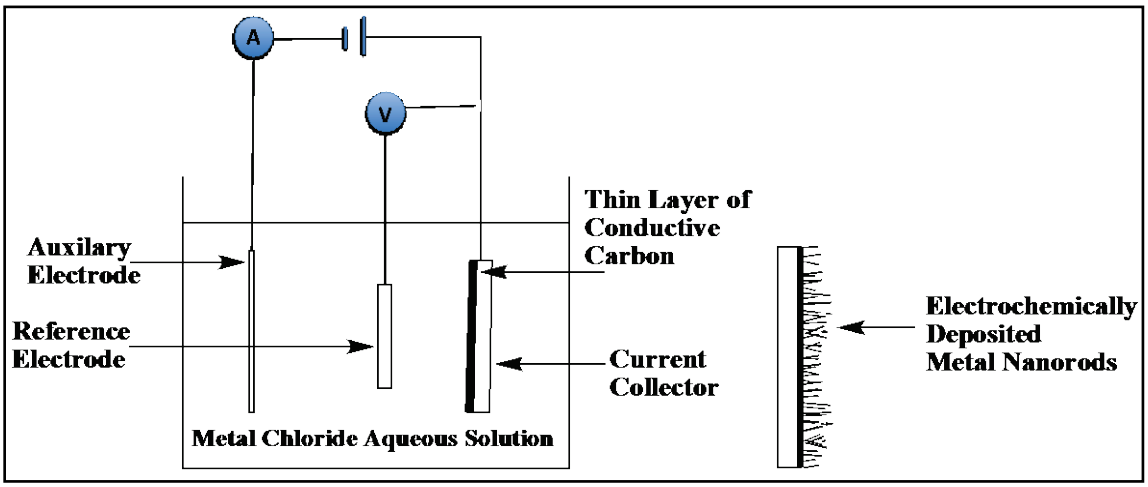

Figure 6.1. A proposed electrochemical deposition of metal oxide nanorods on CNOs. Similar studies can be done with other potential metal oxides for high-performance supercapacitor electrodes.

The A-CNOs study revealed that heteroatom doping (e.g. B, S, N and P) can be done into the hollow core (~10 nm) of A-CNOs to make physicochemical changes in the sp^2-carbon network that will significantly changenot only the physical properties (hardness and electrical conductivity), but also the chemical reactivity. For example, B_4C@A-CNOs with the high neutron cross-section of ^{10}B can be used as radiation shielding in spacecraft and reactivity controlled material in nuclear reactors.

References

1. Balzani, V.; Gomez-Lopez, M.; Stoddart, J. F., Molecular Machines. *Acc. Chem. Res.* **1998,** 31, 405-414.
2. Kroto, H. W.; Heath, J. R.; O'Brien, S. C.; Curl, R. F.; Smalley, R. E., C60: Buckminsterfullerene. *Nature* **1985,** 318, 162-163.
3. Kratschmer, W.; Lamb, L. D.; Fostiropoulos, K.; Huffman, D. R., Solid C60: a new form of carbon. *Nature* **1990,** 347, 354-358.
4. Schmalz, T. G.; Seitz, W. A.; Klein, D. J.; Hite, G. E., Elemental carbon cages. *J. Am. Chem. Soc.* **1988,** 110, 1113-1127.
5. Zuo, T.; Beavers, C. M.; Duchamp, J. C.; Campbell, A.; Dorn, H. C.; Olmstead, M. M.; Balch, A. L., Isolation and Structural Characterization of a Family of Endohedral Fullerenes Including the Large, Chiral Cage Fullerenes Tb3N@C88 and Tb3N@C86 as well as the Ih and D5h Isomers of Tb3N@C80. *J. Am. Chem. Soc.* **2007,** 129, 2035-2043.
6. Schwarz, H., The Mechanism of Fullerence Formation. *Angew. Chem. Int. Ed. Engl.* **1993,** 32, 1412-1415.
7. Ruoff, R. S.; Tse, D. S.; Malhotra, R.; Lorents, D. C., Solubility of fullerene (C60) in a variety of solvents. *J. Phys. Chem.* **1993,** 97, 3379-3383.
8. Sivaraman, N.; Dhamodaran, R.; Kaliappan, I.; Srinivasan, T. G.; Rao, P. R. V.; Mathews, C. K., Solubility of C60 in organic solvents. *J. Org. Chem.* **1992,** 57, 6077-6079.
9. Nakamura, Y.; Suzuki, M.; Imai, Y.; Nishimura, J., Synthesis of [60]Fullerene Adducts Bearing Carbazole Moieties by Bingel Reaction and Their Properties. *Org. Lett.* **2004,** 6, 2797-2799.
10. Iwashita, A.; Matsuo, Y.; Nakamura, E., AlCl3-Mediated Mono-, Di-, and Trihydroarylation of [60]Fullerene. *Angew. Chem. Int. Ed.* **2007,** 46, 3513-3516.
11. Jia, J.; Wu, H.-S.; Xu, X.-H.; Zhang, X.-M.; Jiao, H., Fused Five-Membered Rings Determine the Stability of C60F60. *J. Am. Chem. Soc.* **2008,** 130, 3985-3988.
12. Iijima, S.; Ichihashi, T., Single-shell carbon nanotubes of 1-nm diameter. *Nature* **1993,** 363, 603-605.
13. Bethune, D. S.; Klang, C. H.; de Vries, M. S.; Gorman, G.; Savoy, R.; Vazquez, J.; Beyers, R., Cobalt-catalysed growth of carbon nanotubes with single-atomic-layer walls. *Nature* **1993,** 363, 605-607.
14. Odom, T. W.; Huang, J.-L.; Kim, P.; Lieber, C. M., Structure and Electronic Properties of Carbon Nanotubes. *J. Phys. Chem. B* **2000,** 104, 2794-2809.
15. Journet, C.; Maser, W. K.; Bernier, P.; Loiseau, A.; de la Chapelle, M. L.; Lefrant, S.; Deniard, P.; Lee, R.; Fischer, J. E., Large-scale production of single-walled carbon nanotubes by the electric-arc technique. *Nature* **1997,** 388, 756-758.
16. Chen, C.; Chen, W.; Zhang, Y., Synthesis of carbon nano-tubes by pulsed laser ablation at normal pressure in metal nano-sol. *Physica E: Low-dimensional Systems and Nanostructures* **2005,** 28, 121-127.
17. Dai, H., Carbon Nanotubes: Synthesis, Integration, and Properties. *Acc. Chem. Res.* **2002,** 35, 1035-1044.

18. Ugarte, D., Curling and closure of graphitic networks under electron-beam irradiation. *Nature* **1992,** 359, 707-709.
19. Banhart, F.; Füller, T.; Redlich, P.; Ajayan, P. M., The formation, annealing and self-compression of carbon onions under electron irradiation. *Chem. Phys. Lett.* **1997,** 269, 349-355.
20. Thune, E.; Cabioc'h, T.; GuÈrin, P.; Denanot, M. F.; Jaouen, M., Nucleation and growth of carbon onions synthesized by ion-implantation: a transmission electron microscopy study. *Mater. Lett.* **2002,** 54, 222-228.
21. Hou, S.-S.; Chung, D.-H.; Lin, T.-H., High-yield synthesis of carbon nano-onions in counterflow diffusion flames. *Carbon* **2009,** 47, 938-947.
22. He, C.; Zhao, N.; Du, X.; Shi, C.; Ding, J.; Li, J.; Li, Y., Low-temperature synthesis of carbon onions by chemical vapor deposition using a nickel catalyst supported on aluminum. *Scripta Mater.* **2006,** 54, 689-693.
23. Chen, X. H.; Deng, F. M.; Wang, J. X.; Yang, H. S.; Wu, G. T.; Zhang, X. B.; Peng, J. C.; Li, W. Z., New method of carbon onion growth by radio-frequency plasma-enhanced chemical vapor deposition. *Chem. Phys. Lett.* **2001,** 336, 201-204.
24. Kuznetsov, V. L.; Chuvilin, A. L.; Butenko, Y. V.; Mal'kov, I. Y.; Titov, V. M., Onion-like carbon from ultra-disperse diamond. *Chem. Phys. Lett.* **1994,** 222, 343-348.
25. Zou, Q.; Wang, M.; Li, Y.; Zhao, Y.; Zou, L., Fabrication of onion-like carbon from nanodiamond by annealing. *Science in China, Series E: Technological Sciences* **2009,** 52, 3683-3689.
26. Gubarevich, A. V.; Kitamura, J.; Usuba, S.; Yokoi, H.; Kakudate, Y.; Odawara, O., Onion-like carbon deposition by plasma spraying of nanodiamonds. *Carbon* **2003,** 41, 2601-2606.
27. Sano, N.; Wang, H.; Alexandrou, I.; Chhowalla, M.; Teo, K. B. K.; Amaratunga, G. A. J.; Iimura, K., Properties of carbon onions produced by an arc discharge in water. *J. Appl. Phys.* **2002,** 92, 2783-2788.
28. Thune, E.; Cabioc'h, T.; Jaouen, M.; Bodart, F., Nucleation and growth of carbon onions synthesized by ion implantation at high temperatures. *Phys. Rev. B* **2003,** 68, 115434.
29. Xu, B.-s., Prospects and research progress in nano onion-like fullerenes. *New Carbon Materials* **2008,** 23, 289-301.
30. Sano, N.; Wang, H.; Chhowalla, M.; Alexandrou, I.; Amaratunga, G. A. J., Nanotechnology: Synthesis of carbon 'onions' in water. *Nature* **2001,** 414, 506-507.
31. Lange, H.; Sioda, M.; Huczko, A.; Zhu, Y. Q.; Kroto, H. W.; Walton, D. R. M., Nanocarbon production by arc discharge in water. *Carbon* **2003,** 41, 1617-1623.
32. Wang, X. K.; Lin, X. W.; Dravid, V. P.; Ketterson, J. B.; Chang, R. P. H., Carbon nanotubes synthesized in a hydrogen arc discharge. *Appl. Phys. Lett.* **1995,** 66, 2430-2432.
33. Rettenbacher, A. S.; Elliott, B.; Hudson, J. S.; Amirkhanian, A.; Echegoyen, L., Preparation and Functionalization of Multilayer Fullerenes (Carbon Nano-Onions). *Chem. Eur. J.* **2006,** 12, 376-387.

34. Koudoumas, E.; Kokkinaki, O.; Konstantaki, M.; Couris, S.; Korovin, S.; Detkov, P.; Kuznetsov, V.; Pimenov, S.; Pustovoi, V., Onion-like carbon and diamond nanoparticles for optical limiting. *Chem. Phys. Lett.* **2002,** 357, 336-340.
35. Keller, N.; Maksimova, N. I.; Roddatis, V. V.; Schur, M.; Mestl, G.; Butenko, Y. V.; Kuznetsov, V. L.; Schlögl, R., The Catalytic Use of Onion-Like Carbon Materials for Styrene Synthesis by Oxidative Dehydrogenation of Ethylbenzene. *Angew. Chem. Int. Ed.* **2002,** 41, 1885-1888.
36. Park, S.; Lian, K.; Gogotsi, Y., Pseudocapacitive Behavior of Carbon Nanoparticles Modified by Phosphomolybdic Acid. *J. Electrochem. Soc.* **2009,** 156, A921-A926.
37. Palkar, A.; Kumbhar, A.; Athans, A. J.; Echegoyen, L., Pyridyl-Functionalized and Water-Soluble Carbon Nano Onions: First Supramolecular Complexes of Carbon Nano Onions. *Chem. Mater.* **2008,** 20, 1685-1687.
38. Hirata, A.; Igarashi, M.; Kaito, T., Study on solid lubricant properties of carbon onions produced by heat treatment of diamond clusters or particles. *Tribo. Int.* **2004,** 37, 899-905.
39. Craddock, J. D. Production, functionalization, modification and characterization of carbon nano-onions and multi-walled carbon nanotubes. University of Kentucky, Lexington, 2008.
40. Tai, F. C.; Wei, C.; Chang, S. H.; Chen, W. S., Raman and X-ray diffraction analysis on unburned carbon powder refined from fly ash. *J. Raman Spectrosc.* **2010,** 41, 933-937.
41. Zickler, G. A.; Smarsly, B.; Gierlinger, N.; Peterlik, H.; Paris, O., A reconsideration of the relationship between the crystallite size La of carbons determined by X-ray diffraction and Raman spectroscopy. *Carbon* **2006,** 44, 3239-3246.
42. Tzeng, S.-S., Catalytic graphitization of electroless Ni-P coated PAN-based carbon fibers. *Carbon* **2006,** 44, 1986-1993.
43. Faugeras, C.; Nerriere, A.; Potemski, M.; Mahmood, A.; Dujardin, E.; Berger, C.; de Heer, W. A., Few-layer graphene on SiC, pyrolitic graphite, and graphene: A Raman scattering study. *Appl. Phys. Lett.* **2008,** 92, 011914-3.
44. Hayashi, T.; Shimamoto, D.; Kim, Y. A.; Muramatsu, H.; Okino, F.; Touhara, H.; Shimada, T.; Miyauchi, Y.; Maruyama, S.; Terrones, M.; Dresselhaus, M. S.; Endo, M., Selective Optical Property Modification of Double-Walled Carbon Nanotubes by Fluorination. *ACS Nano* **2008,** 2, 485-488.
45. Chang, H.; Bard, A. J., Scanning tunneling microscopy studies of carbon-oxygen reactions on highly oriented pyrolytic graphite. *J. Am. Chem. Soc.* **1991,** 113, 5588-5596.
46. Morishita, K.; Takarada, T., Scanning electron microscope observation of the purification behaviour of carbon nanotubes. *J. Mater. Sci.* **1999,** 34, 1169-1174.
47. Ebbesen T.W., A. P. M., Hiura H., Tanigaki K. , Purification of nanotubes. *Nature* **1994,** 367, 519–9.
48. An, K. H.; Kim, W. S.; Park, Y. S.; Moon, J.-M.; Bae, D. J.; Lim, S. C.; Lee, Y. S.; Lee, Y. H., Electrochemical Properties of High-Power Supercapacitors Using Single-Walled Carbon Nanotube Electrodes. *Adv. Funct. Mater.* **2001,** 11, 387-392.

49. Zhang, J.; Zou, H.; Qing, Q.; Yang, Y.; Li, Q.; Liu, Z.; Guo, X.; Du, Z., Effect of Chemical Oxidation on the Structure of Single-Walled Carbon Nanotubes. *J. Phys. Chem. B* **2003,** 107, 3712-3718.
50. Hou, P. X.; Bai, S.; Yang, Q. H.; Liu, C.; Cheng, H. M., Multi-step purification of carbon nanotubes. *Carbon* **2002,** 40, 81-85.
51. Hu, H.; Zhao, B.; Itkis, M. E.; Haddon, R. C., Nitric Acid Purification of Single-Walled Carbon Nanotubes. *J. Phys. Chem. B* **2003,** 107, 13838-13842.
52. Bauer, B. J.; Becker, M. L.; Bajpai, V.; Fagan, J. A.; Hobbie, E. K.; Migler, K.; Guttman, C. M.; Blair, W. R., Measurement of Single-Wall Nanotube Dispersion by Size Exclusion Chromatography. *J. Phys. Chem. C* **2007,** 111, 17914-17918.
53. Doorn, S. K.; Strano, M. S.; O'Connell, M. J.; Haroz, E. H.; Rialon, K. L.; Hauge, R. H.; Smalley, R. E., Capillary Electrophoresis Separations of Bundled and Individual Carbon Nanotubes. *J. Phys. Chem. B* **2003,** 107, 6063-6069.
54. Chun, J.; Fagan, J. A.; Hobbie, E. K.; Bauer, B. J., Size Separation of Single-Wall Carbon Nanotubes by Flow-Field Flow Fractionation. *Anal. Chem.* **2008,** 80, 2514-2523.
55. Andrews, R.; Jacques, D.; Qian, D.; Dickey, E. C., Purification and structural annealing of multiwalled carbon nanotubes at graphitization temperatures. *Carbon* **2001,** 39, 1681-1687.
56. Fei, B.; Lu, H.; Chen, W.; Xin, J. H., Ionic peapods from carbon nanotubes and phosphotungstic acid. *Carbon* **2006,** 44, 2261-2264.
57. Liu, J.; Rinzler, A. G.; Dai, H.; Hafner, J. H.; Bradley, R. K.; Boul, P. J.; Lu, A.; Iverson, T.; Shelimov, K.; Huffman, C. B.; Rodriguez-Macias, F.; Shon, Y.-S.; Lee, T. R.; Colbert, D. T.; Smalley, R. E., Fullerene Pipes. *Science* **1998,** 280, 1253-1256.
58. Fei, B.; Lu, H.; Hu, Z.; Xin, J. H., Solubilization, purification and functionalization of carbon nanotubes using polyoxometalate. *Nanotechnology* **2006**, 1589-1593.
59. Newman, A. D.; Brown, D. R.; Siril, P.; Lee, A. F.; Wilson, K., Structural studies of high dispersion H3PW12O40/SiO2 solid acid catalysts. *PCCP* **2006,** 8, 2893-2902.
60. Hodnett, B. K.; Moffat, J. B., Application of temperature-programmed desorption to the study of heteropoly compounds: Desorption of water and pyridine. *J. Catal.* **1984,** 88, 253-263.
61. Schwegler, M. A.; Vinke, P.; van der Eijk, M.; van Bekkum, H., Activated carbon as a support for heteropolyanion catalysts. *Appl. Catal., A* **1992,** 80, 41-57.
62. Gall, R. D.; Hill, C. L.; Walker, J. E., Carbon Powder and Fiber-Supported Polyoxometalate Catalytic Materials. Preparation, Characterization, and Catalytic Oxidation of Dialkyl Sulfides as Mustard (HD) Analogues. *Chem. Mater.* **1996,** 8, 2523-2527.
63. Gupta, S.; Saxena, A., Nanocarbon materials: probing the curvature and topology effects using phonon spectra. *J. Raman Spectrosc.* **2009,** 40, 1127-1137.
64. Sun, Y.-P.; Fu, K.; Lin, Y.; Huang, W., Functionalized Carbon Nanotubes: Properties and Applications. *Acc. Chem. Res.* **2002,** 35, 1096-1104.
65. Fu, K.; Huang, W.; Lin, Y.; Zhang, D.; Hanks, T. W.; Rao, A. M.; Suna, Y.-P., Functionalization of Carbon Nanotubes with Bovine Serum Albumin in Homogeneous Aqueous Solution. *J. Nanosci. Nanotechnol.* **2002,** 2, 457-461.

66. Chen, Z.; Kobashi, K.; Rauwald, U.; Booker, R.; Fan, H.; Hwang, W.-F.; Tour, J. M., Soluble Ultra-Short Single-Walled Carbon Nanotubes. *J. Am. Chem. Soc.* **2006,** 128, 10568-10571.
67. Yang, M.; Koutsos, V.; Zaiser, M., Interactions between Polymers and Carbon Nanotubes: A Molecular Dynamics Study. *J. Phys. Chem. B* **2005,** 109, 10009-10014.
68. Hirsch, A., Functionalization of Single-Walled Carbon Nanotubes. *Angew. Chem. Int. Ed.* **2002,** 41, 1853-1859.
69. Vigolo, B.; Penicaud, A.; Coulon, C.; Sauder, C.; Pailler, R.; Journet, C.; Bernier, P.; Poulin, P., Macroscopic Fibers and Ribbons of Oriented Carbon Nanotubes. *Science* **2000,** 290, 1331-1334.
70. Islam, M. F.; Rojas, E.; Bergey, D. M.; Johnson, A. T.; Yodh, A. G., High Weight Fraction Surfactant Solubilization of Single-Wall Carbon Nanotubes in Water. *Nano Lett.* **2003,** 3, 269-273.
71. Penicaud, A.; Poulin, P.; Derre, A.; Anglaret, E.; Petit, P., Spontaneous Dissolution of a Single-Wall Carbon Nanotube Salt. *J. Am. Chem. Soc.* **2004,** 127, 8-9.
72. Chen, R. J.; Zhang, Y.; Wang, D.; Dai, H., Noncovalent Sidewall Functionalization of Single-Walled Carbon Nanotubes for Protein Immobilization. *J. Am. Chem. Soc.* **2001,** 123, 3838-3839.
73. Huang, W.; Fernando, S.; Allard, L. F.; Sun, Y.-P., Solubilization of Single-Walled Carbon Nanotubes with Diamine-Terminated Oligomeric Poly(ethylene Glycol) in Different Functionalization Reactions. *Nano Lett.* **2003,** 3, 565-568.
74. Pekker, S.; Salvetat, J. P.; Jakab, E.; Bonard, J. M.; Forro, L., Hydrogenation of Carbon Nanotubes and Graphite in Liquid Ammonia. *J. Phys. Chem. B* **2001,** 105, 7938-7943.
75. García-Gallastegui, A.; Obieta, I.; Bustero, I.; Imbuluzqueta, G.; Arbiol, J.; Miranda, J. I.; Aizpurua, J. M., Reductive Functionalization of Single-Walled Carbon Nanotubes with Lithium Metal Catalyzed by Electron Carrier Additives. *Chem. Mater.* **2008,** 20, 4433-4438.
76. Tagmatarchis, N.; Prato, M., Functionalization of carbon nanotubes via 1,3-dipolar cycloadditions. *J. Mater. Chem.* **2004,** 14, 437-439.
77. Meier, M. S.; Poplawska, M., The Addition of Nitrile Oxides to C60. *Tetrahedron* **1996,** 52, 5043-5052.
78. Kraatz, H.-B., Synthesis and electrochemistry of ferrocenemethylamine and its conjugated acid. Crystal structure of ferrocenemethylammonium chloride. *J. Organomet. Chem.* **1999,** 579, 222-226.
79. Maggini, M.; Scorrano, G.; Prato, M., Addition of azomethine ylides to C60: synthesis, characterization, and functionalization of fullerene pyrrolidines. *J. Am. Chem. Soc.* **1993,** 115, 9798-9799.
80. Georgakilas, V.; Kordatos, K.; Prato, M.; Guldi, D. M.; Holzinger, M.; Hirsch, A., Organic Functionalization of Carbon Nanotubes. *J. Am. Chem. Soc.* **2002,** 124, 760-761.
81. Georgakilas, V.; Guldi, D. M.; Signorini, R.; Bozio, R.; Prato, M., Organic Functionalization and Optical Properties of Carbon Onions. *J. Am. Chem. Soc.* **2003,** 125, 14268-14269.

82. Li, C.; Wang, D.; Liang, T.; Wang, X.; Wu, J.; Hu, X.; Liang, J., Oxidation of multiwalled carbon nanotubes by air: benefits for electric double layer capacitors. *Powder Technol.* **2004,** 142, 175-179.
83. Gergely, A. T., J.; Mészáros, E.; Pászti, Z.; Tárkányi, G.; Kármán, F.H.; Kálmán, E, Modification of Multi-Walled Carbon Nanotubes by Diels-Alder and Sandmeyer Reactions. *J. Nanosci. Nanotechnol.* **2007,** 7, 2795-2807.
84. Ericson, L. M.; Fan, H.; Peng, H.; Davis, V. A.; Zhou, W.; Sulpizio, J.; Wang, Y.; Booker, R.; Vavro, J.; Guthy, C.; Parra-Vasquez, A. N. G.; Kim, M. J.; Ramesh, S.; Saini, R. K.; Kittrell, C.; Lavin, G.; Schmidt, H.; Adams, W. W.; Billups, W. E.; Pasquali, M.; Hwang, W.-F.; Hauge, R. H.; Fischer, J. E.; Smalley, R. E., Macroscopic, Neat, Single-Walled Carbon Nanotube Fibers. *Science* **2004,** 305, 1447-1450.
85. Van Der Hoeven, P. C.; Lyklema, J., Electrostatic stabilization in non-aqueous media. *Adv. Colloid Interface Sci.* **1992,** 42, 205-277.
86. Xu, R.; Wu, C.; Xu, H., Particle size and zeta potential of carbon black in liquid media. *Carbon* **2007,** 45, 2806-2809.
87. Becker, H. I. Low voltage electrolytic capacitor. 23 July 1957, 1957.
88. Rightmire, R. A. Electrical energy storage apparatus. 29 Nov 1966, 1966.
89. M. Endo, T. T., Y. J. Kim, K. Koshiba, K. Ishii, High Power Electric Double Layer Capacitor (EDLC's); from Operating Principle to Pore Size Control in Advanced Activated Carbons. *Carbon Science* **2001,** 1, 117-128.
90. Pandolfo, A. G.; Hollenkamp, A. F., Carbon properties and their role in supercapacitors. *J. Power Sources* **2006,** 157, 11-27.
91. Wang, H.; Pilon, L., Accurate Simulations of Electric Double Layer Capacitance of Ultramicroelectrodes. *J. Phys. Chem. C* **2011,** 115, 16711-16719.
92. M Jayalakshmi, K. B., Simple Capacitors to Supercapacitors - An Overview. *Int. J. Electrochem. Sci.* **2008,** 3, 1196-1217.
93. Mastragostino, M.; Arbizzani, C.; Soavi, F., Polymer-based supercapacitors. *J. Power Sources* **2001,** 97, 812-815.
94. Lafuente, E.; Callejas, M. A.; Sainz, R.; Benito, A. M.; Maser, W. K.; Sanjuán, M. L.; Saurel, D.; de Teresa, J. M.; Martínez, M. T., The influence of single-walled carbon nanotube functionalization on the electronic properties of their polyaniline composites. *Carbon* **2008,** 46, 1909-1917.
95. Kovalenko, I.; Bucknall, D. G.; Yushin, G., Detonation Nanodiamond and Onion-Like-Carbon-Embedded Polyaniline for Supercapacitors. *Adv. Funct. Mater.* **2010,** 20, 3979-3986.
96. http://www2.chemistry.msu.edu/courses/cem419/cem372cyclicvoltammetry.
97. Frackowiak, E.; BÈguin, F., Carbon materials for the electrochemical storage of energy in capacitors. *Carbon* **2001,** 39, 937-950.
98. Simon, P.; Gogotsi, Y., Materials for electrochemical capacitors. *Nat. Mater.* **2008,** 7, 845-854.
99. Michael, M. S.; Prabaharan, S. R. S., High voltage electrochemical double layer capacitors using conductive carbons as additives. *J. Power Sources* **2004,** 136, 250-256.

100. Pajkossy, T. In *Fundamentals of Electrochemical Impedance Spectroscopy*, First Regional Symposium on Electrochemistry of South-East Europe, May 4-8, 2008, Croatia.
101. Pell, W. G.; Conway, B. E.; Marincic, N., Analysis of non-uniform charge/discharge and rate effects in porous carbon capacitors containing sub-optimal electrolyte concentrations. *J. Electroanal. Chem.* **2000,** 491, 9-21.
102. Qu, D.; Shi, H., Studies of activated carbons used in double-layer capacitors. *J. Power Sources* **1998,** 74, 99-107.
103. Stoller, M. D.; Ruoff, R. S., Best practice methods for determining an electrode material's performance for ultracapacitors. *Energy Environ. Sci.* **2010,** 3, 1294-1301.
104. McDonough, J. R.; Choi, J. W.; Yang, Y.; La Mantia, F.; Zhang, Y.; Cui, Y., Carbon nanofiber supercapacitors with large areal capacitances. *Appl. Phys. Lett.* **2009,** 95, 243109-3.
105. Xu, B.; Wu, F.; Chen, S.; Zhou, Z.; Cao, G.; Yang, Y., High-capacitance carbon electrode prepared by PVDC carbonization for aqueous EDLCs. *Electrochim. Acta* **2009,** 54, 2185-2189.
106. Liu, M.-C.; Kong, L.-B.; Zhang, P.; Luo, Y.-C.; Kang, L., Porous wood carbon monolith for high-performance supercapacitors. *Electrochim. Acta* **2012,** 60, 443-448.
107. Belyakov, A. I., Asymmetric electrochemical supercapacitors with aqueous electrolytes In *ELIT JSC, Kursk, Russian Federation*, Rome, Italy, Nov 6-7, 2008.
108. Ma, Y.; Luo, J.; Suib, S. L., Syntheses of Birnessites Using Alcohols as Reducing Reagents: Effects of Synthesis Parameters on the Formation of Birnessites. *Chem. Mater.* **1999,** 11, 1972-1979.
109. Gao, Q.; Giraldo, O.; Tong, W.; Suib, S. L., Preparation of Nanometer-Sized Manganese Oxides by Intercalation of Organic Ammonium Ions in Synthetic Birnessite OL-1. *Chem. Mater.* **2001,** 13, 778-786.
110. Liu, Z.-h.; Ooi, K.; Kanoh, H.; Tang, W.-p.; Tomida, T., Swelling and Delamination Behaviors of Birnessite-Type Manganese Oxide by Intercalation of Tetraalkylammonium Ions. *Langmuir* **2000,** 16, 4154-4164.
111. Plonska-Brzezinska, M. E.; Palkar, A.; Winkler, K.; Echegoyen, L., Electrochemical Properties of Small Carbon Nano-Onion Films. *Electrochemical and Solid-State Letters* **2010,** 13, K35.
112. Pech, D.; Brunet, M.; Durou, H.; Huang, P.; Mochalin, V.; Gogotsi, Y.; Taberna, P.-L.; Simon, P., Ultrahigh-power micrometre-sized supercapacitors based on onion-like carbon. *Nat Nano* **2010,** 5, 651-654.
113. Bock, C.; Paquet, C.; Couillard, M.; Botton, G. A.; MacDougall, B. R., Size-Selected Synthesis of PtRu Nano-Catalysts: Reaction and Size Control Mechanism. *J. Am. Chem. Soc.* **2004,** 126, 8028-8037.
114. Kim, Y.-T. I., Y.; Tadai, K.; Mitani, T.; Kim, U.-S.; Kim, H.-S.; Cho, B.-W., Drastic change of electric double layer capacitance by surface functionalization of carbon nanotubes. *Appl. Phys. Lett.* **2005,** 87, 234106-1 −234106−3.
115. Zheng, J. P.; Jow, T. R., High energy and high power density electrochemical capacitors. *J. Power Sources* **1996,** 62, 155-159.

116. Li, J.; Wang, X.; Huang, Q.; Dai, C.; Gamboa, S.; Sebastian, P., Preparation and characterization of RuO2.xH2O/carbon aerogel composites for supercapacitors. *J. Appl. Electrochem.* **2007,** 37, 1129-1135.
117. Emmenegger, C.; Mauron, P.; Sudan, P.; Wenger, P.; Hermann, V.; Gallay, R.; Z¸ttel, A., Investigation of electrochemical double-layer (ECDL) capacitors electrodes based on carbon nanotubes and activated carbon materials. *J. Power Sources* **2003,** 124, 321-329.
118. Wang, Y.; Shi, Z.; Huang, Y.; Ma, Y.; Wang, C.; Chen, M.; Chen, Y., Supercapacitor Devices Based on Graphene Materials. *J. Phys. Chem. C* **2009,** 113, 13103-13107.
119. Khomenko, V.; Raymundo-Piñero, E.; Béguin, F., Optimisation of an asymmetric manganese oxide/activated carbon capacitor working at 2V in aqueous medium. *J. Power Sources* **2006,** 153, 183-190.

VITA

Academic Background:

- Master of Science in Chemistry (2002), Dibrugarh University, India.
- Bachelor of Science in Chemistry (1999), Science College, Jorhat; Dibrugarh University, India.

Experiences:

- Executive Chemist (May 2007 – December 2007), Oil India Limited, Assam, India.
- Research Project Assistant (November 2005 – April 2007), Heterogeneous Catalysis Division, National Chemical Laboratory (NCL), Pune, India.
- Lecturer in Chemistry (non-tenure track) (August 2004 – October 2005), Dibrugarh University, Assam, India.

Honors:

- President of Materials Research Society Chapter-University of Kentucky 2010.
- Award winner in the KAS Graduate Research Competition in 2008.
- Qualified National Eligibility Test (NET, 2003) for academic, and research positions (RA) in the Universities and the National Research Centers in India.

Presentations:

- Kentucky Academy of Science Meeting (KAS) 2008 (Oral)
- Ohio Inorganic Meeting 2010 (Oral)
- Carbon Conference 2010 (Poster)

- 243rd ACS Meeting 2012 (Oral)
- Naff Symposium 2012 (Poster)

Professional Affiliations:

- Materials Research Society (MRS)
- Carbon Society
- The Electrochemical Society (ECS)
- American Chemical Society (ACS)
- Kentucky Academy of Science (KAS)

Publications:

- Electrochemical Study of Functionalized Carbon Nano-onions for High-Performance Supercapacitor Electrodes; ***Rituraj Borgohain****, Juchuan Li, John P. Selegue and Y.-T. Cheng; J. Phys. Chem. C* **2012***, 116,* 15068.
- Controlled Synthesis, Purification, and Electrochemical Study of Carbon nano-onions produced via underwater arc discharge; ***Rituraj Borgohain***, *Juchan Yang, John P. Selegue* and *Doo Young Kim*; Carbon **2013**, XXX, XXX (*In Press*).
- "Thin-layered MnO_2-carbon composites for Supercapacitor Electrodes" ***Rituraj Borgohain***, *John P. Selegue.* (Manuscript in preparation)
- Esterification of Carboxylic acids by Acid-activated Kaolinite Clay; *D. Konwar, P. K. Gogoi, P. Gogoi, G. Borah, R. Boruah, N. Hazarika,* ***R. Borgohain*** *Indian. J. Chem. Technol.* **2008***, 15,* 75.